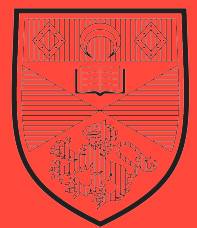


Cornell
University



University of
St Andrews

The Electronic Structure of the Nematic Materials $\text{Sr}_3\text{Ru}_2\text{O}_7$ and $\text{Ca}(\text{Co}_x\text{Fe}_{1-x})_2\text{As}_2$

by Milan P. Allan
from Innertkirchen, BE and Freiburg, FR,
Switzerland

a dissertation presented to the University of St. Andrews
in application for the degree of Doctor of Philosophy

March 2010

Declarations required by the University of St. Andrews

I, Milan P. Allan, hereby certify that this thesis, which is approximately 28 thousand words in length, has been written by me,¹ that it is the record of work carried out by me,¹ and that it has not been submitted in any previous application for a higher degree.

date April 6, 2010 signature of candidate M. Allan

I was admitted as a research student in November 2006 and as a candidate for the degree of Doctor of Philosophy in November 2006; the higher study for which this is a record was carried out in the University of St. Andrews² between November 2006 and April 2010.

date April 6, 2010 signature of candidate M. Allan

I hereby certify that the candidate has fulfilled the conditions of the Resolution and Regulations appropriate for the degree of Doctor of Philosophy in the University of St. Andrews and that the candidate is qualified to submit this thesis in application for that degree.

date 8.9.2010 signature of supervisor F. D. M.

In submitting this thesis to the University of St. Andrews we understand that we are giving permission for it to be made available for use in accordance with the regulations of the University Library for the time being in force, subject to any copyright vested in the work not being affected thereby. We also understand that the title and abstract will be published, and that a copy of the work may be made and supplied to any *bona fide* library or research worker, that my thesis will be electronically accessible for personal or research use, and that the library has the right to migrate my thesis into new electronic forms as required to insure continued access to the thesis. We have obtained any third-party copyright permissions that may be required in order to allow such access and migration.

The following is an agreed request by candidate and supervisor regarding the electronic publication of this thesis: Embargo on both printed copy and electronic copy for the same fixed period of six months on the following ground: publication would preclude future publication.

date April 6, 2010 signature of candidate M. Allan

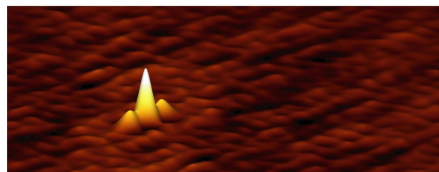
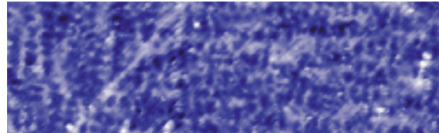
date 8.9.2010 signature of supervisor F. D. M.

¹Research in physics is almost always teamwork. Many people were involved in building and improving instruments, making discoveries and writing papers. I tried to mention all of them in the acknowledgements.

²Parts of the work were carried out at Cornell University.

Abstract

We investigated the electronic structure of the two nematic materials $\text{Sr}_3\text{Ru}_2\text{O}_7$ and $\text{Ca}(\text{Fe}_{0.97}\text{Co}_{0.03}\text{As})_2$ using spectroscopic – imaging scanning tunneling microscopy (SI-STM) and angle resolved photoemission spectroscopy (ARPES). – – – $\text{Sr}_3\text{Ru}_2\text{O}_7$ is an itinerant metamagnet that shows a putative quantum critical endpoint at 8 Tesla, submersed by the formation of a nematic electronic phase. Using ARPES, we identified at least 5 Fermi pockets in agreement with quantum oscillation measurements. Surprisingly, we found Fermi velocities up to an order of magnitude lower than in single layer Sr_2RuO_4 and up to 35 times lower than predicted by *ab initio* calculations. Many bands are confined in an energy range of only ~ 10 meV below the Fermi level. This, as well as distinct peak-dip-hump shapes of the spectra with a characteristic energy of around ~ 5 meV indicate strong correlations and a possible nontrivial mechanism that is absent in single layer Sr_2RuO_4 and connected to the nematicity. The quasiparticle interference of one of the bands was detected by SI-STM, which was also used to measure subatomic features with the symmetries of the relevant Ru *d* orbitals. – – – In the second material, the iron-based high-temperature superconductor $\text{Ca}(\text{Fe}_{1-x}\text{Co}_x\text{As})_2$, we discovered electronic nematic nano-pattern in its under-doped ‘parent’ state. We spectroscopically imaged this state in real space over large areas and across domain boundaries that change the directionality of the nano-pattern by 90° . We propose that oriented, dimer-shaped electronic nematogens are responsible for this pattern, in striking contrast to what has been expected and observed in electronic nematic materials. The dimers consist of two Gaussian conductance peaks separated by about $8 a_{\text{FeFe}}$. Unidirectionality also shows in the quasiparticle interference pattern of the delocalized electrons. The dispersion is in agreement with scattering from the α_2 band discovered by ARPES but has distinct C_2 symmetry, not inconsistent with a C_4 -symmetric band scattered by the proposed dimers.



© Milan P. Allan

Advised by Felix Baumberger and J.C. Séamus Davis
Examined by Mark S. Golden and Chris Hooley

to my family

Acknowledgements

After much procrastination, this thesis was cobbled together in two short months, and it shows. The work behind it, however, stretched over about 3.5 years. And whenever something useful came out of this work, it was probably thanks to the help of countless persons, some of whom (the whole list would be too long) I would like to acknowledge in this section.

First, I want to thank my advisors, J.C. Séamus Davis and Felix Baumberger. Séamus' energy, his unique way of thinking about physics, his creativity, 'his' STM, and his ability to ask the right questions and to catch interesting results at a point where they are just slight transients in the noise continue to impress me. Felix involved me into science right after I arrived; I enjoyed the beamtimes in Palo Alto and also the dinners at *Il Fornai*o, the few visits in St. Andrews, and the long Skype-sessions. His calm but determined, honest way to do science certainly influenced me. I am very grateful to Séamus and Felix for interesting discussions, support, encouragement, and advice.

Mark S. Golden and Chris Hooley were my thesis examiners. I appreciate all their insightful comments and corrections, and their ideas for further experiments.

Tien-Ming Chuang was (and is) my long-time partner on STM1, we did all the pnictide research, as well as much repair and maintenance work together. We spent countless days and nights in the lab, had many hectic phone calls when the temperature curve on our monitors at home did not behave as expected, and had hour-long, heated discussions on whether to warm up 'our' STM or not.

Miao 'Alfred' Wang had an incredible dedication to STM1, and he spend time teaching me the mechanisms, tricks, and traditions of this historic machine. I appreciate what he taught me.

Many members of the Davis group helped me with little problems, gave inspiring advice, contributed important ideas, or renewed my motivation for physics by telling me about their discoveries in the hallway. I want to thank Jinho Lee (who lead the QPI project on $\text{Sr}_3\text{Ru}_2\text{O}_7$), Yang Xie (the newest member of team STM1, welcome), Mohammad H. Hamidian (for being in the same boat), Vikram Gadagkar (for the life-coaching), Andy 'The Library' Schmidt, Kazuhiro 'Kazupedia' Fujita, Sourin Mukhopadhyay, Chung Koo Kim, Inês Firmo, Morgann Berg, Peter Wahl, Curry Taylor, Minoru Yamashita, Yuhki Kohsaka, Focko Meier, Benjamin Hunt & Ethan Pratt (for explaining how a fridge works), and Jhinhwan 'crazy electronics' Lee (for help with the instrument).

Eun-Ah Kim and Michael Lawler kept my motivation up with fun and en-

lightening discussions, contributed many ideas, and were incredibly tolerant of my occasional ignorance of fundamental physics.

I am also thankful to Kaden Hazaard, Mark Hannes Fischer, Srivatsan Chakram Sundar, and Sumiran Pujari for explaining quantum mechanics and the like to me, and to Duane Loh, for contributing great ideas to find the nematogens.

My gratitude also goes to the condensed matter teams in St. Andrews and at Stanford/SSRL, for all the hospitality. Special thanks to Anna Tamai, with whom I spend much time in the noise of the cryopumps in California, and Andy P. Mackenzie, who introduced me to the ruthenates, contributed ideas in many nice discussions, and was always incredibly supportive. Further, Worawat ‘Non’ Meevasana, Emil Rozbicki (who did most of the LDA+SO calculations), Mary Rodger, Ross Dunkel, Jean-François Mercure, Felix Schmitt, and Z.X. Shen, were of much help in many regards. Andreas Rost contributed much insight in discussions and was, during his visit, very helpful in many regards.

Progress in strongly correlated electron systems is often driven by the people who grow crystals. I feel fortunate that we could use high-quality samples for our work. The CaFe_2As_2 were grown by Ni Ni and Sergey L. Bud’ko from the Paul Canfield group in Ames Laboratory. The $\text{Sr}_3\text{Ru}_2\text{O}_7$ crystals were grown by Jason Farrell, Alex Gibbs and Robin Perry, from the Andy P. Mackenzie group in St. Andrews. Thank you!

I appreciate that Felix, Mark, Ming, Séamus and Andreas gave me helpful comments on the manuscript, and that Ming, Andreas, and Yang covered my part of work in the lab while I was trying to write a thesis.

I want to thank the friendly staff in the basement of Clark, e.g. Eric Smith, Nick Brown, Linda Hatch, Stan Carpenter, Bob Snedeker, Bob Tillotson, Nathan Ellis, Chris Cowulich, Stan McFall, Jeff Koski, Dan Sheerer, and Rodney Bowman. Research here would not be possible without them.

The foundations on which this thesis was built were laid long ago: I want to thank Eric Hudson and Christian Lupien for writing code that everyone still uses, and Shuheng Pan for designing the most awesome STM head ever.

Thanks to Jürg Osterwalder, Matthias Hengsberger, Thomas Gerber and Simon Berner for teaching me experimental physics.

I could never have stayed sane and happy without all the wonderful people whose paths I was fortunate enough to cross in Ithaca, gorges Ithaca. We are all in the same bubble. I’m incredibly thankful to amazing Hạnh Phương Nguyễn, Kavita Ashana Singh, Caroline Philothée Ferraris-Besso, Amaya Atucha, Guillaume Ratel, Alex Ratel, Lorenzo Fabbri, Abi Fisher, Marcela Romero (for introducing me to Ithaca), Ada Maria Kuskowski, famous Valentine Pétry, Juan Sierra, Mike Castro Reyes, John Dương Phan,

Sophie Rittner (for coming to lunch), Juan Lube, Chia-chen Chou, Yuki Inoue, Tsitsi Jaji, Claudine Ang, Sara Grundel, Douglas Kawano, Sezi Seskir, Esther Blodau-Konick (for making my first apartment a nice home), Tina Waltraud Rebelein, Michelle Smith, Trisha Kanjirath, Kari Perez, Mirabelle Yang, Joseph Stevens, Arend van der Zande, Jörn Kupferschmidt, Kelly Chan, Shushan Xu, and *many, many* more that I forgot to list here !

Thanks also to all the ‘Swiss’. Whenever I visited Switzerland, I enjoyed discussions and company of my family, Martin, Mirek, Miša and Annelies, and my friends, Kai Eberhardt, Dani Jossen (who shared nine years of my education with me), Stefano Balestra, Mark Drenhaus, Carmen Chan, Sophie Wenger, Ann-Karin Sanchez, and especially Silva Celio, who shaped quite a part of me.

Thank you guys, it was nice! ~

List of acronyms

SI-STM	spectroscopic imaging – scanning tunneling microscopy
ARPES	angle-resolved photoemission spectroscopy
1d / 2d	one-dimensional / two-dimensional
DC / AC	direct current / alternating current
FOV	field-of-view
LDA	local-density approximation
LDA+SO	local-density approximation + spin-orbit coupling
dHvA	de Haas – van Alphen
DOS	density-of-states
LDOS	local density-of-states
JDOS	joint density-of-states
SNP	static nematic pattern

Contents

Abstract	i
Acknowledgements	iv
List of acronyms	viii
Contents	ix
1 Introduction	1
1.1 Motivation	1
1.2 Strongly correlated electronic states in solids	2
1.3 Directional order	3
2 Experimental techniques	7
2.1 Angle resolved photoemission spectroscopy	7
2.1.1 Physical background	7
2.1.2 Experimental setup	10
2.2 Spectroscopic imaging - scanning tunneling microscopy	12
2.2.1 Complete mapping of the local density-of-states	12
2.2.2 Quasiparticle interference	15
2.2.3 Experimental considerations	15
3 The bilayer ruthenate $\text{Sr}_3\text{Ru}_2\text{O}_7$	18
3.1 The strontium ruthenate family	18
3.2 Crystalline structure and synthesis	19
3.3 The phase diagram: magnetism, criticality, and nematicity	21
3.4 Theoretical models	23
4 The electronic structure of $\text{Sr}_3\text{Ru}_2\text{O}_7$ seen by ARPES	25
4.1 Fermi surface mapping	26
4.2 Strong \mathbf{k} - and orbital dependent quasiparticle renormalization	30
4.2.1 Renormalization factors in $\text{Sr}_3\text{Ru}_2\text{O}_7$	31
4.2.2 Direction dependent renormalization	34
4.2.3 Low energy kink in the α_1 -band	34
4.2.4 Orbital character and renormalization	36

4.3	Van Hove singularities and density of states	38
4.4	Concluding remarks	41
5	Real-space orbital imaging of $(\text{Sr}_{0.99}\text{Ti}_{0.01})_3\text{Ru}_2\text{O}_7$	43
6	Quasiparticle interference of the α_2-band	48
6.1	Fourier transform SI-STM data	48
6.2	Quasiparticle interference from the model α_2 -band	49
6.3	Agreement between the model α_2 band and ARPES	54
7	The ferropnictides: a second family of high-temperature superconductors	56
7.1	The different families	57
7.2	Ground state electronic structure	59
7.3	The phase diagram	60
7.4	Similarities with the cuprates	61
7.5	STM experiments on the ferropnictides	62
8	SI-STM of the nematic electronic state in $\text{Ca}(\text{Fe}_{0.97}\text{Co}_{0.03}\text{As})_2$	65
8.1	Static nematic pattern in $\text{Ca}(\text{Fe}_{0.97}\text{Co}_{0.03}\text{As})_2$	68
	8.1.1 Domain boundaries	68
	8.1.2 Changes in the nematic pattern with varying energy . .	71
8.2	Dimer-shaped nematogens	72
	8.2.1 Simulations	74
	8.2.2 Fourier transform of dimer-shaped nematogens	75
	8.2.3 Impurity imaging	78
8.3	C_2 -quasiparticle interference	83
8.4	Concluding remarks	89
	Bibliography	91

Chapter 1

Introduction

This thesis discusses the effect of strong electronic correlations and the emergence of electronic nematicity, studied in $\text{Ca}(\text{Fe}_{0.97}\text{Co}_{0.03}\text{As})_2$ and $\text{Sr}_3\text{Ru}_2\text{O}_7$. The following sections aim to motivate our research, to give some background information, and to survey some of the results.

Note that it is assumed that the reader of this thesis has a knowledge of condensed matter physics. The basic concepts such as Fermi liquid theory are assumed. The basic techniques are only briefly reviewed in chapter 2, and the materials studied are introduced in chapters 3 and 7, respectively.

1.1 Motivation

Even though the fundamental rule that governs the motion of electrons in solids, the Schrödinger equation, is known, many of us are again and again surprised by the fascinating, unexpected, and complex behavior that can emerge from electrons obeying this simple rule. Perhaps this is due to two reasons: First, the emergence of complexity from simple rules is often strongly dependent on weak tuning of the constituents and slight differences in the governing rules. The path from the initial parts to the emergent phenomenon is, if present, often not accessible to our intuition. Theories adapted to the level of complexity are needed. Specifically, even though we understand the equations that govern the motion of one electron in a solid, we do not understand the emerging solutions of the associated many-body problem. Second, even if it is possible to reduce complex behavior to simple rules, the opposite is usually impossible. It is not likely that any physicist would have derived superconductivity, or biology, from quantum mechanics before seeing the experimental evidence thereof.

Emerging phenomena are abundant in nature, and include different sys-

tems such as ant-hives, neural networks, and in our case, electrons in a solid.¹ In the latter, electron can, e.g. form spatially ordered or superconducting phases. Understanding these complex states, their microscopic origin, and their interplay and competition has been a major challenge to solid state physics in the past decades.

This thesis deals with materials ideal to study the phenomena mentioned above. $\text{Sr}_3\text{Ru}_2\text{O}_7$, discussed in chapters 3 to 6, shows a directional electronic ordering in a magnetic field of 8 Tesla. We investigated its ground-state electronic structure that has many indications of strong electronic correlations. CaFe_2As_2 , discussed in in chapters 7 and 8 is found to form a very special short-range correlated nematic state. Lastly, we want to mention here that even though our primary motivation is to understand the fascinating underlying concepts, the examples of emerging electronic states having a profound impact on technology are plentiful — superconductivity or giant-magnetoresistance are examples.

1.2 Strongly correlated electronic states in solids

Electrons are charged, and thus naturally interact with each other. However, in many solids, such as gold, copper, and silver, the interaction can be elegantly included by describing, instead of electrons, *quasiparticles*, which behave like free electrons with renormalized characteristic properties such as mass, velocity, etc. scaled by a factor. This concept is part of the Landau theory of electronic liquids [5]. The strength of the renormalization factors is a rough measure on how strong the electron-electron interactions are.

On the (111) surface of copper, the surface state has a Fermi vector of $v_F = 0.22 \text{ \AA}^{-1}$ and Fermi velocity v_F of almost 3000 meV\AA . These values are close to those of a free electron Fermi gas: The electrons are only lightly correlated [6, 7, 8]. Fig. 4.4 in chapter 4 will illustrate that for electrons in the δ band in $\text{Sr}_3\text{Ru}_2\text{O}_7$, the Fermi wave vector is only about half, but the value of the Fermi velocity is much lower, $v_F \approx 50 \text{ meV\AA}$. This is almost a factor of 60: $\text{Sr}_3\text{Ru}_2\text{O}_7$ is, at low temperature and zero field, a *strongly* correlated electron system. Another indication for strong correlations in $\text{Sr}_3\text{Ru}_2\text{O}_7$ is the high Wilson ratio. In a weakly correlated system, the Wilson ratio can be estimated by the susceptibility of a single electron, when it is higher, quasiparticles interact to enhance the spin response.

The nematic electronic states imaged in $\text{Ca}(\text{Fe}_{0.97}\text{Co}_{0.03}\text{As})_2$ described in chapters 7 and 8 are perhaps even more correlated. SI-STM images show

¹Many people from different fields have discussed the subject of emergence, we cite Refs. [1, 2, 3, 4] as examples.

highly inhomogeneous states, in disagreement with simple Bloch states. We will explain this inhomogeneity with a disordered set of oriented nematogens, forming an electronic nematic, with parallels to the ‘liquid crystals’ introduced in the next section.

1.3 Directional order

In this section we will introduce some definitions for different forms of directional order that we will later use to describe nematic electronic states. We start from the well-established field of *liquid crystals*, which are compounds made of anisotropic molecules with various degrees of directional order. We will then discuss the comparison with unidirectional electronic systems and port some of the concepts and definitions.

A liquid/solid of anisotropic molecules can have fascinating properties. To use the historic language, there can be several different ‘melting points’ where solids can change to cloudy, ‘half crystalline’ ordered liquids which then turn into clear liquids. It is now known that this is a consequence of the anisotropic molecules having directional order without translational order – the material becomes liquid, yet it maintains more order than a conventional liquid. A liquid in which the molecules have no translational symmetry but directional order is called ‘nematic’. If the order is maintained in one direction only, it is called ‘smectic’. The mentioned cloudiness of a liquid crystal derives from the ability of the ordered molecules to change the polarization of light depending on their order — a phenomenon that can have technological use, as will be discussed later. The anisotropic molecules, or other constituents whose microscopic orientation induces directional order, are commonly called ‘nematogens’. Fig. 1.1 shows schematically images of crystalline, smectic, and nematic order. The left column shows schematic images of nematogens, while the images in the right column show the relevant orders purely schematic using lines.

The reason for the technological importance of liquid crystals lies in the fact that it is possible to steer liquid crystal phases by electrical fields *and* that liquid crystals change the polarization of light depending on their order, allowing the construction of displays. Arrays of transparent capacitors with liquid crystals between the plates can be used to direct individual pixels to well-defined liquid crystal phases. Polarized light is then shone through the array, and each pixel rotates the polarized light according to its particular liquid crystals phase. A linear polarization filter, rotated 90° relative to the incident polarization converts the rotation angle of the polarization in a light intensity, such that light going through liquid crystal regions that do not

affect its polarization does not pass while light with its polarization changed can pass. Consequently, it becomes possible to steer the grayscale of the array by the voltages across the capacitances. This and similar devices are called ‘liquid crystal displays’, or short LCDs, and are projected to make a 100 billion market in 2010 [9].

On the other hand, electrons in a solid such as the high-temperature superconductors are very different from anisotropic molecules in classical liquid crystals. Nevertheless, they can also form liquid-like states (e.g. Fermi liquids) in proximity to solid-like states (e.g. Mott-insulators). In between, different unidirectional arrangements have been proposed [10] and measured [11, 12]. The comparison to liquid crystals comes naturally. Kivelson *et al.* [10] termed this unidirectional states between insulator and Fermi liquid (or superconductor) ‘electronic liquid crystals’, and proposed that nematic, smectic, and isotropic electronic phases can exist.

However, in the electronic analogue to a liquid crystal, the definitions for ‘smectic’ and ‘nematic’ can not be used in exactly the same way. Two challenges are present: *(i)*, there is not necessarily any obvious analogue to the nematogens in liquid crystals where they are anisotropic molecules, and *(ii)*, the directional symmetry is already broken by the atomic lattice.

Problem *(i)* can be avoided by making the definitions of ‘nematic’ and ‘smectic’ without explicitly referring to the nematogens, emphasizing the order. In fact, no electronic nematogens have yet been imagined by any probe – chapter 8 will report on a possible first exception.

To deal with *(ii)*, the definition of electronic directional order is phrased relative to the underlying lattice, e.g. we could say a system is smectic or nematic if the electronic structure has lower symmetry than the underlying lattice. Physically, however, this is almost impossible, electron-lattice coupling will not allow a unidirectional electronic structure without at least a tiny subsequent distortion of the lattice. For that reason, we will use a definition somewhat softer, and call a system an ‘electronic smectic/nematic’ if the electronic structure shows an unidirectionality far greater than could be expected from some possible minuscule lattice distortion.

More precisely, we will use the following definitions:

- A system is in an *electronic nematic* state if the electronic structure shows unidirectionality far greater than what can be expected from the lattice symmetry, and if there is no translational symmetry in any direction.
- A system is in an *electronic smectic* state if the electronic structure shows unidirectionality far greater than what can be expected from the

lattice symmetry, and if there is translational symmetry in one direction only, as indicated by a Bragg peak.

Finally, we will call an electronic structure that holds to either definition an *electronic liquid crystal*.

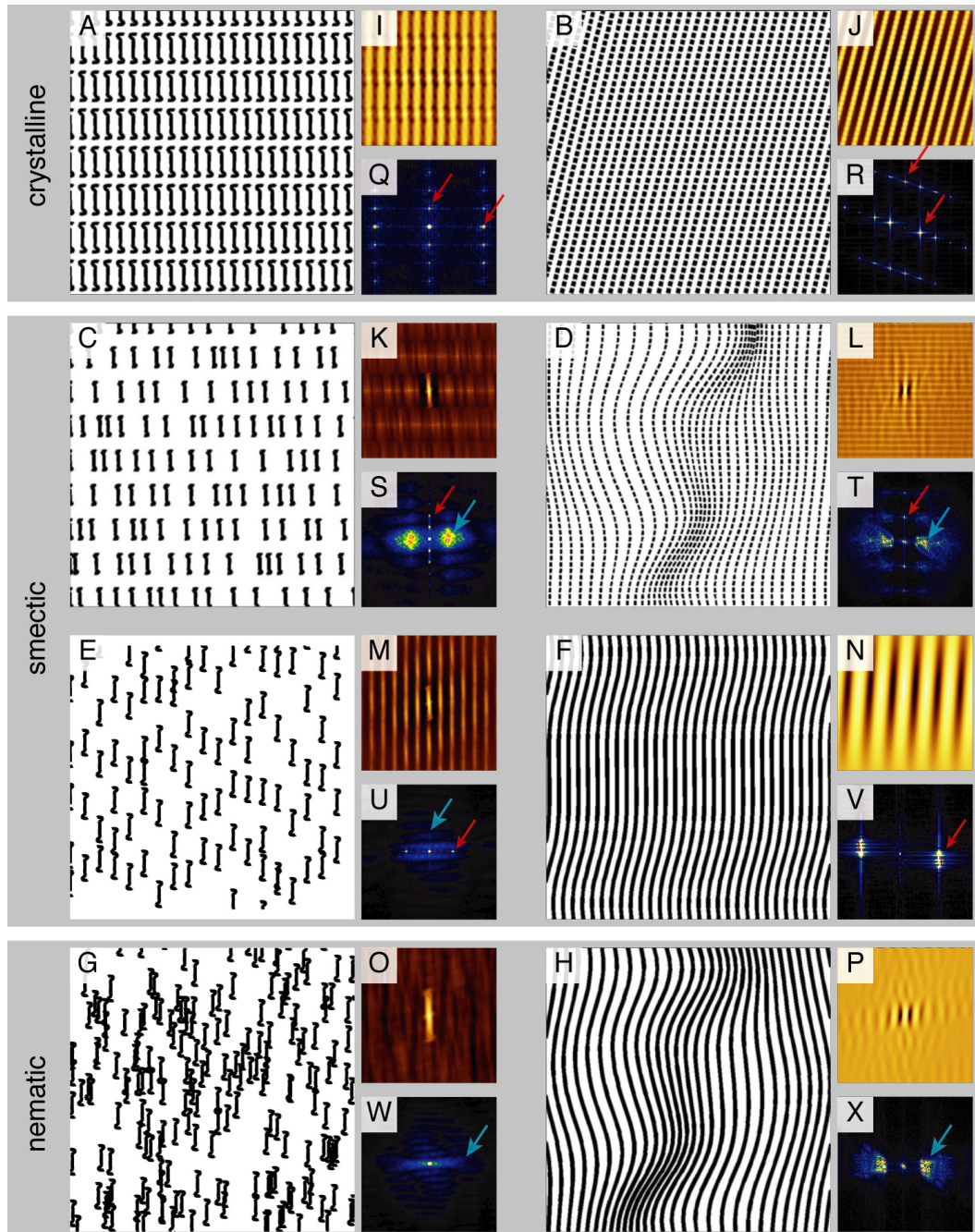


Figure 1.1: Schematic illustration of directional order. (A,B), 'Crystal' of rod-shaped nematogens or dashed lines. (C,D,E,F), Smectic order: There exists directional order but translational symmetry in one direction only. (G,H), Nematic order: There exist only directional order, no long range spatial periodicity. (I-P), The respective auto-correlations reflect the order. In case of the rod-shaped nematogens in nematic order, the autocorrelation closely reflects the shape of the nematogens. (Q-X), The Fourier transforms show Bragg peaks in case of spatial periodicity (marked by red arrows), or broad peaks for spatial short-range correlation (blue arrow). (I-X) are not to scale. Note that all the pictures are schematic illustrations without physical meaning.

Chapter 2

Experimental techniques

The subject of this thesis is the electronic structure of $\text{Sr}_3\text{Ru}_2\text{O}_7$ and $\text{Ca}(\text{Fe}_{1-x}\text{Co}_x\text{As})_2$ investigated by two techniques, angle resolved photoemission spectroscopy (ARPES) and spectroscopic imaging - scanning tunneling spectroscopy (SI-STM). Here, it is not our aim to give a full review of either, but just to briefly survey the two techniques and to give references to more in depth treatment.

2.1 Angle resolved photoemission spectroscopy

More comprehensive descriptions of angle resolved photoemission spectroscopy (ARPES) are available elsewhere, e.g. Hüfner [13] or Damascelli *et al.* [14], which reviews ARPES on cuprates.

2.1.1 Physical background

When one irradiates a solid with light, an electron can absorb a photon and be emitted from the surface if the energy from the photon ($h\nu$) is greater than the potential barrier at the surface (ϕ , termed ‘workfunction’). This is the so-called ‘photoelectric effect’. The kinetic energy of the emitted photoelectron is

$$E_{\text{kin}} = h\nu - \phi - E_{\text{Binding}},$$

with E_{Binding} the binding energy of the electron in the solid. Translation invariance on the surface implies crystal momentum conservation, and this connects the momentum of the photoelectron $\hbar|\mathbf{k}_{\parallel}|$ emitted at polar angle ϑ with its parallel wavevector in the solid:

$$\hbar|\mathbf{k}_{\parallel}| = \sqrt{2E_{\text{kin}}} \cdot \sin \vartheta.$$

Note that throughout this chapter we assume that the materials studied are sufficiently two-dimensional to assume negligible k_z dispersion. The two equations above relate the measurable quantities E_{kin} and \mathbf{p}_{\parallel} of the photoelectron with important physical quantities it had in the solid, E_{binding} and \mathbf{k}_{\parallel} — this is the basic principle of ARPES.

Let us now take a slightly more detailed look at what happens in real experiments in order to calculate the photocurrent $I(\mathbf{k}, \omega)$ measured by the analyzer. We will use the so called three-step model, approximating the photoeffect as three independent processes (Fig. 2.1A) : *(i)*, the photon hits the sample and excites an electron, that evolves with probability $w_{f,i}$ from the initial state into the final one. In the so-called 'sudden approximation', the solid instantly adapts to the missing electron, i.e. there is no post-excitation interaction between the photoelectron and the sample. Second, *(ii)*, the photoelectron travels inside the solid to the surface. Since the mean free path of electrons with typical energies in our ARPES experiments (14 to 50 eV) is around 5 Å, only electrons close to the surface have to be considered. Lastly, *(iii)*, the photoelectron overcomes the potential barrier ϕ at the surface and is emitted. We can neglect this step since it only affects k_z .

The photocurrent $I(\mathbf{k}, \omega)$ is proportional to the sum of the transition probabilities $\Sigma_{\{f,i\}} w_{f,i}$. Following Refs. [15, 13], we calculate them using Fermi's golden rule,

$$w_{f,i} \propto |\langle \Psi_f^N | H_{\text{int}} | \Psi_i^N \rangle|^2 \delta(E_f^N - E_i^N - h\nu). \quad (2.1)$$

The delta function guarantees energy conservation for photon energy and initial/final state energy, $E_i^N = E_i^{N-1} - E_{\text{binding}}^{\mathbf{k}}$ and $E_f^N = E_f^{N-1} + E_{\text{kin}}^{\mathbf{k}}$.

In the sudden approximation, the final state can be written as a product of photoelectron state and the excited state left behind,

$$\Psi_f^N = \mathcal{A} \phi_f^{\mathbf{k}} \Psi_f^{N-1},$$

where \mathcal{A} is the total antisymmetric operator, $\phi_f^{\mathbf{k}}$ it the state of the photoelectron, and Ψ_f^{N-1} is the final $N - 1$ electron state that we assume to be one of the excited states Ψ_{ex}^{N-1} of the system. Then,

$$w_{f,i} \propto |\langle \phi_f^{\mathbf{k}} | H_{\text{int}} | \phi_i^{\mathbf{k}} \rangle|^2 |\langle \Psi_{\text{ex}}^{N-1} | a_{\mathbf{k}} | \Psi_i^N \rangle|^2 \delta(E_f^N - E_i^N - h\nu).$$

Here, we assumed that the initial state can also be written as a product of an one-electron state and the $N - 1$ initial state, $\Psi_i^N = \mathcal{A} \phi_i^{\mathbf{k}} \Psi_i^{N-1}$. H_{int} is the interaction Hamiltonian for photon and electron. $a_{\mathbf{k}}$ is the annihilation operator, $a_{\mathbf{k}} \Psi_i^N = \Psi_i^{N-1}$.

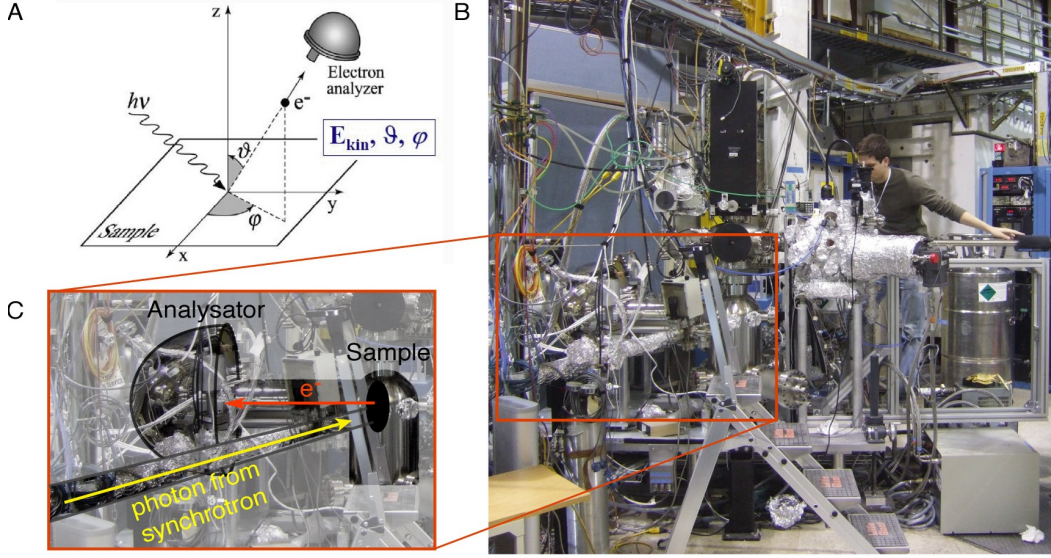


Figure 2.1: Typical ARPES experiment. (A), Schematic illustration of the three step process: (i), a photon hits the sample, (ii) excites an electron, and (iii), the photoelectron leaves the surface and its kinetic energy and polar and azimuthal angle are measured by the analyzer. (B), Representative graduate student at the Stanford Synchrotron Radiation Laboratory, beamline 5.4. (C), Incoming light, sample, and analyzer at the beamline.

The total photocurrent is then the sum over all excited states Ψ_{ex}^{N-1} in eq. 2.1,

$$I_{\text{photo}}(\mathbf{k}, \omega) \propto \sum_{\{f,i\}} |M_{f,i}(\mathbf{k})|^2 \sum_{\text{ex}} |\langle \Psi_{\text{ex}}^{N-1} | a_{\mathbf{k}} | \Psi_i^N \rangle|^2 \delta(E_f^N - E_i^N - h\nu),$$

where $|M_{f,i}(\mathbf{k})|^2 = |\langle \phi_f^{\mathbf{k}} | H_{\text{int}} | \phi_i^{\mathbf{k}} \rangle|^2$ is the one-electron matrix element, and the term $\sum_{\text{ex}} |\langle \Psi_{\text{ex}}^{N-1} | a_{\mathbf{k}} | \Psi_i^N \rangle|^2$ is identified with the spectral function $A(\mathbf{k}, \omega)$. In summary, we have

$$I_{\text{photo}}(\mathbf{k}, \omega) = f_{FD}(\omega) |M_{f,i}(\mathbf{k})|^2 A(\mathbf{k}, \omega),$$

with $f_{FD}(\omega)$ the Fermi-Dirac function. $A(\mathbf{k}, \omega)$, the one-particle spectral function, is the quantity of interest. Intuitively, it gives the density of one-particle excitations in (\mathbf{k}, ω) -space. It can be separated in bare bandstructure $\varepsilon(\mathbf{k})$ and correlation/coupling effects added through a complex *self-energy*

$$\Sigma = \Sigma_{\text{re}} + i\Sigma_{\text{im}},$$

$$A(\mathbf{k}, \omega) = -\frac{1}{\pi} \frac{\Sigma_{\text{im}}(\mathbf{k}, \omega)}{(\omega - \varepsilon(\mathbf{k}) - \Sigma_{\text{re}}(\mathbf{k}, \omega))^2 + (\Sigma_{\text{im}}(\mathbf{k}, \omega))^2}. \quad (2.2)$$

The real part of the self energy gives the strength and shape renormalization, and the imaginary part gives the broadening of the quasiparticle peak.

Through different models for the self energy, or through predictions for the bare bandstructure by *ab initio* calculations, this often allows us to back-calculate the bare-bandstructure $\varepsilon(\mathbf{k})$ and separate it from effects such as phonon coupling and correlations [16, 17, 18, 19].

2.1.2 Experimental setup

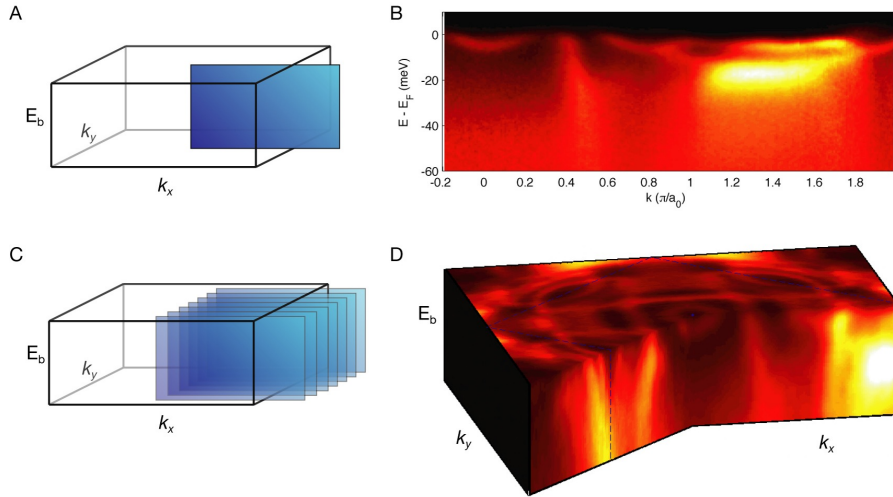


Figure 2.2: Typical ARPES measurements. (A), Schematic view of the $A(\mathbf{k}, \omega)$ cube. The blue plane marks the \mathbf{k} , E location of a high symmetry cut that can be efficiently measured by modern analyzers. (B), False color plot of the photocurrent intensity in such a measurement in $\text{Sr}_3\text{Ru}_2\text{O}_7$. (C), To map the whole $A(\mathbf{k}, \omega)$ cube, one takes many parallel cuts and interpolates the values to a new grid spanning the whole cube. (D) is an example of the resulting data set, the top surface is a mapping of the Fermi surface. For details about this particular measurement, see chapter 4.

Fig. 2.1 is an illustration of a typical ARPES experimental setup. A light source, usually a He-discharge lamp or a synchrotron radiation source, irradiates a sample, prepared *in situ* in ultra-high-vacuum. Electrons are emitted, travel through a hemispherical analyzer and are detected on a CCD

screen. The analyzer filters the kinetic energy of the photoelectron; the polar and azimuthal angle are scanned by changing the sample orientation.

Due to the electron-optical properties of most state-of-the-art analyzers, most experiments measure *slices* of $A(\mathbf{k}, \omega)$ in the \mathbf{k}, ω space. Typically, we either measure high resolution, high S/N slices along high symmetry directions, or many slices covering the whole Brillouin zone, from which we then extract the Fermi surface. The two measurements are illustrated in Fig. 2.2.

Most ARPES experiments described in this thesis were performed at the instrument built by the group of Z.X. Shen at Stanford University that uses a monochromatized He-discharge lamp with 21.2 eV photons, and a Scienta SES2002 analyzer. We used an energy and momentum resolution of 4.2 meV and 0.3° , respectively. Some additional experiments were performed at the beamline 5.4 at Stanford Synchrotron Radiation Laboratory (SSRL), part of SLAC National laboratory, Menlo Park, CA. There, we used a Scienta R4000 analyzer with resolution 8 meV, 0.3° . Unless stated otherwise, all data from the SSRL beamline was taken using 21.2 eV photons. Temperatures on the sample were always between 5 and 9 K, the cleaves were prepared *in situ* and measured at a pressure below $5 \cdot 10^{-11}$ mbar.

2.2 Spectroscopic imaging - scanning tunneling microscopy

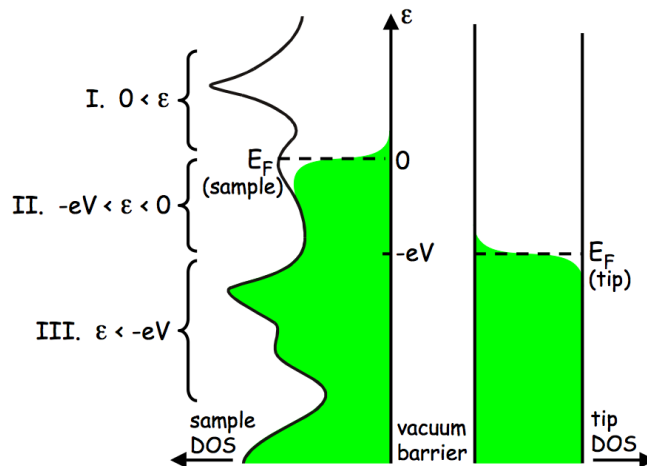


Figure 2.3: Schematic drawing of the density-of-states of sample (with bias V_B) and tip. *Figure reproduced from Ref. [20].*

Macroscopic tunneling experiments can measure the density-of-states of a solid, and are associated with milestones in understanding condensed matter physics such as the observation of the excitation gap in superconductors [21]. On the other hand, scanning tunneling microscopy (STM) is a well explored technique to image surfaces on the Ångstrom scale [22]. It seems natural to combine the two techniques, i.e. to use a STM and perform a tunneling experiment at every location on the surface, with the goal to measure the *local* density-of-states, $LDOS(\mathbf{r}, E)$. This technique goes under different names, we will call it ‘spectroscopic imaging - scanning tunneling microscopy’ (SI-STM). It was pioneered on metal surfaces [23, 24] and is nowadays also successfully used for high-temperature superconductors, strongly correlated electron systems, and heavy-fermion compounds [25, 26, 27, 28].

2.2.1 Complete mapping of the local density-of-states

In SI-STM, the tip height is adjusted by a feedback circuit until a given setpoint current I_{set} flows at a given set-point bias voltage V_{set} . This is the same as in the so-called constant-current imaging mode with conventional STMs [22], and is intended to keep the tip at a constant height above the

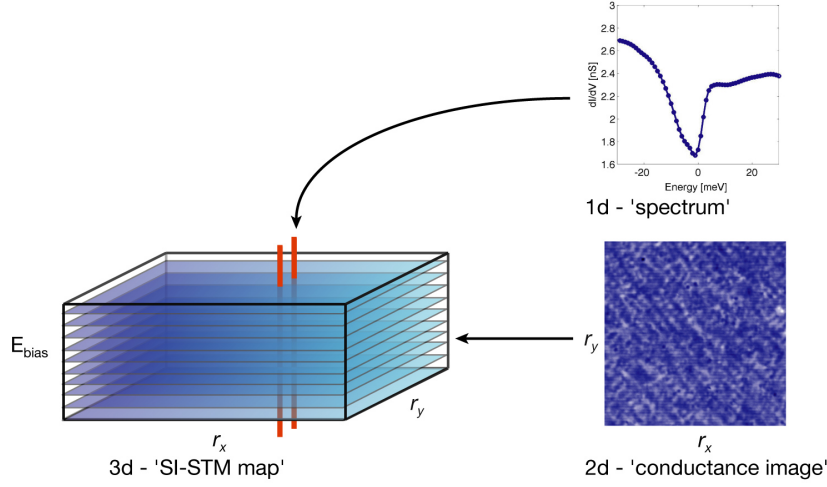


Figure 2.4: Typical SI-STM experiments map the conductance and current in the three-dimensional E_{bias} , \mathbf{r} cube. The data is typically displayed as spectra at fixed location, or as a conductance image at fixed bias voltage.

sample, since the tunneling current is approximately proportional to the exponential of the distance, $I(d) \propto e^{-\frac{d}{\alpha}}$. Then at every point of a predefined grid, the tip halts, the feedback loop is turned off, and at constant height a tunneling experiment is performed, i.e. a current $I(E_{\text{bias}})$ and a conductance $g(E_{\text{bias}}) = \frac{d}{dV}I(E_{\text{bias}})$ curve are measured. All together, this yields the conductance and current as a function of \mathbf{r} and E_B , yielding the three-dimensional datasets $g(\mathbf{r}, E)$ and $I(\mathbf{r}, E)$, as illustrated in Fig. 2.4. Simultaneously, a topographic image of the surface is taken.

Excellent descriptions of the tunneling process in SI-STM can be found in the thesis by A. R. Schmidt [29]. Here, we will merely give a brief illustration of the process.

Consider the situation of a STM tip at fixed tunneling distance to a sample with a bias of $-V$. In a simple picture, this raises the Fermi level in the tip with respect to the Fermi level in the sample, and a current flows. According to Fermi's golden rule, the total current is proportional to the number of filled states in the tip available for tunneling, the number of empty states in the sample available, and the distance-dependent tunneling matrix element $|M(d)|^2$, as illustrated in Fig. 2.3. This leads to

$$I_{\text{tunnel}}(eV) \propto \int d\varepsilon \left\{ |M(d)|^2 \cdot \{f_{FD}(\varepsilon)\rho_{\text{sample}}(\varepsilon)\} \cdot \{(1-f_{FD}(\varepsilon))\rho_{\text{tip}}(\varepsilon+eV_{\text{bias}})\} \right\},$$

with $\rho(\varepsilon)$ the respective density-of-states, d the tip-sample distance, and $f_{FD}(\varepsilon)$ the Fermi-Dirac function.

All experiments discussed in this thesis were done at 4.2 K, where the Fermi-Dirac function changes over a range of only ~ 1 meV. Consequently, we simplify the integral and limit the integration range by approximating $f_{FD}(\varepsilon)$ with a step function:

$$I_{tunnel}(eV) \propto \int_{-eV}^0 d\varepsilon \left\{ |M(d)|^2 \rho_{sample}(\varepsilon) \rho_{tip}(\varepsilon + eV_{bias}) \right\}. \quad (2.3)$$

The conductance $g = dI/dV$ is then proportional to the density-of-states of the sample,

$$\begin{aligned} g(eV) &= \frac{d}{dV} I_{tunnel}(eV) \propto \frac{d}{dV} \int_{-eV}^0 d\varepsilon \left\{ |M(d)|^2 \rho_{tip}(0) \rho_{sample}(\varepsilon) \right\} \\ &= |M(d)|^2 \rho_{tip}(0) \rho_{sample}(eV). \end{aligned} \quad (2.4)$$

Here we assumed that the density-of-states of the tip is constant, an approximation that is tested on a gold surface before every experiment. Further, we neglect the possibility of any forbidden transition from tip to sample.

Since the conductance is approximately proportional to the density-of-states, the conductance images are proportional to the *local* density-of-states, $g(\mathbf{r}, E_{bias}) \sim LDOS(\mathbf{r}, E)$.

As noted above, we want to keep the tip-sample distance d constant by adjusting the tip height to obtain a predefined (I_{set}, V_{set}) -*set-point*, i.e. a constant current I_{set} at a given bias V_{set} . We have seen, however, that the tunneling current is not only proportional to $e^{-\frac{d}{\alpha}}$, but also to the integrated density-of-states up to the bias voltage: topographic structure and electronic density both influence the tip height. It is often not possible to separate the two, and the differences in height induced by different electronic densities influences the conductance images. This often undesired phenomena is commonly called ‘set-point-effect’ or ‘set-up-effect’. More explicitly, one can substitute $|M(d)|^2 \propto e^{-\frac{d}{\alpha}}$ in equation (2.4) by using equation (2.3), leading to

$$g(eV, \mathbf{r}) \propto \frac{\rho_s(eV, \mathbf{r})}{\int_{-eV_0}^0 d\varepsilon \rho_s(\varepsilon, \mathbf{r})}, \quad (2.5)$$

for a junction set up at V_0 .

Ways to minimize the set-point-effect are taking ratio-maps [12], choosing the set-point in a range with spatially homogenous density-of-states [30], or looking for strong features in the spectra that are not influenced by the effect, such as excitation gaps [31]. Details can be found in Refs. [29, 20, 32].

2.2.2 Quasiparticle interference

A key advantage of SI-STM is the ability to simultaneously obtain information about \mathbf{r} - and \mathbf{k} -space. The latter is done by measuring the interference of scattered quasiparticles and is termed ‘quasiparticle interference’ (QPI).

In an ideal metal where the electrons are Bloch states, $\Psi_{\mathbf{k}}(\mathbf{r}) = e^{i\mathbf{k}\mathbf{r}}u_{\mathbf{k}}(\mathbf{r})$, the local density-of-states is homogenous, $\rho(\omega, \mathbf{r}) = \sum_{\mathbf{k}}|\Psi_{\mathbf{k}}(\mathbf{r})|\delta(\varepsilon(\mathbf{k}) - \omega)$ (except for modulations with the periodicity of the atomic lattice). Imagine now a material with elastic scatterers. This will mix states on the same $\varepsilon(\mathbf{k})$ -contour, leading to $\Psi_{\mathbf{k}}(\mathbf{r}) = a_1\Psi_{\mathbf{k}_1}(\mathbf{r}) + a_2\Psi_{\mathbf{k}_2}(\mathbf{r})$, with $\mathbf{k}_1, \mathbf{k}_2$ arbitrary such that $\varepsilon(\mathbf{k}_1) \stackrel{!}{=} \varepsilon(\mathbf{k}_2)$. The resulting density is

$$\begin{aligned} |\Psi_{\mathbf{k}_s}(\mathbf{r})| &= |a_1\Psi_{\mathbf{k}_1}(\mathbf{r}) + a_2\Psi_{\mathbf{k}_2}(\mathbf{r})| \\ &= |a_1u_{\mathbf{k}_1}(\mathbf{r})|^2 + |a_2u_{\mathbf{k}_2}(\mathbf{r})|^2 \\ &\quad + a_1a_2^*u_{\mathbf{k}_1}(\mathbf{r})u_{\mathbf{k}_2}^*(\mathbf{r})e^{i(\mathbf{k}_1-\mathbf{k}_2)\mathbf{r}} + a_1^*a_2u_{\mathbf{k}_1}^*(\mathbf{r})u_{\mathbf{k}_2}(\mathbf{r})e^{-i(\mathbf{k}_1-\mathbf{k}_2)\mathbf{r}}. \end{aligned}$$

It is the last two terms that give us a modulation with wavevector $\mathbf{q} = \mathbf{k}_1 - \mathbf{k}_2$, i.e. the difference between two vectors on the same energy contour.

Consequently, the Fourier transform of conductance images yields maxima at \mathbf{q} -vectors connecting constant energy $\varepsilon(\mathbf{k})$ contours. This lets us access information about the bandstructure and the scattering process of a material. Again, more details can be found in the thesis of A. R. Schmidt [29], and in Refs. [33, 34].

2.2.3 Experimental considerations

For an experiment as described, one measures typically ~ 50 energy points, on a $\sim 300 \times 300$ point \mathbf{r} -grid, in total that is 4.5 millions datapoints that have to be taken in a low temperature cryostat and in ultra-high vacuum. Thus, measuring the individual spectra in short time and with a high signal to noise ratio is imperative. The technical detail to achieve this are described C. Taylors thesis [32]. In short, a rigid head design and a thorough vibration insulation as well as well-designed electronics are a necessity (Fig. 2.6, 2.5).

The experiments described in this thesis were conducted at STM1 at Cornell University [35]. A typical map consisting of 256×256 pixel and 61 layers took three days to measure. All data was taken at 4.2 K. Samples were inserted in the cryogenic ultra high vacuum, and cleaved *in situ* below 15 K.

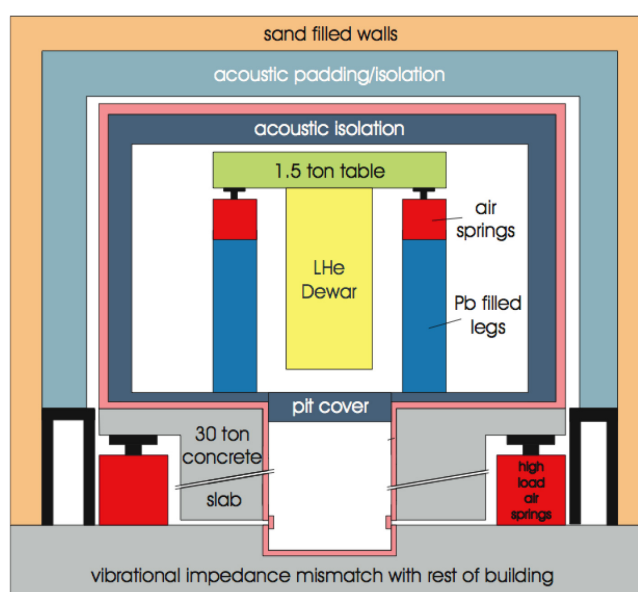


Figure 2.5: Vibration insulation. *Figure reproduced from Ref. [32].* For details, see reference.

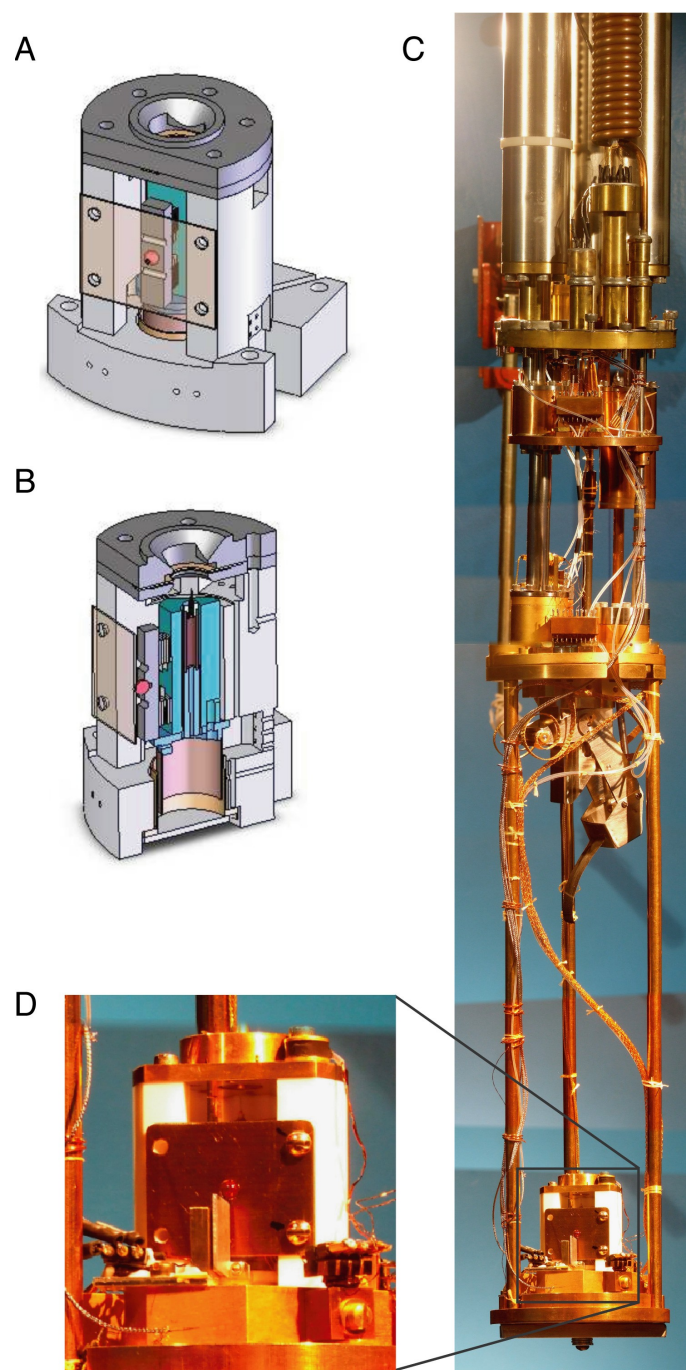


Figure 2.6: STM head and cryostat. (A,B), Schematic drawing of the STM head (*CAD drawing by C. Taylor [32]*). (C,D) Photograph of the cryostat and head. For instrumental details, see Refs. [35, 32]

Chapter 3

The bilayer ruthenate $\text{Sr}_3\text{Ru}_2\text{O}_7$

The first part of this thesis, the electronic structure of $\text{Sr}_3\text{Ru}_2\text{O}_7$, is covered in chapters 3 to 6. Here, we will give a short introduction to the material. We will first survey the family of strontium ruthenate perovskites, then discuss the geometric and electronic structure, and finally review the particular phase diagram and theoretical models thereof.

3.1 The strontium ruthenate family

The perovskite $\text{Sr}_3\text{Ru}_2\text{O}_7$ is the $n = 2$ bilayer member of the strontium ruthenate family with Ruddlesden-Popper structure, $\text{Sr}_{n+1}\text{Ru}_n\text{O}_{3n+1}$. The parameter n is equal to the number of RuO_6 octahedra layers in-between SrO spacer layers. Since the electronic structure is dominated by the former, this also changes the resistivity anisotropy: the ratio $R_{\text{in-plane}}/R_{\text{out-of-plane}}$ for the single-layer $n = 1$ compound is above 1000 [37], for the $n = 2$ bilayer material it is around 300 [36], and $n = \infty$ has three-dimensional conductance behavior. Fig. 3.1 shows a schematic picture of different strontium ruthenates listed here:

The single layer Sr_2RuO_4 ($n = 1$) is famous for its unconventional, most likely p -wave superconductivity. It is isostructural to the high T_c superconductor $\text{La}_{2-x}\text{Sr}_x\text{CuO}_4$, consisting of RuO_6 octahedra layers with SrO layers in-between, leading to a very two dimensional electronic structure [38].

The bilayer $\text{Sr}_3\text{Ru}_2\text{O}_7$ ($n = 2$) is a paramagnet with RuO_6 octahedra bilayers, spaced by SrO layers. It shows metamagnetic transitions and associated criticality, and it undergoes a nematic phase transition; more about $\text{Sr}_3\text{Ru}_2\text{O}_7$ follows in the following sections.

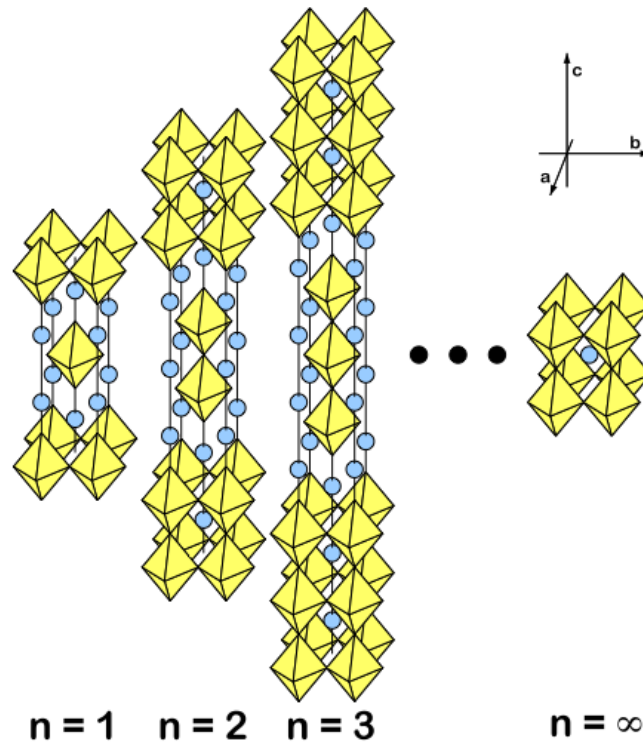


Figure 3.1: Schematic representation of the Ruddlesden-Popper series $\text{Sr}_{n+1}\text{Ru}_n\text{O}_{3n+1}$. Showing from left to right Sr_2RuO_4 ($n = 1$), $\text{Sr}_3\text{Ru}_2\text{O}_7$ ($n = 2$), $\text{Sr}_4\text{Ru}_3\text{O}_{10}$ ($n = 3$) and SrRuO_3 ($n = \infty$). The yellow octahedra represent the RuO_6 octahedra with the Ru atoms in its centers, and the blue spheres represent the Sr ions. The crystallographic axes are given in the top right corner. *Figure reproduced from Ref. [36].*

From the trilayer layer $\text{Sr}_4\text{Ru}_3\text{O}_{10}$ ($n = 3$) to SrRuO_3 ($n = \infty$), the ruthenates have mostly three dimensional electronic properties. SrRuO_3 is an itinerant ferromagnet with a Curie temperature $T_c = 160$ K [39].

3.2 Crystalline structure and synthesis

$\text{Sr}_3\text{Ru}_2\text{O}_7$ consist of RuO_6 octahedra, arranged in bilayers, with SrO spacer layers in-between (Fig. 3.2). The nearest Ru-Ru distance is 3.87 \AA [40, 41]. Every RuO_6 octahedron is rotated by 6.8° around the c -axis, with opposite directions for neighboring octahedra. This doubles the unit-cell (Fig. 3.2, left), but every bilayer still possesses C_4 -symmetry. However, since every bilayer has an opposite rotating pattern, the C_4 symmetry for the whole

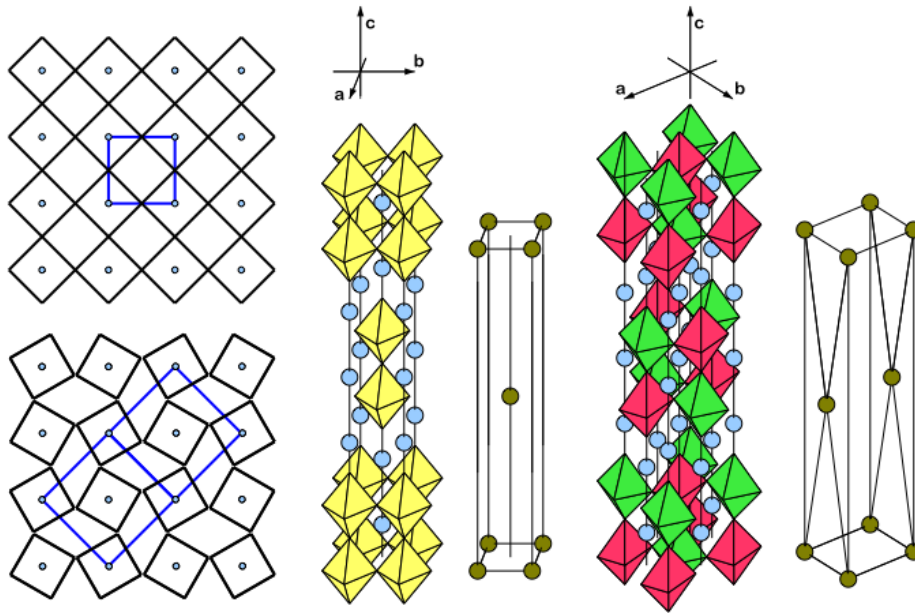


Figure 3.2: Schematic representation of the octahedron rotation in $\text{Sr}_3\text{Ru}_2\text{O}_7$. *Left*, In-plane representation of the octahedra before rotation, *top*, and after, *bottom*. The basal unit cell is shown in blue. *Middle*, Undistorted lattice unit cells. *Right*, Distorted unit cell. Yellow octahedra are not rotated, the green are rotated clockwise in the ab -plane, and the red counter-clockwise. The respective crystallographic axes are represented, the ones for the distorted lattice rotated by 45° around the c -axis. *Figure reproduced from Ref. [36]*.

crystal is lost, as can be seen from Fig. 3.2, right. It is noteworthy that even though the octahedra in single layer Sr_2RuO_4 are not rotated in the bulk under ambient conditions, they will do so at the surface [42, 43].

The first $\text{Sr}_3\text{Ru}_2\text{O}_7$ crystals were grown in Pt-crucibles using self-flux [44], and were thought to be ferromagnetic, most likely due to ferromagnetic $\text{Sr}_4\text{Ru}_3\text{O}_{10}$ intergrowth [45]. Later, Ikeda *et al.* [45] and Perry, Maneo, *et al.* [46, 47] observed paramagnetic behavior after they used an image furnace to grow samples with significantly higher purity. This method uses focused light from halogen bulbs to melt rods prepared from powder that subsequently crystallize to single crystal $\text{Sr}_3\text{Ru}_2\text{O}_7$. It is important to have perfect stoichiometric ratios of constituents in the end product, but due to uneven loss during the process, one has to use different nominal concentrations to begin with – one of the many parameters that decide over the quality of the crystals.

State-of-the-art $\text{Sr}_3\text{Ru}_2\text{O}_7$ crystals have residual resistivities below $0.5 \mu\Omega\text{cm}$, and are almost defect and impurity free, as can be seen by SI-STM ([48], chapter 5) and dHvA [36] — it is in those crystals that one can observe the nematic phase introduced in section 3.3. The main challenge is now to suppress the formation of any intergrowth phase, such as $\text{Sr}_4\text{Ru}_3\text{O}_{10}$ or SrRuO_3 . In Ti-doped crystals they can make up molar fractions of several percentages, while high-quality pure crystals have values below one percent [49]. Recent scanning electron microscopy by L. Fitting Kourkoutis *et al.* confirmed the existence of missing layers and intergrowth phases [50].

The crystals used for this thesis were grown by A. Gibbs, R. S. Perry and J. Farrell from the Mackenzie group in St. Andrews. The crystals were characterized by J.-F. Mercure.

3.3 The phase diagram: magnetism, criticality, and nematicity

Let us first review the low temperature, zero magnetic field properties of $\text{Sr}_3\text{Ru}_2\text{O}_7$. Under these conditions, it is a paramagnetic metal. The electronic structure follows Fermi-liquid theory and is mainly two dimensional, the resistivity anisotropy between transport along/perpendicular to the bilayers is around 300 at 0.3 K [36] [46, 52, 51]. The magnetic properties of $\text{Sr}_3\text{Ru}_2\text{O}_7$ are characterized by a tendency towards ferromagnetism, as shown by its high Wilson ratio $R = 10$ [56]. Further, $\text{Sr}_3\text{Ru}_2\text{O}_7$ becomes ferromagnetic under uniaxial pressures of around 1 GP [56]. At very high temperatures (> 200 K), $\text{Sr}_3\text{Ru}_2\text{O}_7$ shows a Curie-Weiss behavior [56]. Another noteworthy thermodynamic property is the high value of specific heat, $\gamma = 110 \text{ mJ molRu}^{-1} \text{ K}^{-2}$, indicative of a high density of states at the Fermi level, and very different to single layer Sr_2RuO_4 where $\gamma = 38 \text{ mJ molRu}^{-1} \text{ K}^{-2}$ has been reported [37].

The reason $\text{Sr}_3\text{Ru}_2\text{O}_7$ has attracted so much attention lies in its particular phase diagram. The high Wilson ratio is indicative of a proximity to a ferromagnetic instability, and indeed, a metamagnetic transition is found at low temperature and a field of ~ 7.8 T along the c -axis, becoming broader with higher temperature [46, 47] (Fig. 3.3). Grigera *et al.* [52, 51] studied the metamagnetic properties by measuring the AC magnetic susceptibility as a function of magnitude and angle of the magnetic field, and temperature. They discovered that at certain angles and temperatures, the crossover becomes a first order phase transition, as shown by a dissipative peak in the imaginary part of the magnetic susceptibility. Further, by varying angle and magnitude of the field, one can suppress the highest temperature of the

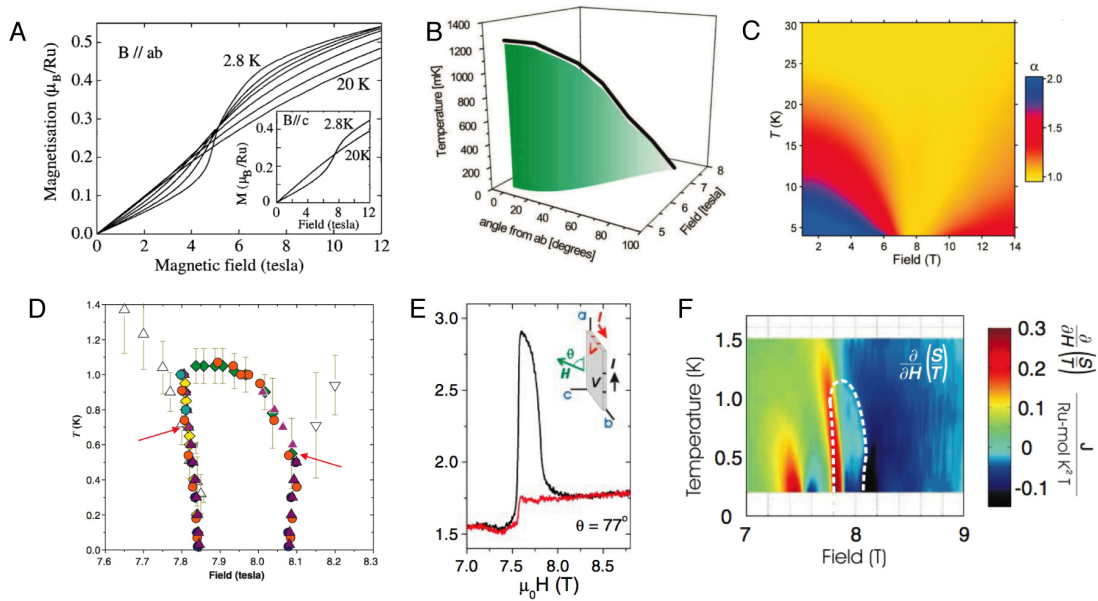


Figure 3.3: Thermodynamic measurements leading to discovery and characterization of the particular phase diagram of $\text{Sr}_3\text{Ru}_2\text{O}_7$. (A), Metamagnetism with $B \parallel ab$. The crossover gets smoother with higher temperature. (B), The first order phase transition sheet leading to a putative quantum critical endpoint at 8 T, 90° . (C), The resistivity shows the typical cone of non-quadratic behavior above the putative quantum critical endpoint. (D), Boundary of the novel phase. The shape of the phase boundaries have been confirmed by various techniques. (E), Anisotropic resistivity in the nematic phase. (F), Entropy landscape showing the higher entropy in the nematic phase (white line). Panels reproduced from Refs. [46, 51, 52, 53, 54, 55], respectively. For details, see references.

phase transition sheet towards zero at 8 T and a field direction close to the c -axis. Note that this is the endpoint of a line of critical endpoints that can be tuned towards zero, and not the phase transition line itself, as in the case of ‘conventional’ quantum critical points [57]. Consequently, Grigera *et al.* called this a ‘quantum critical endpoint’. Fig. 3.3B shows the first order transition sheet and the quantum critical endpoint.

Criticality is also observed in transport measurements. In zero magnetic field, there is a crossover from Fermi-liquid like T^2 resistivity to non-Fermi-liquid like linear resistivity. This transition is suppressed with increased magnetic field, until it goes towards zero at a field of ~ 8 T parallel to the c -axis, close to the quantum critical endpoint. There is the typical cone of non-Fermi liquid behavior above the putative quantum critical endpoint

made visible by plotting the exponent α of the resistivity, $\rho \sim T^\alpha$, as a function of temperature and field (Fig. 3.3C).

Perry *et al.* were later able to increase the sample quality so that the residual resistivity was below $0.4 \mu\Omega\text{cm}$. Grigera *et al.* [53] found that in such ultra-pure samples, the putative quantum critical point is hidden by the formation of a novel phase that exists in a small, muffin-shaped region below 1 K. Borzi *et al.* [54] and Rost *et al.* [55] characterized this phase (Fig. 3.3) and found that this phase exhibits a transport anisotropy without a significant distortion of the underlying lattice, a characteristic of a nematic electronic liquid phase. This phase has higher entropy than the surrounding phases [55] (Fig. 3.3D,E), different than one could naively expect for a liquid exhibiting additional directional order.

$\text{Sr}_3\text{Ru}_2\text{O}_7$ seems to be an ideal system to study the criticality and the related nematicity: the magnetic field is a relatively easy parameter to tune (other than e.g. doping or pressure), and due to the layered structure and the possibility of cleaving the sample *in situ* to reveal pristine, atomically flat surfaces, the material is accessible for various experimental techniques. Not surprisingly then, $\text{Sr}_3\text{Ru}_2\text{O}_7$ has attracted much attention from both experimentalists and theorists (e.g. Refs. [58, 59, 60, 61, 62, 63, 64]).

3.4 Theoretical models

Before the nematicity was experimentally discovered, early theoretical models of the $\text{Sr}_3\text{Ru}_2\text{O}_7$ phase diagram concentrated on metamagnetism and criticality. Binz and Sigrist [58] discovered that a strong enough maxima in the density-of-states near the chemical potential, e.g. a van Hove singularity, induces a first order metamagnetic phase transition and qualitatively reproduces the experimental phase diagram [58]. This is still the starting point for many models [59, 60, 61], and the existence of a van Hove singularity has been confirmed by ARPES [65]. Later, an Hamiltonian that favors forward scattering was introduced to qualitatively reproduce the experimental phase diagram. Puetter *et al.* [66] and Fischer *et al.* [64] used this method with mainly d_{xy} derived bandstructure models. A different route is taken in recent work from Raghu *et al.* [62] and Lee *et al.* [63] who concentrate on the quasi one-dimensional Ru d_{xz} , d_{yz} orbitals and the related α_1 , α_2 bands and proposed different coulomb repulsion for electrons at the same site in the same orbital (U) versus electrons at the same site but in different orbitals (V). In the magnetic field, this leads to an uneven occupation of the orbitals with orthogonal directionality and thus nematicity. Common to all recent work is the use of spin orbit coupling to explain the dependence of the nematicity

on the magnetic field angle.

Despite the apparent success of these models, many questions remain open. First, the differences to single layer Sr_2RuO_4 , which does not exhibit nematicity, are not always addressed. Second, in some models, the parameters have to be tuned very precisely and to unexpected values in order to get the the metamagnetic transition at the right magnetic field. Third, it is often not clear to what degree the bandstructure assumed and/or predicted matches the experimental data. As we will present in chapter 4, there is an unusual renormalization of the bandstructure that cannot be predicted by simple tight binding models, and is not yet included in any theoretical models of $\text{Sr}_3\text{Ru}_2\text{O}_7$. Perhaps some of these questions will be answered when it becomes possible to microscopically image the electronic states in the nematic phase by orbital imaging or \mathbf{k} -space Fermi surface distortion [27].

Chapter 4

The electronic structure of $\text{Sr}_3\text{Ru}_2\text{O}_7$ seen by ARPES

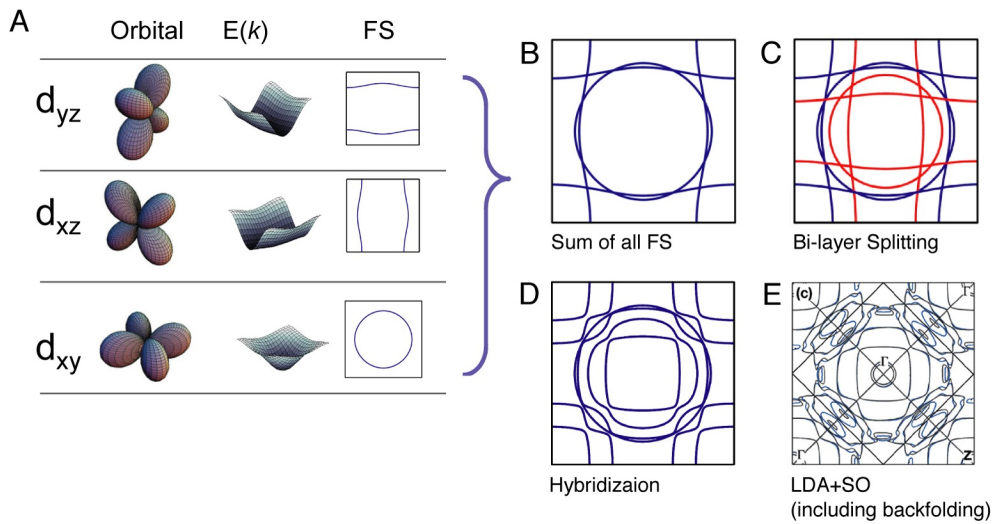


Figure 4.1: (A), The relevant Ru d_{xy} , d_{xz} , d_{yz} orbitals, as well as their dispersions $E(\mathbf{k})$ and Fermi surfaces that can be expected from tight binding models using Sr_2RuO_4 hopping parameters. The following simplified arguments lead to an approximation for the $\text{Sr}_3\text{Ru}_2\text{O}_7$ Fermi surface: Adding the Fermi surfaces from the three mentioned orbitals together (B), introducing a bilayer splitting in the $d_{xz,yz}$ derived bands (C), hybridizing (D), and back-folding. This bandstructure is, despite the simplified model, similar to the LDA+SO bandstructure (E) and ARPES (*panel reproduced from Ref. [65]*). Later, we will show that this is not the case for the Fermi velocities.

The low energy electronic states of $\text{Sr}_3\text{Ru}_2\text{O}_7$ are mainly composed of Ru t_{2g} d_{xy} , $d_{xz,yz}$ and O $p_{x,y,z}$ orbitals. In a simple tight binding model,

the d_{xy} orbitals give a circular Fermi surface, while the $d_{xz,yz}$ orbitals give one-dimensional sheets orthogonal to each other. Fig. 4.1 shows the relevant orbitals and their respective tight binding Fermi-surfaces. These three bands give, after hybridization, a Fermi surface very close to the one measured for single layer Sr_2RuO_4 [67]. In bilayer $\text{Sr}_3\text{Ru}_2\text{O}_7$, one has to duplicate the bands due to bilayer splitting and then backfold the bands due to the smaller Brillouin zone (c.f. Fig. 3.2). Fig. 4.1A-E show a cartoon illustrating this set of very simplified arguments that lead to a Fermi surface that looks surprisingly similar to LDA+SO calculations (Fig. 4.1F).

4.1 Fermi surface mapping

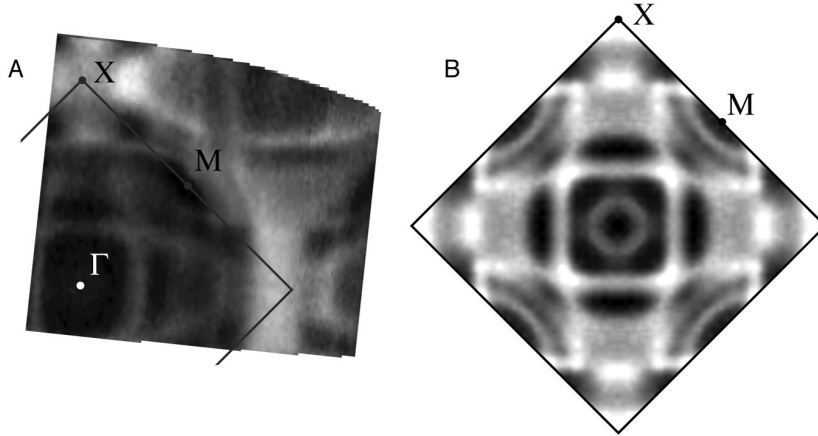


Figure 4.2: (A), Raw ARPES data taken on $\text{Sr}_3\text{Ru}_2\text{O}_7$ with photocurrent intensity integrated over an energy range of ± 2 meV, plotted in gray scale. The black box marks the first Brillouin zone of the orthorhombic lattice. X denotes the surface projection of R and M that of a midpoint between two Γ points (Z or S). (B), We symmetrized the data across the a -, b -axis and the diagonal to suppress direction dependent matrix element effects. ((A) and (B) are measurements from different samples.)

¹Fig. 4.2 shows the ARPES photocurrent intensity integrated over an energy window of ± 2 meV around E_{Fermi} plotted in a false-color image to map the Fermi surface. Fig. 4.2A shows the raw data, Fig. 4.2B is symmetrized to suppress direction dependent matrix element effects.

¹We published some of the results discussed here in Ref. [65]. Parts of this chapter follow closely the published manuscript.

Possibly due to surface effects, different samples show slightly (up to 1 meV) different Fermi levels. This effect is not observable with most photoelectron detectors due to the limited resolution, and for most other compounds, it would be irrelevant due to the high Fermi velocities. For $\text{Sr}_3\text{Ru}_2\text{O}_7$ however, we have to take this into account. We will note this possible uncertainty of ± 1 meV whenever we give exact energy levels of bandstructure features measured by ARPES.

Analyzing the Fermi surface and some high symmetry direction cuts, it is possible to identify at least 5 Fermi pockets, marked and labeled in Fig. 4.3B. They agree well with LDA calculations (Fig. 4.3C), allowing us to identify the orbital character of the sheets through comparison with the corresponding LDA+SO bands (c.f. section 4.2.4). We will briefly describe the individual bands below, starting with the innermost pocket.

The δ pocket is almost circular. It is the only pocket that stems from the $d_{x^2-y^2}$ orbital of the e_{2g} manifold, with some additional d_{xy} contribution. (All other bands crossing the Fermi level stem from the t_{2g} manifold.) This band is above the Fermi level in single-layer Sr_2RuO_4 . The δ pocket has a very low Fermi velocity and hybridizes with the α_1 band above E_{Fermi} (Fig. 4.9).

The α_1 and α_2 bands stem from the $d_{xz,yz}$ orbitals, which are highly one-dimensional (Fig. 4.1A). Bilayer splitting and subsequent hybridization leads to the cross- and square-shaped, hole-like α_1 , α_2 bands. We will call the α_1 band, which is lower in energy, ‘bonding’ and the α_2 band ‘antibonding’, in loose reference to two-atom-molecules.

The γ_1 band is an electron pocket. It has mostly d_{xy} character (on the arc) and some $d_{xz,yz}$ character. A shoulder in the photocurrent intensity along ΓM (Fig. 4.5, [65]) shows that there is a small bilayer splitting of this pocket, consistent with LDA+SO results.

The β band is a small, lens-shaped electron pocket at the zone boundary around the M point. Its main orbital character is d_{xy} .

The γ_2 band has its maxima slightly below the Fermi level, at around -1 ± 1 meV. However since different samples yield a shift in the Fermi-level of around ± 1 meV, we can not unambiguously decide whether this band crosses the Fermi-level.

We compared the areas of these pockets with dHvA result [47, 68, 69, 70], and the agreement of surface sensitive ARPES with this bulk-sensitive probe

proves that the data shown here is bulk-representative. More about dHvA will follow in section 4.4.

It is possible that some bands create too weak photocurrent to be detected by ARPES and are therefore missed. An indication on whether one measures the complete Fermi surface is to test Luttinger's theorem, which, in this case, states that the total area of electron pockets minus the total area of hole pockets is an even integer. (Of course this does not exclude that there might be several additional pockets that add up to zero, or additional but very small pockets). To calculate the Luttinger area, one has to take into account the bilayer splitting. For the splitting leading to the α_2 , α_1 bands, the energy difference is large, and ARPES can easily resolve the bands. For the γ_1 band, a shoulder in the data indicates a small bilayer splitting (Fig. 4.5). The ARPES data for the δ , γ_2 , β bands does not show any bilayer splitting, however, comparison with LDA+SO indicates that only the first of these has a small bilayer splitting. Further, we assumed a small bilayer splitting of the γ_2 band to match the value of the specific heat, as outlined below. Adding the areas of the pockets, with a sign according to their electron/hole character, counted with the number of times with which they occur in the Brillouin zone, and including an additional factor 2 for the bilayer-split bands, we get $2(-A_{\alpha_1} - A_{\alpha_2} + 2A_{\beta} + 2 \cdot 4A_{\gamma_1} + 2 \cdot 4A_{\gamma_2} + 2 \cdot A_{\delta}) = 0.24(25)$ electrons/RuO₂, or $-0.06(6) + 2n$, $n \in \mathbb{N}$ [65]. This is in accordance with the Luttinger theorem.

Using the same assumptions, one can calculate the electronic specific heat. The sum of masses $\Sigma m^* = 171 m_e$, and consequently $\gamma = 127 \text{ mJ molRu}^{-1} \text{ K}^{-2}$ [65]. This agrees well with the specific heat measured by direct probe, $110 \text{ mJ molRu}^{-1} \text{ K}^{-2}$ [56]. If one would assume that the γ_2 band did not cross the Fermi level, the calculated specific heat would be $67 \text{ mJ molRu}^{-1} \text{ K}^{-2}$. This indicates that the γ_2 band indeed crosses the Fermi level.

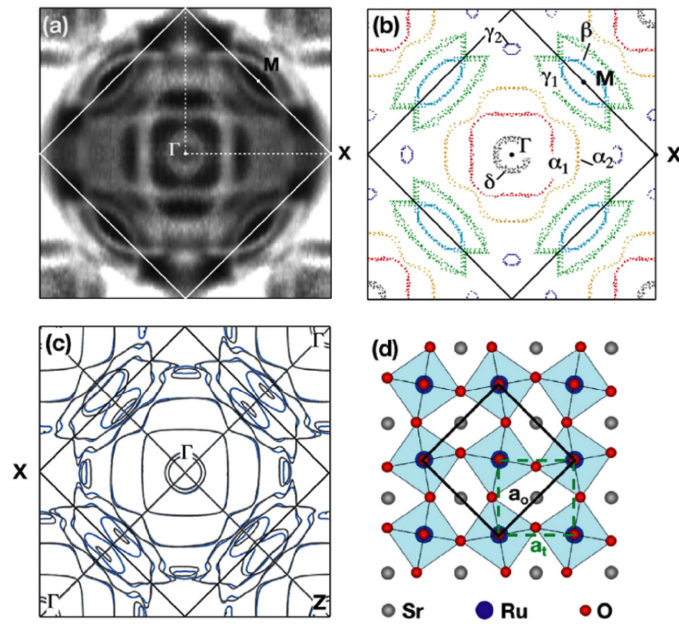


Figure 4.3: Fermi surface of $\text{Sr}_3\text{Ru}_2\text{O}_7$. (a) shows the experimental data taken in the first quadrant of the larger tetragonal Brillouin zone and symmetrized with respect to the Ru-Ru nearest neighbor directions. The white square marks the orthorhombic Brillouin zone. (b), Fermi surface contours extracted from the data shown in (a). (c), LDA calculation for the basal plane ($k_z = 0$, black) and mid-plane ($k_z = \frac{1}{4}$, blue). (d), Schematic structure of a single RuO_2 plane illustrating the unit-cell doubling due to a 6.8° rotation of the RuO_6 octahedra [20]. a_t denotes the Ru-Ru nearest neighbor distance and a_o the in-plane lattice constant of the orthorhombic unit cell, respectively. *Figure reproduced from Ref. [65].*

4.2 Strong k - and orbital dependent quasiparticle renormalization

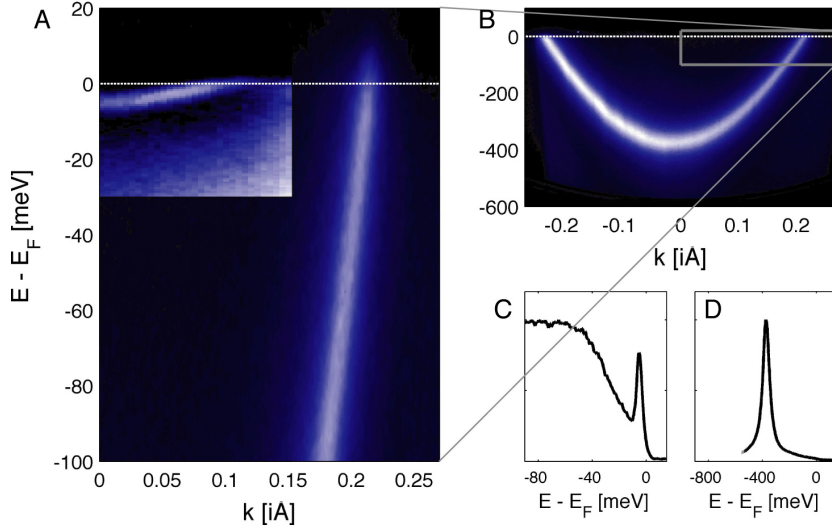


Figure 4.4: Comparison of the surface state of Cu(111) as an example of nearly-free electron system, and the δ band in $\text{Sr}_3\text{Ru}_2\text{O}_7$, a highly correlated electron system. (B), ARPES photocurrent plot of the Cu(111) surface state. The gray box shows the area that is magnified in (A). The Cu(111) is shown again in (A), with the $\text{Sr}_3\text{Ru}_2\text{O}_7$ δ band plotted in the same axis. Its bandwidth is around 60 times smaller. (C,D), Photocurrent spectra from the Γ point. The copper band has a the spectral weight concentrated in a clear peak, while the spectral weight of the δ band is distributed between a quasiparticle peak and an incoherent part ('peak-dip-hump' shape).

Fig. 4.4(A) is a false color plot of the flat δ band in $\text{Sr}_3\text{Ru}_2\text{O}_7$. In the same axis, the free-electron like surface state on Cu(111) is displayed. It is immediately clear that they have very different band-widths; the band minima differ by a factor of around 100 while the Fermi vectors are similar. This extremely strong renormalization shows that the quasiparticles in $\text{Sr}_3\text{Ru}_2\text{O}_7$ are far from being 'nearly-free' electrons in a Fermi gas. The spectra of Cu(111) and $\text{Sr}_3\text{Ru}_2\text{O}_7$ underline the difference between the two systems: while the free-electron-like band in Cu shows a narrow peak at the band energy, the spectra of the δ -band in $\text{Sr}_3\text{Ru}_2\text{O}_7$ show a peak-dip-hump shape typical for strongly correlated electron systems [14].

From this, it is evident that the quasiparticles in $\text{Sr}_3\text{Ru}_2\text{O}_7$ differ greatly from free electrons that can be treated independently without any interac-

tions. In the following sections we will describe the strong renormalization of $\text{Sr}_3\text{Ru}_2\text{O}_7$ quasiparticles in more detail and will discuss the physical implications thereof.

4.2.1 Renormalization factors in $\text{Sr}_3\text{Ru}_2\text{O}_7$

Fig. 4.5 shows the quasiparticle dispersion in $\text{Sr}_3\text{Ru}_2\text{O}_7$ along two high-symmetry directions. The most striking observation is the extremely flat bandstructure with bands confined to a narrow energy range of only ~ 5 meV around E_{Fermi} , present mostly along the ΓX direction. Some bands exhibit Fermi velocities more than an order of magnitude lower than those of the single layer compound Sr_2RuO_4 , and more than 30 times lower than the non-interacting Fermi-velocities we calculated by *ab-initio* calculations. This set of strongly renormalized bands coexists with a set of much weaker renormalized bands, observed mostly at high energies and along ΓM . The extent of the renormalization is ‘binary’ in the sense that bands are either *strongly* ($v_{\text{exp}}/v_{\text{LDA}} \approx 19$ to 32) or *weakly* ($v_{\text{exp}}/v_{\text{LDA}} \approx 6$ to 11) renormalized, but not in between. The bands in Fig. 4.5 are labeled in orange (yellow) for strong (weak) renormalization. Further, the energy scale on which the bands become incoherent and quasi-vertical (blue arrow in Fig. 4.5(b)) is around 20 meV, much lower than in the cuprates [71].

To gauge the strength of the renormalization, we compare the electronic structure of $\text{Sr}_3\text{Ru}_2\text{O}_7$ with its single-layer sister compound Sr_2RuO_4 (Fig. 4.5(c)). The bandstructure of the former differs due to the lack band-splitting and back-folding induced by the bilayer and octahedron rotation [70, 66]. However, the Fermi velocities should not be strongly affected by either. Thus we expect values similar to single layer Sr_2RuO_4 , where the bands have electron masses of 3 to 6 m_e , and renormalization factors of $m^*/m_{\text{LDA}} \approx 2.7$ for the α^{214} -, β^{214} -sheets and $m^*/m_{\text{LDA}} \approx 6$ for the γ^{214} -sheet. Here, the renormalization is constant over a larger energy range, and has been attributed to electron–electron interactions [67, 72, 73]. Fig. 4.5 compares the single and bilayer compounds illustrating that the dispersion in the former is similar to the weakly renormalized bands in the latter, but that there is a striking difference to the strongly renormalized bands. This suggests that there are additional non-trivial mechanisms in $\text{Sr}_3\text{Ru}_2\text{O}_7$ that have a strong effect at low binding energies and for some bands only, possibly the same mechanisms that lead to the electronic nematic liquid observed in $\text{Sr}_3\text{Ru}_2\text{O}_7$ but not in Sr_2RuO_4 .

The different Fermi velocities are very notable along the ΓX direction, where the α_2 band hybridizes with the γ_2 band and disperses very weakly up to the X point. The dispersion of this sheet spans over more than half

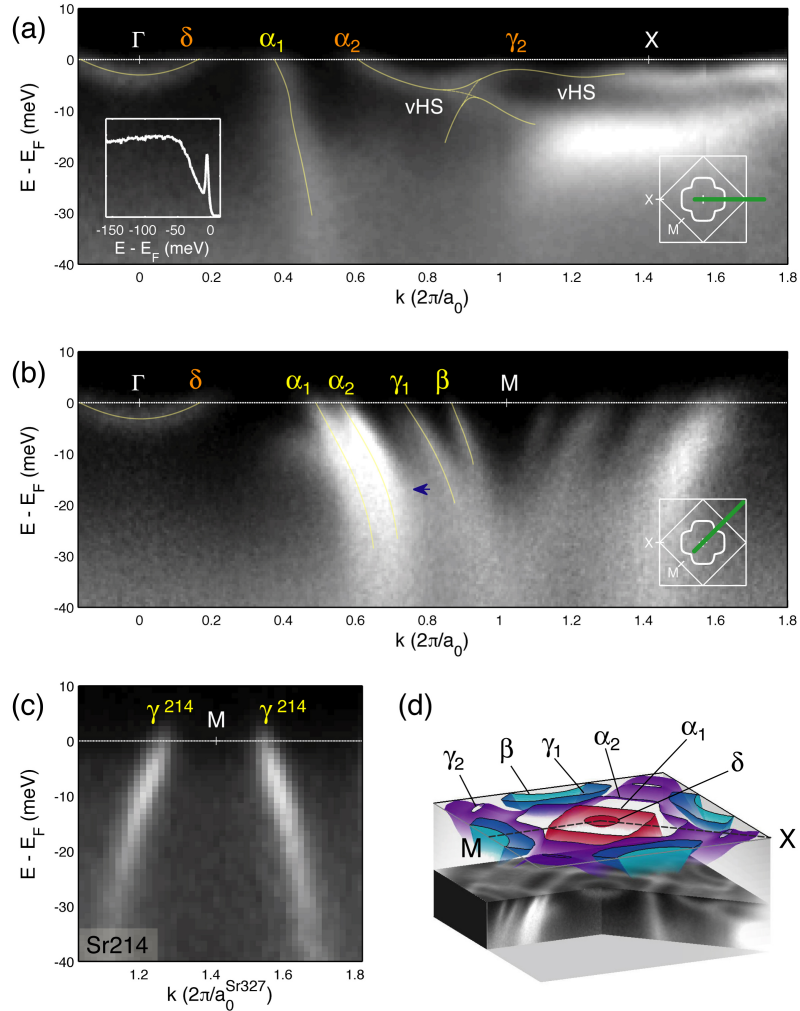


Figure 4.5: (a, b) Quasiparticle dispersion along the ΓM and ΓX high symmetry directions (defined in the insets). The white lines are guides to the eye. Bands with renormalization factors in the range of 19 to 32 (6 to 11) are labeled with red (yellow) font. Two van Hove singularities are labeled. Note the peak-dip-hump shape of the spectra (inset) characteristic for strong correlations. The blue arrow in (b) marks the energy scale at which the bands become quasi-vertical. (c) The γ^{214} band of Sr_2RuO_4 . Despite manageable differences in atomic structure, the renormalization is about an order of magnitude lower than some of the corresponding bands in $\text{Sr}_3\text{Ru}_2\text{O}_7$. (d) Sketch of the complete low-energy band structure in $\text{Sr}_3\text{Ru}_2\text{O}_7$ up to E_{Fermi} . Note that in this sketch we shifted the γ_2 band slightly above the Fermi level for better visibility.

of the Brillouin zone and stays confined well above the -10 meV level. It is more than ~ 25 times flatter than the non-interacting band we calculated by LDA+SO and some sections are almost horizontal. The band includes two van Hove singularities, c.f. section 4.3 and Fig. 4.5(a). In contrast, we find that the α_1 sheet, which is in close proximity, exhibits much weaker renormalization, as do most of the bands at higher energies or along ΓM .

The binary character of the renormalization is more obvious when the ARPES bandstructure is compared to the LDA+SO bandstructure. Fig. 4.6 is a false-color intensity plot of the ARPES photocurrent with LDA+SO overlaid. LDA+SO is plotted twice: once globally renormalized by a factor of 4, and a second time globally renormalized by a factor of 20. Some bands follow the former, some bands the latter, illustrating again the binary character of the renormalization.

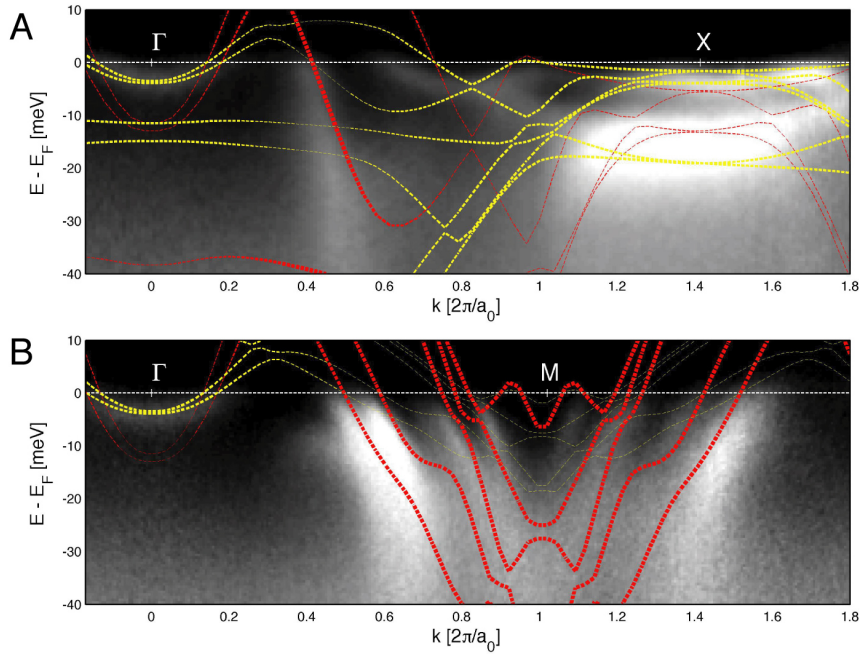


Figure 4.6: Comparison between the ARPES bandstructure and LDA calculation. (A,B) are ARPES intensity plots in the ΓX , ΓM direction, respectively. LDA+SO calculations are overlaid; the red curves are renormalized by a factor of 5 and track the ‘light’ bands, the yellow curves are renormalized by a factor of 20 and track the heavy bands. LDA+SO calculations by E. Rozbicki [74].

4.2.2 Direction dependent renormalization

Unexpected is also the contrast between the two high-symmetry directions. Along ΓX , the data mostly show the discussed coexistence of strongly and lightly renormalized low-energy quasiparticle excitations. Along ΓM , the quasiparticles generally remain lighter. Notably, this direction dependence can even be observed in a *single* sheet. Fig. 4.7 shows the Fermi surface contour of the α_2 band, which dominates the quasiparticle scattering interference seen in SI-STM [27], plays a vital role in recent theoretical models [62, 75], and undergoes the largest volume change in the metamagnetic transition [76]. Our LDA calculations suggest that this sheet has quasi-one-dimensional $d_{xz,yz}$ character and a nearly isotropic bare Fermi velocity, the same holds for the bandstructure used in recent theoretical models [62, 75]. ARPES, however, measures a striking anisotropy of the renormalization (Fig. 4.7). This becomes clear from the dispersion plots shown in Fig. 4.7(b,c), where we overlay an LDA+SO dispersion, globally compressed by a factor of 6 as seen in single layer Sr_2RuO_4 . The LDA+SO band reproduces the Fermi velocity along ΓM but strongly overestimates it along ΓX . In order to correlate the velocity renormalization with the shape of the Fermi surface we analyzed a large number of cuts extracted from a three-dimensional data-set. The result is given in Fig. 4.7(a) by red arrows with lengths proportional to the inverse Fermi velocity. This shows that the strongly renormalized sections stem from the $d_{xz,yz}$ orbitals with higher bilayer split energy level (antibonding), while the weakly renormalized sections that stem from the lower bilayer split energy level (bonding); both are drawn in the background. Similarly, the α_1 band that also stems from the bonding band also exhibits weak renormalization. Intriguingly, the high renormalization also tracks sections of the bands that stem from electrons that are concentrated less in the RuO plane and more at the apical O in-between bilayers (Fig. 4.10). We will comment on that later in section 4.2.4.

4.2.3 Low energy kink in the α_1 -band

At the same energy scale of ~ 5 meV noted above, we observe a kink in the dispersion of the α_1 sheet (see Fig. 4.8). Fits to momentum distribution curves show the canonical s-shaped dispersion with high- and low-energy parts extrapolating to the same Fermi wave vector, the behavior expected for coupling of electronic quasiparticle to a bosonic mode [16, 17, 78]. The coupling parameter $\lambda' = v_{\text{high}}/v_{\text{low}} - 1 \approx 1 - 2$ is of intermediate strengths, though the data do not allow us to give a precise value. Note that a mode energy around 5 meV is approximately an order of magnitude lower than seen

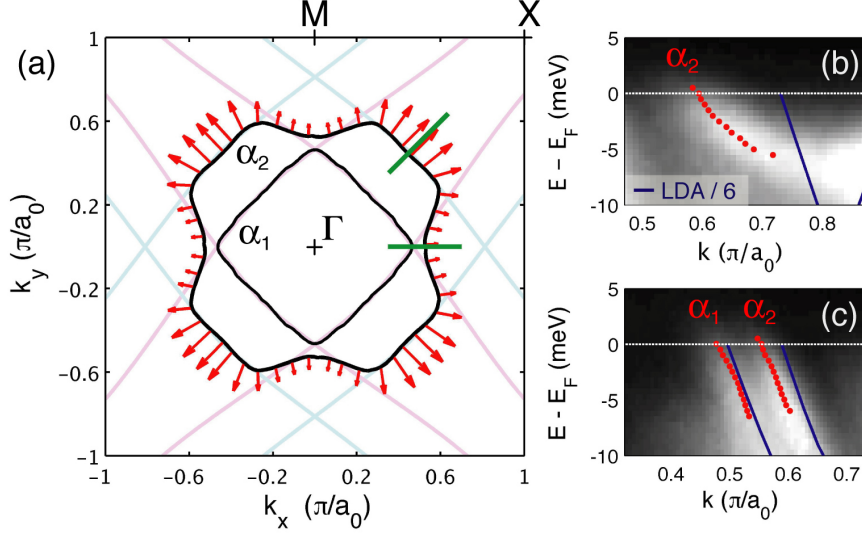


Figure 4.7: (a) Renormalization map for the α_2 Fermi surface sheet. The length of the red arrows is proportional to the ratio $v_{\text{LDA}}/v_{\text{F}}$, i.e. longer arrows indicate a higher renormalization. The bilayer-split bands from the one-dimensional d_{xz} , d_{yz} orbitals before hybridization are drawn in the background in blue (bonding) and pink (anti-bonding). Note that the strong renormalization is mainly on the anti-bonding band and vice versa. (b,c), Image plots comparing the quasiparticle dispersion with a globally renormalized LDA+SO calculation, using a factor similar to the one used in Sr_2RuO_4 . The Brillouin zone locations of the cuts (b,c) are marked by green lines in (a).

in various ARPES studies on cuprates [18, 79]. We confirmed through simulations that the finite energy resolution and temperature of the experiment cause only a minor distortion of the extracted dispersion, and reproduced the kink-feature on multiple cleaves from different growth batches. However, its precise strengths appears to depend on the surface quality of individual cleaves and its measurement is further complicated by a hybridization between the δ and α_1 pockets above the Fermi level. Cuts along ΓX , with the intensity above E_{Fermi} made visible by normalization [80] show clearly that the δ - and α_1 -bands connect at around +3 meV (Fig. 4.9). Note that this can lead to an flattening of the α_1 -band towards the Fermi level, but not to a pronounced kink. We thus believe that there is a low energy kink in the α_1 band, but caution to give precise values about the strength and energy.

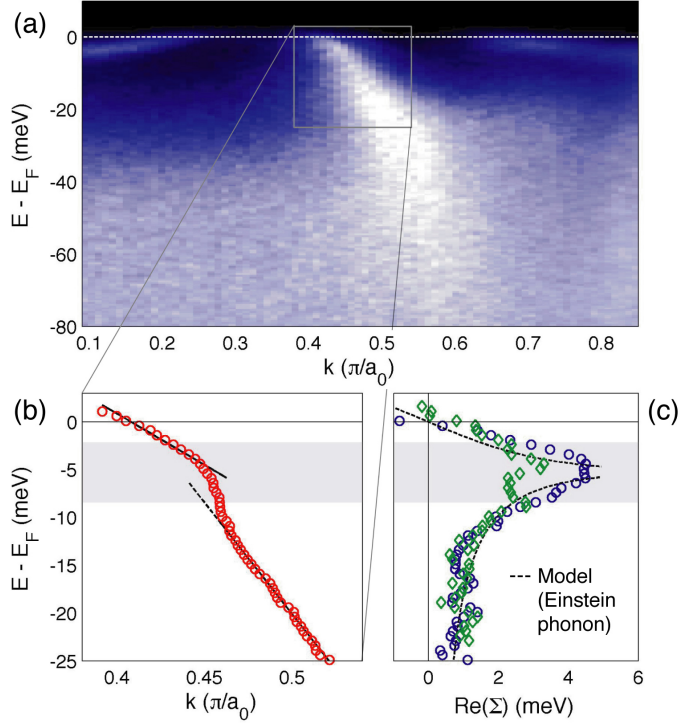


Figure 4.8: Low-energy kink in the dispersion of the α_1 band. (a), Dispersion plot along IX. The energy scale of the kink coincides with the characteristic energy scale below which we find highly renormalized quasiparticles. (b), Dispersion extracted from fits to momentum distribution curves and (c), the corresponding real part of the self energy for two different samples. The strength and shape of the kink is found to depend highly on the quality of individual cleaves but its energy of ~ 5 meV is reproducible. The dotted line shows a model of the coupling to an Einstein phonon [77].

4.2.4 Orbital character and renormalization

The orbital character of the different bands was briefly discussed in section 4. From tight-binding models, one can deduce that most straight sections on the Fermi surface that make up the α_1 , α_2 , and part of the other bands stem from the one dimensional $d_{xz,yz}$ orbitals, and the rest mainly from the d_{xy} orbital.

LDA calculations provide a more quantitative estimate of the distribution of orbital character on the various Fermi sheets. Fig. 4.10A shows the LDA - Fermi surface in the first Brillouin zone with the different orbital contributions of the $d_{xz,yz}$, d_{xy} , $d_{x^2-y^2}$ orbitals (the innermost δ band only has significant $d_{x^2-y^2}$ (e_{2g}) contribution) colored in blue, red and yellow, respec-

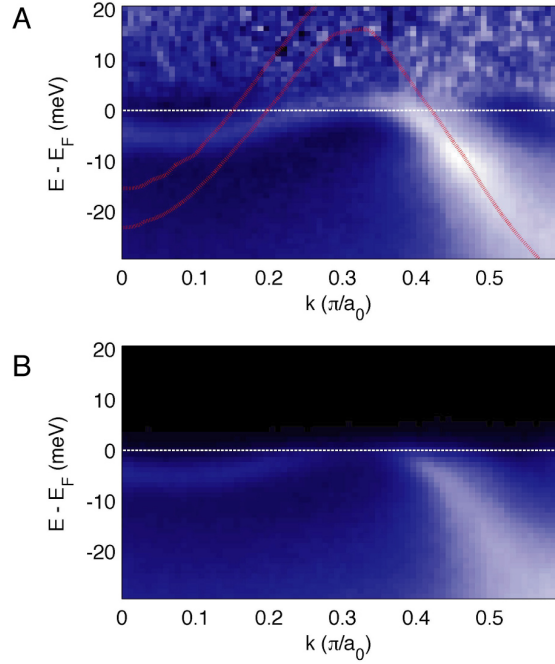


Figure 4.9: Hybridization of the δ and α_1 bands. (A), ARPES photocurrent intensities, divided by a Fermi-Dirac function to make data around and above E_{Fermi} visible. The δ and α_1 bands connect, in agreement with LDA+SO calculations (red line). (B), Raw data.

tively.

Labeling different sheets of the Fermi surface depending on their orbital character gives information about the spatial location that the electrons have. One can follow this route further by investigating how much of the contributions stem from which oxygen atom in the unit cell. We divide the atoms in three types, as defined in Fig. 4.10B: the ones in RuO layers (IL), the ones between the RuO layer within a bilayer (BL, red arrow), or on top/bottom of a bilayer (TB, blue arrows). Then, we analyze the contribution of these types to the different bands. The most striking observation is visible for the α_1 (bonding) and α_2 (anti-bonding) bands; while the former mainly stems from O p from IL oxygens, the latter stems from orbitals from BL atoms, in accordance with our naive picture of bonding and anti-bonding states. This is particularly intriguing since those bands also exhibit a very different renormalization.

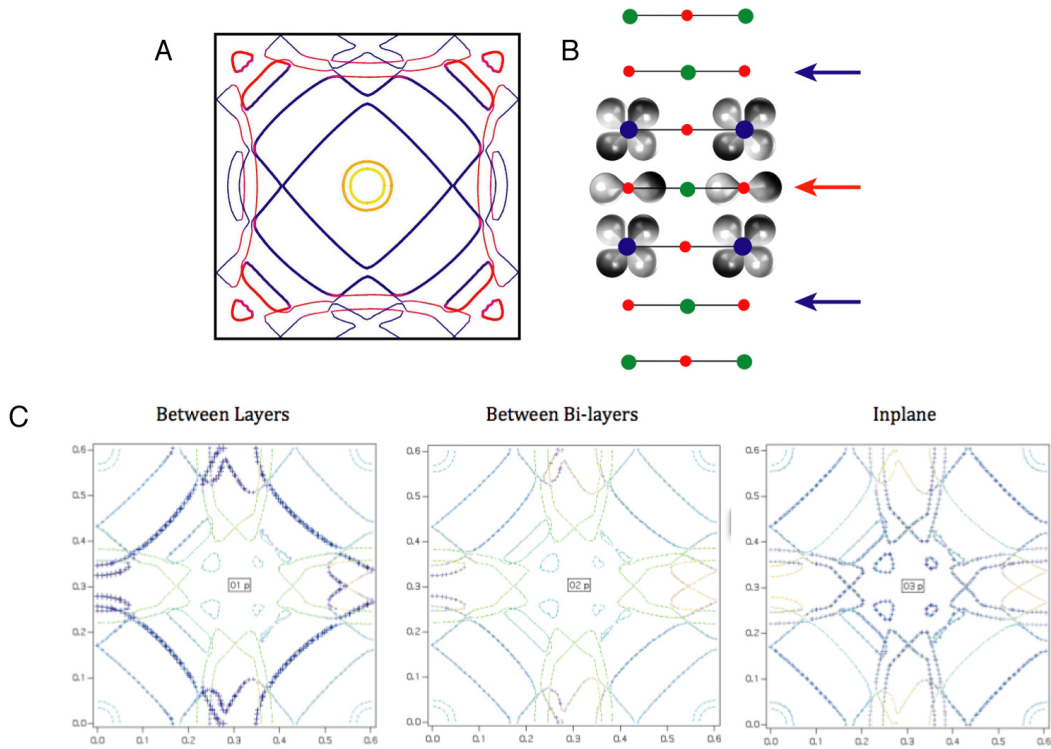


Figure 4.10: Orbital character of the different Fermi sheets. (A), Fermi surface in the first Brillouin zone calculated by LDA+SO with the different orbital contributions of the $d_{xz,yz}$, d_{xy} , $d_{x^2-y^2}$ orbitals colored in blue, red and yellow, respectively. (B), Schematic illustration of a bilayer of $\text{Sr}_3\text{Ru}_2\text{O}_7$, with Ru, O, and Sr atoms in blue, red, and green, respectively. The blue arrow indicate the oxygen atoms outside of the bilayer that contribute much to the anti-bonding α_1 , while the red arrow points to the oxygen atoms within a bilayer that contribute much to the bonding α_2 band. (C), LDA+SO Fermi surfaces with the different bands drawn with different thickness, proportional to which oxygen layer gives most contribution ('Between Layers', 'Between Bi-layers' and 'Inplane', refer to BL, TB, and IL in our nomenclature, respectively; *panel reproduced from Ref. [74]*). LDA+SO calculations by E. Rozbicki [74].

4.3 Van Hove singularities and density of states

In two dimensions, van Hove singularities arise at saddle points of the band-structure that lead to logarithmic divergences in the density of states. Van Hove singularities play an important role in many theoretical models of the metamagnetism, the criticality, and the nematicity in $\text{Sr}_3\text{Ru}_2\text{O}_7$, and ARPES

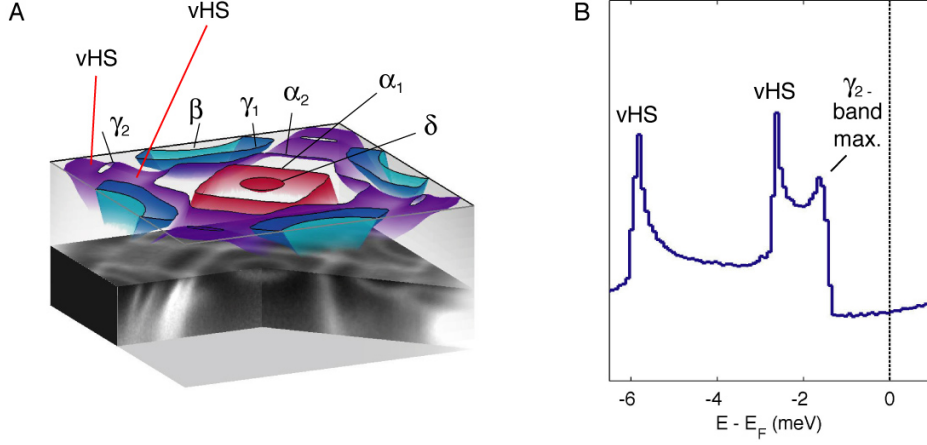


Figure 4.11: Van Hove singularities and density of states. (A), Sketch of the parametrized bandstructure. Two saddle points that correspond to van Hove singularities are visible. (B), Density of states obtained from the histogram of the band-parameterization (for details, see text).

is potentially an ideal technique to detect such band structure features.

In the low-energy bandstructure as plotted in Fig. 4.11A, two van Hove singularities are apparent. In the ΓX cut (Fig. 4.5(a)) they are visible as local band minima at around -2 and -6 meV, respectively.² To confirm that they are indeed saddle points, we took cuts in orthogonal directions (not shown), and indeed, these show band-maxima.

The low energy density of states in $\text{Sr}_3\text{Ru}_2\text{O}_7$ is not only dominated by van Hove singularities, but also by a wealth of flat bands with blunt maxima that strongly influence the density of states. We thus need not only to find the position of the van Hove singularities, but also obtain the full density of states from our data. It is not possible to just \mathbf{k} -integrate the spectral weight measured by ARPES to obtain this, since this would be strongly influenced by the matrix elements. To avoid this, we obtained the peaks of the relevant bands in numerous cuts and fitted a surface for each band through the points, shown in Fig. 4.11. Since $DOS(\varepsilon) = \int d\mathbf{k} \delta(\varepsilon - \varepsilon(\mathbf{k}))$, the ε -histogram of the parametrized bands is equal to the density of states. The result is displayed in Fig. 4.11B. Two maxima correspond to the van Hove singularities. Another maxima corresponds to the flattened maxima of the γ_2 band.

The maxima we report in the density of states are at an energy scale that

²As noted in section 4.1, ARPES can only determine the position of the singularities and the γ_2 maxima up to an uncertainty of ± 1 meV.

corresponds to magnetic field strengths that govern the metamagnetism in $\text{Sr}_3\text{Ru}_2\text{O}_7$. It is thus not inconsistent with many theoretical approaches (c.f. section 3.4). Further, the density-of-states again highlights the energy scale of ~ 5 meV at which much of the spectral weight is confined.

4.4 Concluding remarks

Detailed comparison with de-Haas-van-Alphen data

To compare ARPES data with dHvA data [47, 68, 69, 70], we calculated the cyclotron masses $m^* = \frac{\hbar^2}{2\pi} \cdot (\partial A / \partial \varepsilon)_{k_F}$ by averaging the Fermi velocities along the contours of the Fermi sheets. Note that due to the anisotropy of the sheets, the masses one gets are not as high as one might expect given the renormalization factors along ΓX .

Table 4.1 compares ARPES data with dHvA. The areas as well as the masses are equal within experimental error, showing that the ARPES data is bulk representative. The γ_2 band is not seen in dHvA, but this is most likely due to the small area.

	$\alpha_1 (h^+)$	$\alpha_2 (h^+)$	$\gamma_1 (e^-)$	$\beta (e^-)$	$\gamma_2 (h^+)$	$\delta (e^-)$
ARPES A_{FS} (% BZ)	14.1±2	31.5±3	8.0±2	2.6±1	< 1	2.1±1
ARPES m^* (m_e)	8.6±3	18±8	9.6±3	4.3±2	10 ± 4	8.6±3
dHvA A_{FS} (% BZ)	13.2±1.0	32.1±1.1	7.0±0.9	1.1±0.2		3.2±0.3
dHvA m^* (m_e)	6.8±0.5	10.4±1	8±0.5	6±3		8.5±1.0

Table 4.1: Fermi surface volumes and cyclotron masses of $Sr_3Ru_2O_7$ obtained from ARPES and dHvA. The polarity of the pockets is indicated in brackets. Errors are estimated from the statistical accuracy of the analysis and the reproducibility of the experiments. The mass of γ_3 is estimated from parabolic fits to the dispersion. *Table reproduced from Ref. [65].*

Magnetic Fluctuations

Here, we want to elaborate on the possibility of strong antiferromagnetic fluctuations being responsible for observed heavy bands and the kink. Inelastic neutron scattering at energies $\lesssim 5$ meV observed strong antiferromagnetic fluctuations in ΓX direction, at wave vectors of $|\mathbf{q}_1| = 0.18 \frac{\pi}{a_t}$ and $|\mathbf{q}_2| = 0.5 \frac{\pi}{a_t}$, where a_t is the shortest Ru-Ru distance [81, 82, 83]. These \mathbf{q} vectors connect parallel lines of various ARPES Fermi surface sheets stemming from the quasi one-dimensional $d_{xz,yz}$ orbitals. Clearly, various nesting vectors agree very well with the inelastic neutron scattering peak positions, such as $q_{\delta-\delta} = 0.18 \frac{\pi}{a_t}$, $q_{\alpha_1-\alpha_1} = 0.45 \frac{\pi}{a_t}$, $q_{\alpha_1-\alpha_2} = 0.15 \frac{\pi}{a_t}$. We thus believe that the antiferromagnetic fluctuations and the nesting vectors are intimately related, but it remains open whether those fluctuations are a mere consequence of the particular bandstructure, or if they are connected to the physics of criticality and nematicity in $Sr_3Ru_2O_7$.

Similarities with heavy fermion materials

We would now like to briefly compare the heavy quasiparticles in $\text{Sr}_3\text{Ru}_2\text{O}_7$ to these in the so called ‘heavy Fermion’ compounds associated with Kondo lattice physics. The possibility of a connection between Kondo physics and (La-doped) $\text{Sr}_3\text{Ru}_2\text{O}_7$ has been mentioned by Ref. [84]. This is intriguing, given the high Sommerfeld coefficient, the Curie-Weiss dependence of the magnetization at high temperature [56], the tendency for similar compounds to form localized spins [85], and the kink in the resistivity at 40 K [84], all of which are characteristics of Kondo-type f -electron heavy Fermion systems. This comparison can now be extended further by noting that the coexistence of heavy and ‘light’ electrons are also expected in Kondo physics, and that our results are very similar to a recent ARPES study on the heavy Fermion compound URu_2Si_2 [86]. According to the same ARPES study, a band mass ($\sim 22 m_e$) similar to $\text{Sr}_3\text{Ru}_2\text{O}_7$ was measured. We want to note here, however, that the heavy bands in the compound studied here do not ‘naturally’ originate from localized electrons, such as the f -electrons in URu_2Si_2 , and the connection to Kondo-type physics is thus, if present, not simple.

We hope that further, possibly temperature dependent, ARPES and other studies on $\text{Sr}_3\text{Ru}_2\text{O}_7$ will bring some light to this issue.

Chapter 5

Real-space orbital imaging of (Sr_{0.99}Ti_{0.01})₃Ru₂O₇

¹In this chapter, we will discuss SI-STM real space orbital imaging of (Sr_{0.99}Ti_{0.01})₃Ru₂O₇². Fig. 5.1A shows a 36×36 nm² FOV topographic image of the cleaved surface, in agreement with previous studies [48]. The strontium atoms are individually resolved and visible as small bright dots. Note that every other atom, marked by red circles, is brighter, due to the octahedral rotation and the resulting $\sqrt{2}$ superstructure (chapter 3). The most noticeable features are the dark and light spots scattered randomly over the surface. We identify them with Ti atoms that were intentionally inserted in the crystal. There are 170 such spots in this image, in agreement with 188 Ti atoms we would expect in a bilayer of this FOV in (Sr_{1-x}Ti_x)₃Ru₂O₇ with $x = 1\%$. Further confirmation stems from studies on samples with other doping ratios. Since SI-STM only probes the top few layers, this tells us that we cleave between two bilayers, otherwise, since the next Ru layer were $>10 \text{ \AA}$ away, one would only see half the dopants. When comparing with SI-STM studies on single layer Sr₂RuO₄ [87], one notes that the dark signatures visible on the Sr₃Ru₂O₇ surface are very similar to what has been identified as Ti dopants in Sr₂RuO₄. Therefore the dark signatures stem from upper sheet of the bilayer, and the white spots stem from lower sheet of the bilayer.

Careful examination of the white spots reveal that they occur in two different orientations (Fig. 5.1C,D). Each orientation occurs on one of the two disjoint sub-lattices and can be attributed to one of the different orientations

¹We published some of the results discussed here in Ref. [27]. Parts of this chapter follow closely the published manuscript.

²In order to be able to perform simultaneous **k**-space measurements (chapter 6), we used samples with 1% of the Ru atoms replaced with titanium, (Sr_{0.99}Ti_{0.01})₃Ru₂O₇. This changes the transport properties only slightly, refer to Ref. [49] for a discussion.

of the RuO_6 octahedra.

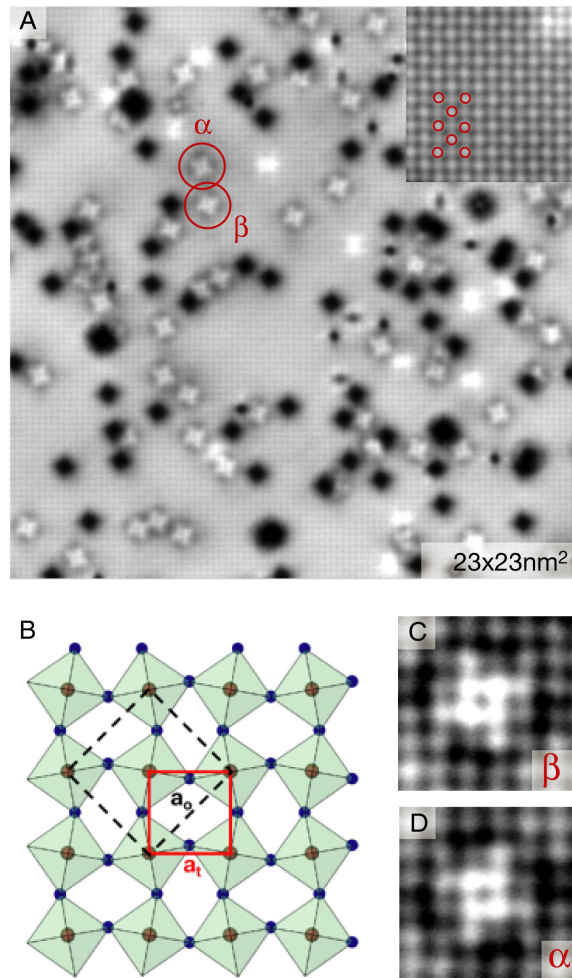


Figure 5.1: (A) Topographic image of the $\text{Sr}_3\text{Ru}_2\text{O}_7$ surface, taken at $V_B = -100$ meV and 10 G Ω . Ti dopants substituting Ru in the top and bottom sheet of the surface-bilayer are visible as black and white spots, respectively. (B), schematic view of the top layer (*panel reproduced from Ref. [65]*). The RuO_6 octahedra are alternatively rotated by $\pm 6.8^\circ$. This leads to an orthorhombic symmetry and doubles the unit cell (orthorhombic: dashed, tetragonal: orange). (C,D), Detail of the white Ti-dopant site. Two different orientations of octahedra are visible, corresponding to the two rotations of the RuO_6 , marked by α and β .

This kind of atomically flat surface is well suited for SI-STM studies. And while the shown topographs display signatures with atomic resolution, surprisingly, the simultaneously taken low junction resistance conductance

images show subatomic features.

Fig. 5.2A shows such a $g(\mathbf{r}, E)$ image with $E_B = -13$ meV, taken at unusually low junction resistance, $R_{JR} = 300$ M Ω , and far away from the nearest Ti impurity. At these resistances, weak subatomic features become visible. To increase S/N, we ‘unit-cell-average’ this and all other $g(\mathbf{r}, E)$ images; a procedure that we will describe in the next paragraph.

The $\text{Sr}_3\text{Ru}_2\text{O}_7$ surface forms a square Bravais lattice, i.e. every point (x_i, y_i) is equivalent to any other point $(x_j, y_j) = (x_i + n\sqrt{2}a_0, y_i + m\sqrt{2}a_0)$ where n, m are integers, a_0 is the shortest inter Ru distance and the $\sqrt{2}$ factor accounts for in-plane superstructure induced by the rotations of the RuO_6 octahedra. Given our ability to image large, flat areas of the $\text{Sr}_3\text{Ru}_2\text{O}_7$ surface, we can use the translational invariance to increase the S/N ratio by averaging over many of these Bravais lattice sites. First, we have to pinpoint the center of each unit cell (some marked in red in Fig. 5.2). For this purpose, we use the simultaneously taken topographic image, where Sr atoms appear as peaks. We determine the position of each Sr atom with an accuracy of less than 0.2 Å by fitting topographic peaks to a two dimensional Gaussian function. This way, we can precisely locate the position of every unit cell of the Ru-Ru lattice. To include the $\sqrt{2}$ superstructure of the lattice, we only use every other Ru atom. Second, we crop a $\sim 15 \times 15$ Å² window around every unit cell center (some marked as red boxes). We now have a set of maps which are $\sim 15 \times 15$ Å² in size, centered about a crystallographically equivalent site. Finally, we add all the equivalent points in these maps together, and divide the resulting sum by the number of maps, to arrive at an unit-cell averaged map with enhanced S/N. The sub-atomic resolution maps presented in Fig. 5.2B and Fig. 5.3 are the result of averaging over 28 such unit cells.

These maps show clear subatomic features. Since $g(\mathbf{r}, E) \sim \text{LDOS}(\mathbf{r}, E)$, this means that electrons retain local probability densities that change on a subatomic scale, and they do so in accordance with the symmetry of the relevant $d_{xy}, d_{xz,yz}$ orbitals, as shown in Fig. 5.3. Such orbital-imaging by STM has thus far only been reported in cuprates, where non-dispersive, Cu-Cu bond-centered, locally C_2 pattern have been observed [12]. In $\text{Sr}_3\text{Ru}_2\text{O}_7$, the pattern are locally C_4 and change quickly with energy, perhaps due to the strong renormalization that the quasiparticle undergo in this compound (c.f. chapters 3, 4 and 6).

The interpretation of the reported pattern is non-trivial. Theoretical models of orbital ordering have been proposed [62, 63], but thus far, no explicit calculations of the signatures we measure have been made. We hope that measurements of these structures in an external magnetic field can possibly help understand them better and reveal the microscopic mechanisms associated with nematicity.

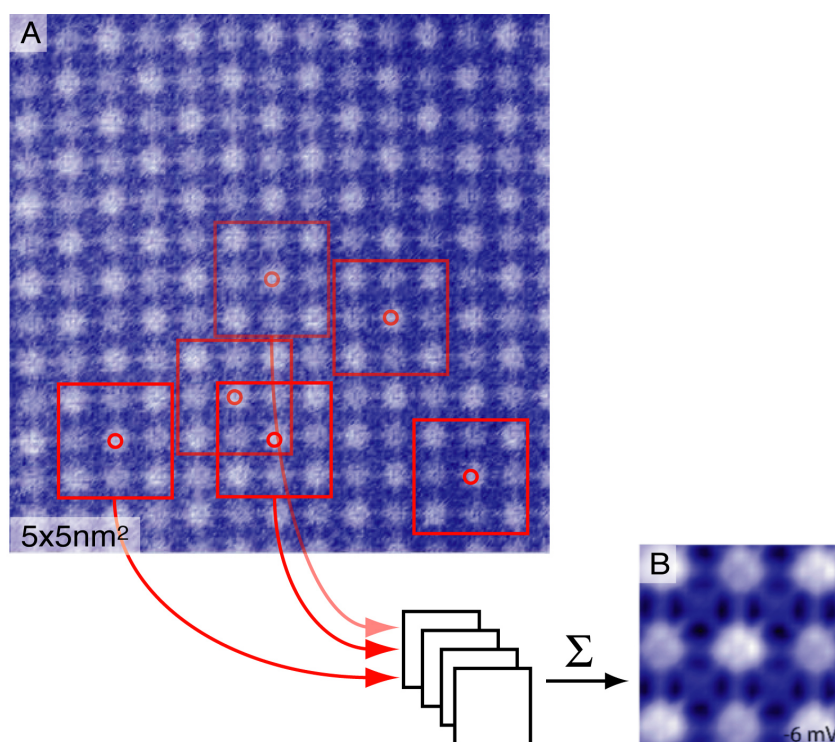


Figure 5.2: Schematic image showing the 'unit-cell-averaging' described in the text. (A), Conductance image at $E = -6 \text{ meV}$, and (B), the unit cell averaged image. The red squares in (A) show some of the cropped areas that are summed to produce the unit-cell-averaged image.

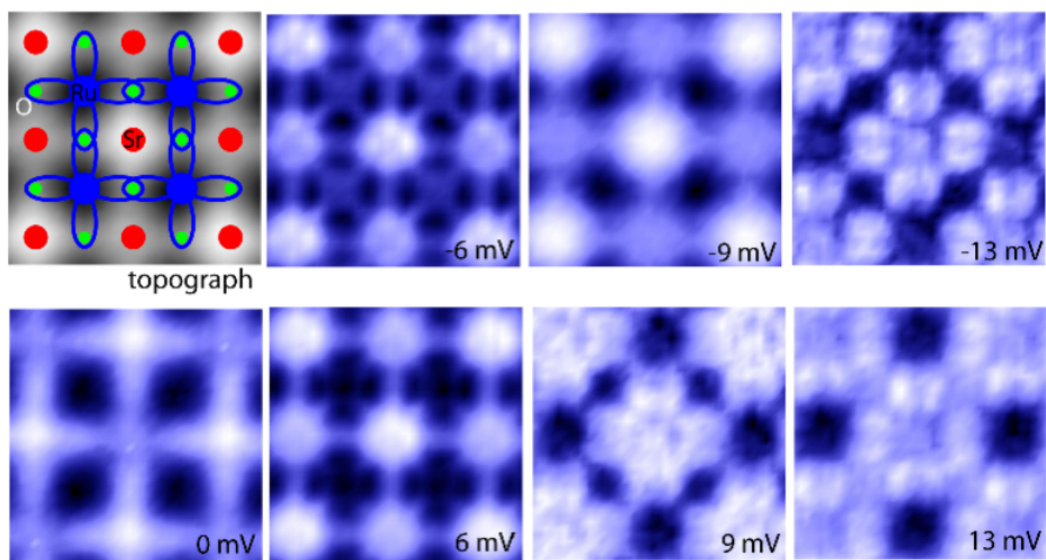


Figure 5.3: The top left-hand panel shows a topographic image with the locations of Ru atoms and their $d_{xz,yz}$ orbitals in blue. Red and green circles mark the positions of Sr, and O atoms, respectively. Each subsequent panel shows $g(\mathbf{r}, E)$ maps resolving sub-unit-cell spatial features in the same field of view. Whereas some $g(\mathbf{r}, E)$ show high intensity mainly at the positions of the Sr atoms, others clearly resolve sub-unit-cell features with the symmetry and location of the d_{xz} , d_{yz} , d_{xy} orbitals.

Chapter 6

Quasiparticle interference of the α_2 -band

¹SI-STM can image both real and reciprocal space [34, 33] — in this section we will discuss quasiparticle interference (QPI) in $\text{Sr}_3\text{Ru}_2\text{O}_7$. Note that the $g(\mathbf{r}, E)$ conductance images we show in this chapter are optimized to study the long wavelength oscillations caused by QPI, i.e. typically ~ 30 nm and ~ 256 pixel and thus obviating the visibility of any small-scale pattern discussed in chapter 5.

6.1 Fourier transform SI-STM data

So far, QPI signals have been detected either for surface states of metals, where one meets little renormalization and high density of states [23, 24], or on the superconducting gap in high-temperature superconductors, where the density of states has extremely sharp peaks at certain \mathbf{k} -space locations as a consequence of the d -wave gap [34, 33]. Both conditions are extremely favorable for QPI measurements. It was thus previously unclear if QPI experiments are possible in a strongly correlated material with such a complex bandstructure as $\text{Sr}_3\text{Ru}_2\text{O}_7$.

Fig. 6.1 shows a sequence of conductance images on $(\text{Sr}_{1-x}\text{Ti}_x)_3\text{Ru}_2\text{O}_7$. The spots identified as Ti atoms on topographic images now appear as dark or light spots, depending on the energy. More interesting though are the interference fringes that are visible around them. These patterns are rather complex and change quickly with changing energy. The Fourier transforms

¹We published some of the results discussed here in Ref. [27]. Parts of this chapter follow closely the published manuscript.

of those images, $g(\mathbf{q}, E)$, reflect this and show rapidly dispersing complex pattern in the range of -14 to -9 meV.

Unfortunately, these images (e.g. $E = -9$ meV) also reveal that the shape of the tip with which the experiment was conducted is not perfectly isotropic. This was confirmed by examining the autocorrelation of topographic images. To neutralize this effect, we 'octet-symmetrized' the data: We only took 1/4 of the image ($x > 0 \wedge x \leq y$), symmetrize it, and repeated it to the whole \mathbf{q} -space, leading to the images shown in Fig. 6.2. The analysis described in the next section uses the octet-symmetrized images.

6.2 Quasiparticle interference from the model α_2 -band

To identify the bands responsible for the observed QPI pattern, we considered the bands calculated by LDA and measured by ARPES (chapter 4). This complex bandstructure would produce an even more complex QPI pattern, consisting of many lines and peaks. Surprisingly, careful examination shows that all the peaks observed in the measured $g(\mathbf{q}, E)$ data can be explained with only one band: the cross-shaped hole pocket around Γ , named ' α_2 ' (c.f. chapter 4). To test this hypothesis, we modeled the α_2 band to best fit our QPI data.

Fig. 6.3A shows a contour of our model α_2 band compared with LDA calculations [65], B shows the simulated spectral weight $A(k, \omega = -11$ meV) stemming from it. To calculate $A(\mathbf{k}, \omega)$, we used equation 2.2, with an imaginary part of the self energy of $\Sigma_{im} \approx 3$ meV. High QPI signal is expected at \mathbf{q} vectors that connect points of high $A(\mathbf{k}, \omega = const)$ regions. A measure thereof is the joint-density of states $JDOS(\mathbf{q}, E)$ that is calculated by taking the \mathbf{k} -autocorrelation of the $A(\mathbf{k}, \omega)$ images, more information about this procedure can be found in Refs. [88, 89]. 10 maxima can be extracted from the $JDOS(\mathbf{q}, E)$ displayed in Fig. 6.3C, they are marked by colored vectors $\mathbf{q}_{1...10}$. The same vectors are also overlaid on the simulated $A(\mathbf{k}, \omega)$ images, where they connect regions with high value. When comparing the 10 vectors with the maxima in the real $g(\mathbf{q}, E)$ data in Fig. 6.3D, one can see that those 10 vectors account for all dispersing maxima.

To test the hypothesis that the α_2 band is indeed responsible for the measured QPI pattern, we followed the dispersion of the QPI and the simulated $JDOS(\mathbf{q}, E)$, and indeed they agree over an energy range of -13 to -7 meV. This shows that the QPI data can be self-consistently explained using scattering from the α_2 band only.

This poses the question as to why one band dominates the QPI signal. Could it be that other bands produce maxima at similar locations, making it impossible to differentiate their signal? Or could it be that other bands produce such low $JDOS(\mathbf{q}, E)$ that their contribution is negligible? We determined this through simulations. We calculated the response that one would expect for the different bands observed by ARPES. Based on this, the answer is that we can exclude significant contributions from all other bands except perhaps for the α_1 band. All other bands would produce peaks that were clearly visible, but the α_1 band produces peaks at similar \mathbf{k} -space locations than the α_2 band.

Consequently, there must be other reasons why the α_2 band dominates the scattering process. One possible explanation is that the Ti atoms only couple to this band, and thus selectively produce QPI scattering signal from it. Likely an influence has also the different spacial locations of the electrons in the different bands (c.f. section 4.2.4). It is natural to assume that electrons located closer to the tip are more likely to tunnel into it and consequently they produce a stronger signal. Since the α_2 band has far more weight at the apical oxygens on top of the bilayer than the other bands, it would also give a stronger signal, in agreement with our data.

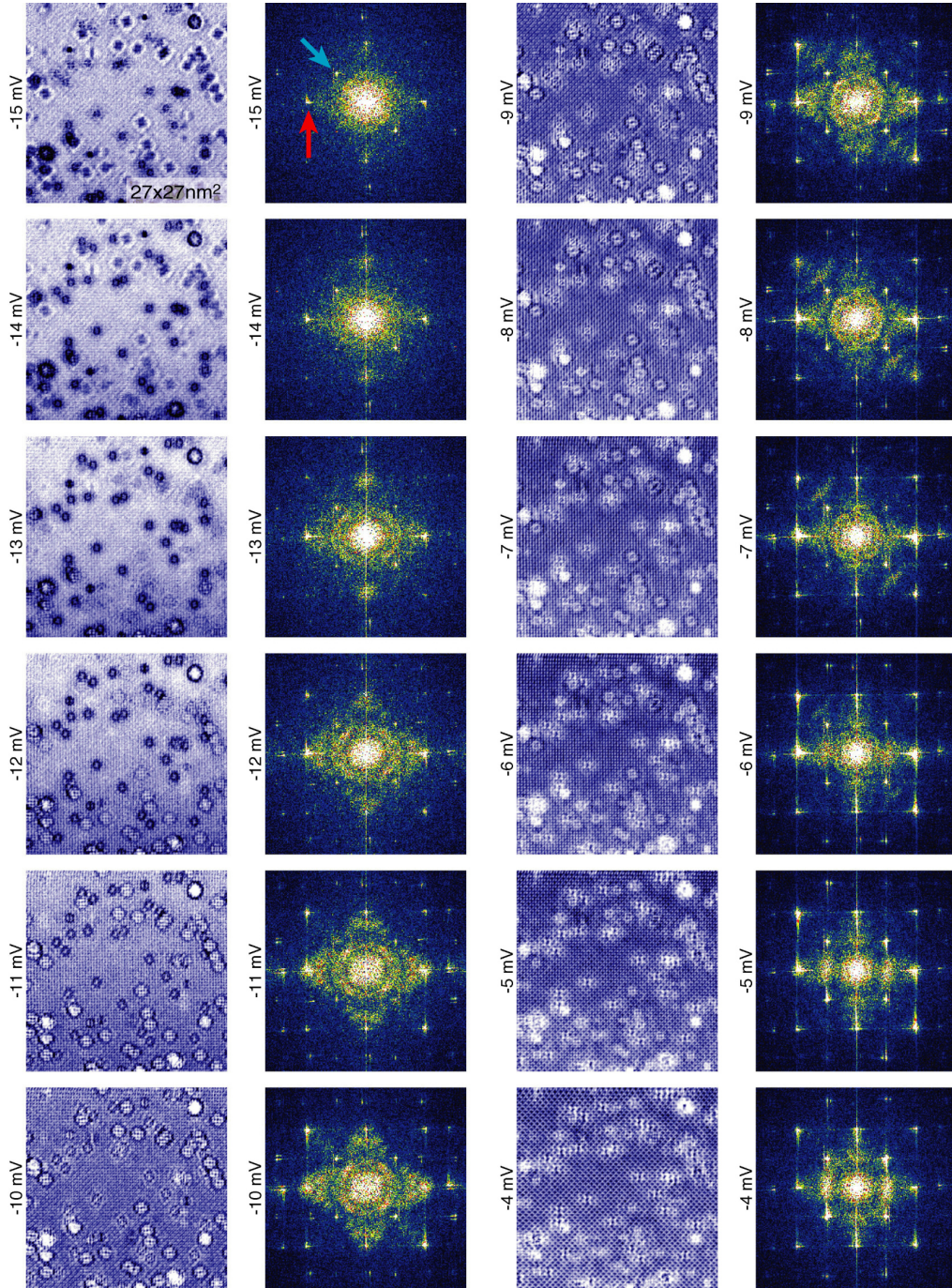


Figure 6.1: *Left column*, A sequence of $g(\mathbf{r}, E)$ images taken in a $27 \times 27 \text{ nm}^2$ FOV. The dark or light features (depending on E_B) are Ti-dopants substituting Ru. Interference fringes can be seen around them. *Right column*, The corresponding Fourier transforms. The bright spots (red arrow in top panel) stem from the Sr lattice. Clearly visible are also the $\sqrt{2}$ reconstruction spots (blue arrow). Dispersing QPI patterns are visible, especially in the energy range -14 meV to -9 meV . In the following, we will concentrate on this energy range.

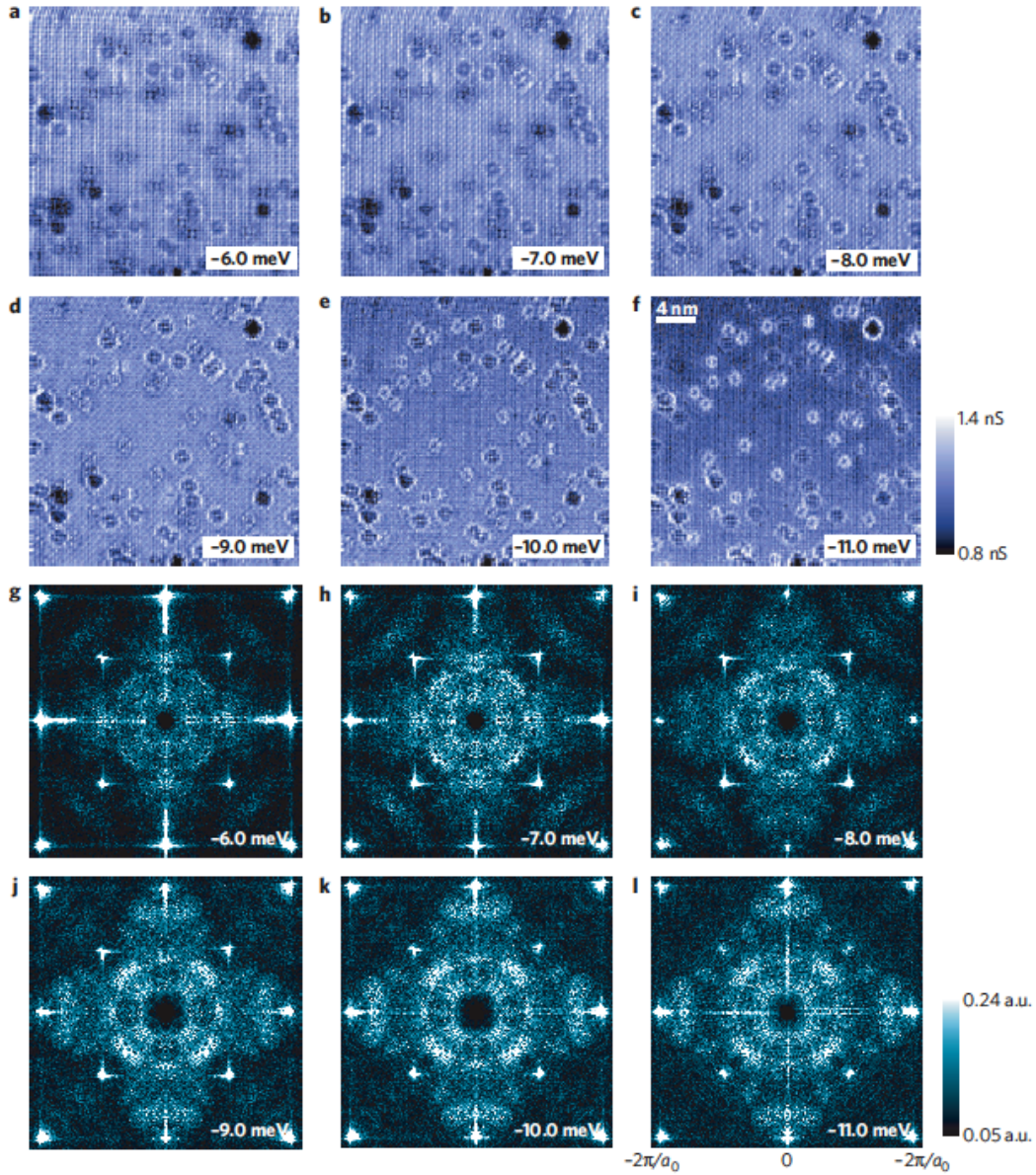


Figure 6.2: (A-F), A sequence of $g(\mathbf{r}, E)$ maps taken at +100 mV, $1\text{G}\Omega$, all taken in the same 28-nm-square FOV. Each Ti scatterer exhibits energy-dispersive QPI fringes around it. (G-L), The corresponding two-dimensional Fourier-transform image $g(\mathbf{q}, E)$, revealing heavy d -electron QPI directly. The dark area near $\mathbf{q}=(0, 0)$ is where spectral weight has been reduced to allow for clearer viewing of the $g(\mathbf{q}, E)$ contrast and the images are octet-symmetrized (original data in Fig. 6.1). A complex and fast-dispersing set of wave vectors \mathbf{q}_i is seen in these $g(\mathbf{q}, E)$. This \mathbf{q} -space complexity and dispersion can be explained by scattering between states in only one very simple band of $\text{Sr}_3\text{Ru}_2\text{O}_7$.

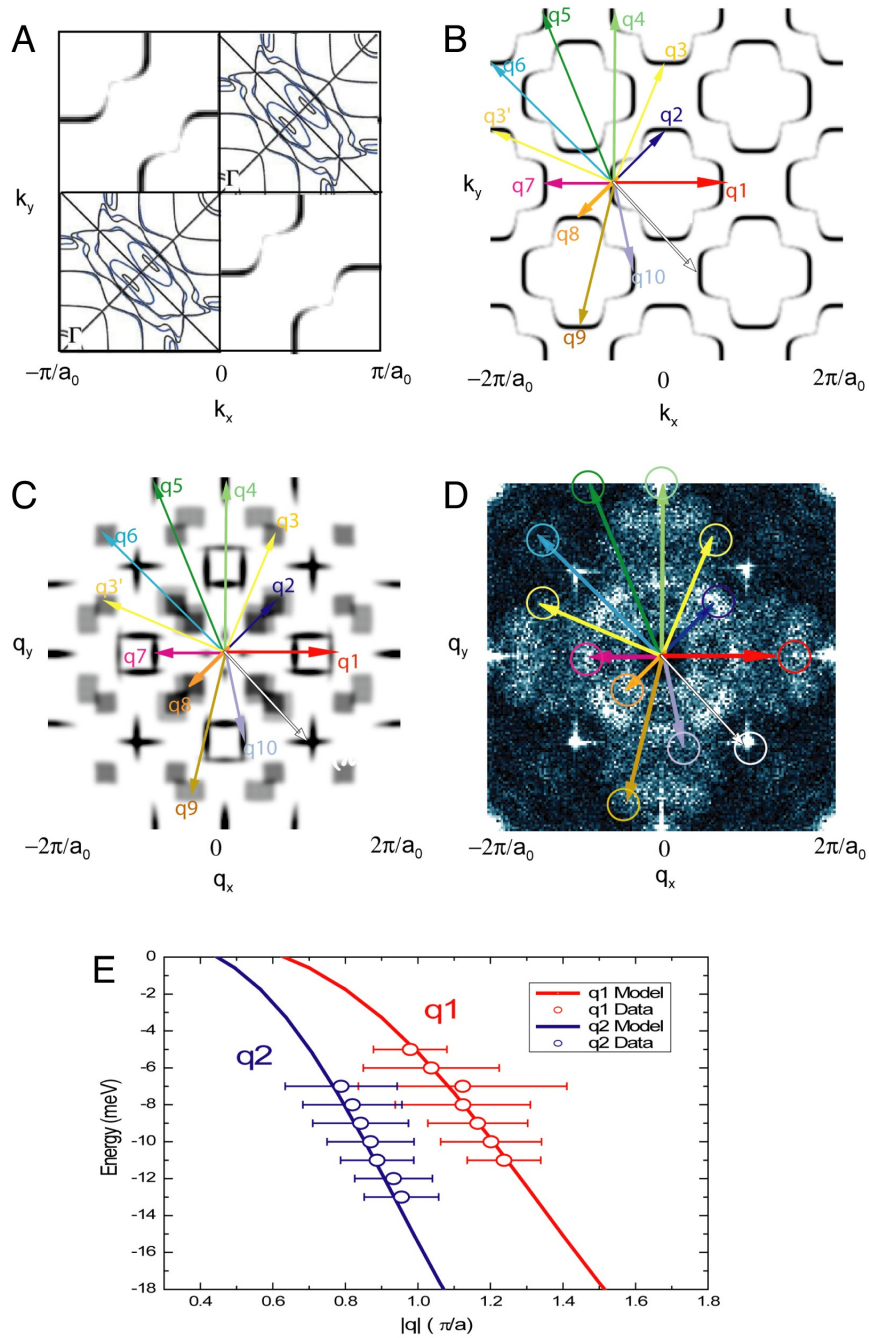


Figure 6.3: The local-density-approximation band structure in the first Brillouin zone (top right and bottom left quadrants) compared with the α_2 band of our model. (B), The model $A(\mathbf{k}, \omega)$ of the α_2 band in the extended zone scheme at $E = -9$ meV. The full set of inequivalent scattering vectors $\mathbf{q}_{i=1\dots 10}$ is shown as colored arrows (same arrows in (C,D)). (C), The autocorrelation of the model α_2 shown in (B). This process picks out the regions of high $JDOS(\mathbf{q})$, which should dominate the quasiparticle scattering process. (D), By overlaying as open circles the tip positions of these same \mathbf{q}_i on $g(\mathbf{q}, E = -9$ meV), we see that all inequivalent maxima can be accounted for by α_2 band scattering interference. (E), Measured dispersions of \mathbf{q}_1 and \mathbf{q}_2 from data in Fig. 6.2(G-L). They agree well with the model α_2 band (solid line). The error bars indicate the standard deviation widths of \mathbf{q}_1 and \mathbf{q}_2 peaks along the dispersion lines after fitting them to Gaussian curves at each energy.

6.3 Agreement between the model α_2 band and ARPES

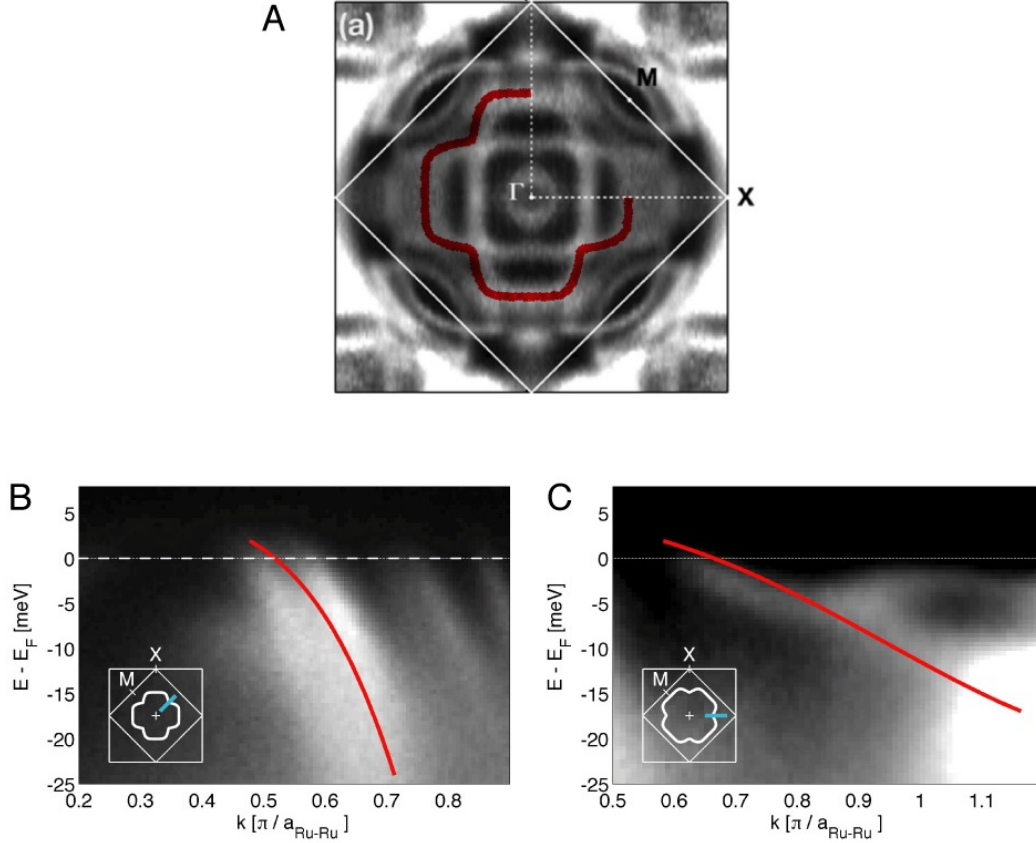


Figure 6.4: Agreement between the model α_2 band and photoemission data. (A) Comparison of Fermi surface (*panel reproduced from Ref. [65]*). The red contour marks the model α_2 Fermi surface. (B, C) Comparison of band dispersion along ΓM and ΓX , respectively. The red line from the model α_2 band follows regions of high photocurrent intensity.

The α_2 band topology described in this paper has been constructed primarily to model the QPI data. To this end, we started from two strongly unidirectional bands $E_x(\mathbf{k})$, $E_y(\mathbf{k})$ described by the empirical formula

$$E_{x,(y)}(\mathbf{k}) = \{1222 \sin^6(k_{x,(y)}a_0/2) - 26.4 \sin^4(k_{y,(x)}a_0/2) + 1.37\} \text{ meV},$$

where a_0 is the Ru-Ru nearest neighbor distance. $E_x(\mathbf{k})$, and $E_y(\mathbf{k})$ corresponds to the bands of ruthenium d_{xz} , and d_{yz} orbital character respectively.

The α_2 band is then obtained by hybridizing these hypothetical bands:

$$E_{\alpha_2}(\mathbf{k}) = \frac{E_x(\mathbf{k}) - E_y(\mathbf{k})}{2} - \sqrt{(E_x(\mathbf{k}) - E_y(\mathbf{k}))^2 + V^2},$$

with $V = 2$ meV. In Fig. 6.4, the model Fermi surface is overlaid on the experimental ARPES data. Its size and shape closely resemble the cross-shaped experimental Fermi surface contour of α_2 band derived from the out of plane d_{xz} , d_{yz} orbitals [65]. The best agreement is observed after shifting the model band by 3 meV towards higher energies. This shift is probably due to small energy uncertainty as well as momentum uncertainty of both techniques, not due to possible different doping level since Ti impurities are not charged. The agreement between the model and ARPES extends to other energies: the dispersion plot along ΓM (Fig. 6.4) shows that the model α_2 band has the same Fermi velocity as the corresponding band measured by ARPES. Hence our QPI result is in very good agreement with the band structure measured by ARPES over the entire energy range investigated in this paper.

Chapter 7

The ferropnictides: a second family of high-temperature superconductors

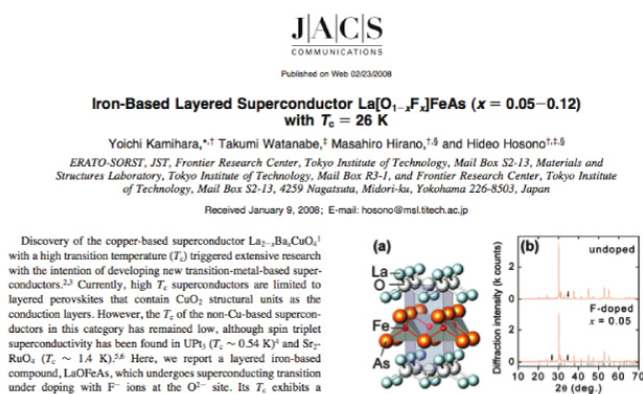
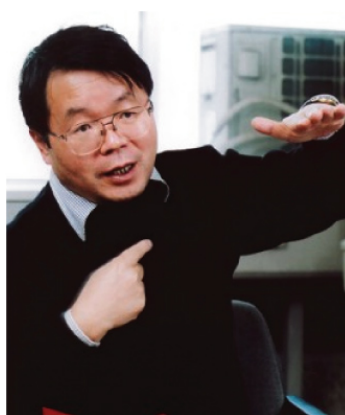


Figure 7.1: Hideo Hosono from the Tokyo Institute of Technology, and excerpt of the paper announcing superconductivity in $\text{F}_x\text{La}_{1-x}\text{OFeAs}$ [90]

In February 2008, Hideo Hosono (Fig. 7.1) and his group from the Tokyo Institute of Technology published an article about superconductivity below $T_c = 26$ K in an electron doped, layered iron arsenide material, $\text{F}_x\text{La}_{1-x}\text{OFeAs}$ [90]. This discovery led to great excitement, for a number of reasons:

- The material contains iron, an element that is not known to be superconducting and was, due to its ferromagnetism, assumed to be unfavorable to it [5].

- The atomic structure and the phase diagram have similarities with the cuprates, a class of materials that have at least touched the careers of most condensed matter physicists, and that still spark their interest and curiosity. The new materials show striking similarities with the cuprates, yet are different enough to be classified as a ‘second family’ [91, 92].
- More than 20 years after the discovery of the high-temperature superconducting cuprates [93], there is still no consensus about the microscopic mechanisms leading to superconductivity, and technical applications, albeit present, are more challenging than perhaps expected [94]. The discovery of a second family of high-temperature superconductors brings hope to both these areas.

In this chapter, we will first introduce the atomic structure of the different families of ‘ferropnictides’, as the new family was termed, and then give an overview of the magnetic and electronic structure. This is not intended to be a complete review, but rather a short introduction to this fast changing subject. Most of the time, we will use CaFe_2As_2 , the compound we performed SI-STM experiments on, as an example. Later, we will quickly summarize the results of STM experiments on ferropnictides thus far.

7.1 The different families

Most ferropnictides are commonly divided into four families with structural similarities, called ‘1111’, ‘111’, ‘11’ and ‘122’, loosely referring to the number of different atoms in the unit cell. Fig. 7.2 depicts the generic structure of each family that will be introduced here briefly.

The ‘1111’ family (e.g. LaFeAsO)

The first discovered ferropnictide was $\text{F}_x\text{La}_{1-x}\text{OFeAs}$ [90]. More generally, the 1111 family consists of compounds of the form $R\text{FeAsO}$, $R = \text{Ce}, \text{Pr}, \text{Sm}, \text{Nd}$, etc. These consist of two dimensional FeAs layers, with structurally similar RO layers in between (Fig. 7.2A). The parent compound is metallic and has a tetragonal to orthorhombic and a paramagnetic to antiferromagnetic transition that occur around 100 K and 150 K, respectively [90].¹ Superconductivity is induced by electron doping² the parent compound, such as by replacing oxygen with fluorine, or by inducing oxygen deficiency [96].

¹Newer work suggests that this difference is very dependent on sample quality [95].

²Recent experiments suggest that the doping in the ferropnictides is qualitatively different than in the naive picture with the introduced atoms inducing additional charge

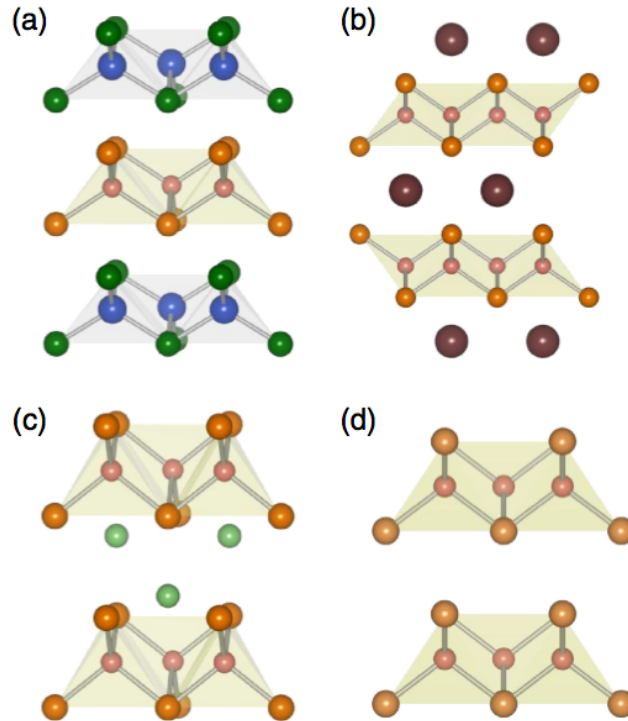


Figure 7.2: Schematic structure of the different ferropnictide families introduced in the text, (a) 1111, (b) 122, (c), 111, (d), 11. *Figure reproduced from Ref. [91].*

The ‘122’ family (e.g. CaFe_2As_2)

The 122 family consist of materials of the form $R\text{Fe}_2\text{As}_2$, with the so called ThCr_2Si_2 -structure (Fig. 7.2B). It has an FeAs layer like the 1111 compounds, but with R layers in between. The valence of the FeAs layer is $1-/\text{Fe}$ (as it is in the 1111 compounds), and thus charge neutral cleaving between the layers is impossible. To make it superconducting, $R\text{Fe}_2\text{As}_2$ can be hole doped through substitution of R^{2+} with A^+ (e.g. K for Ba, Na for Ca [97, 98]), or electron doped by replacing Fe with Co (e.g. $\text{Ca}(\text{Fe}_{1-x}\text{Co}_x\text{As})_2$ [99]). The parent state of 122 compounds has a tetragonal to orthorhombic and paramagnetic to antiferromagnetic transition that occur simultaneous around

carriers. Theoretical models as well as the possibility to introduce superconductivity by ‘doping’ with isovalent atoms indicate that effects like chemical pressure might have an effect, and that the ‘dopants’ do in fact not induce charge carriers. Consistent with large parts of the literature, we will for now continue to use the word ‘dopant’ to describe intentionally introduced atoms to alter the electronic structure.

130 to 220 K [100].

The ‘111’ family (e.g. LiFeAs)

The 111 compounds are possibly the least studied ones. These $R\text{FeAs}$ compounds have the Cu_2Sb type crystal structure (Fig. 7.2C), with $R = \text{Li}, \text{Na}$, e.g. [101]. Superconductivity in LiFeAs can be up to 18 K with Li deficiency [101] or up to 33 K in $\text{NaFeAs}_{0.8}\text{P}_{0.2}$ [102].

The ‘11’ family (e.g. FeSe)

The 11 family has the simplest structure among the ferropnictide families (Fig. 7.2D). It consists of 2d $\text{Fe}R$ layers, such as FeTe, FeSe. Technically, these compounds are not ‘pnictides’, but ‘chalcogenides’. Superconductivity can be induced by inducing R deficiency (~ 8 K in FeTe, or up to 27 K under pressure [103]) or by replacing Te with Se.

Recent multilayer systems

Recently, more complex ferropnictide structures were discovered. These include $\text{Sr}_4\text{V}_2\text{O}_6\text{Fe}_2\text{As}_2$ ($T_c = 39$ K), and $\text{Sr}_3\text{Sc}_2\text{O}_5\text{Fe}_2\text{As}_2$ [104, 105]. The former has charge neutral, mirror-symmetric cleaving planes, and is thus potentially well suited for SI-STM experiments. Unfortunately, no single crystals have been reported at the time of writing.

7.2 Ground state electronic structure

Ferropnictides are bad metals in their parent state, i.e. at zero doping. All have the same main features in their band structure (depicted in Fig. 7.4), but the details are compound specific and complicated. This is mainly due to possible opening of spin-density-wave gaps around the Fermi level, and to the back-folding due to smaller Brillouin cells with the coming of magnetic order — section 7.3 talks about this more and Fig. 7.3 is an illustration of the different real space unit cells on the top layer.

We will first concentrate on the general bandstructure characteristics that are observed in most ferropnictides of the 1111 and 122 families. The states that stem from the FeAs layer are almost solely responsible for the states around the Fermi level [107]. Fig. 7.4A shows the bandstructure in a hypothetical Fe-Fe Brillouin zone, but since the unit cell of the crystal contains two Fe atoms, the actual Brillouin zone is only half as big, and the bandstructure has to be back-folded. This gives two hole pockets around

Γ and two electron pockets around M (Fig. 7.4B). In the antiferromagnetic phase (c.f. section 7.3), the effective Brillouin zone is divided in half, leading to further back-folding. The exact way in which bands hybridize then is still under discussion, and ARPES results are not yet conclusive (e.g. Refs. [108, 109, 110, 111, 112, 113, 114]).

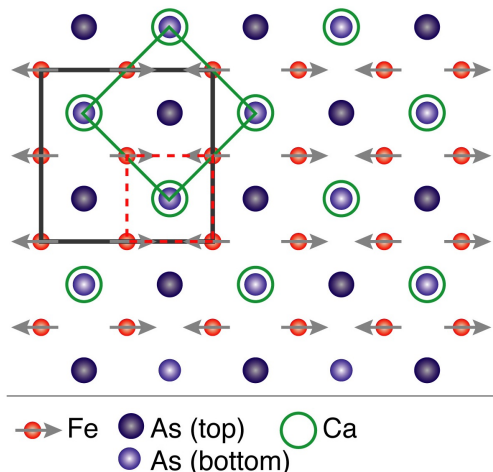


Figure 7.3: Top view of the atomic structure of CaFe_2As_2 . The FeAs layer and one adjoind Ca layer is drawn. The dotted red, green, and gray square mark the FeFe, CaCa, and antiferromagnetic unit cell, respectively.

7.3 The phase diagram

As mentioned, members of the 122 family show a structural phase transition, in the case of CaFe_2As_2 this occurs at around $T_S = 170$ K [99]. The structural transition is a change from tetragonal, $a = b$, to orthorhombic, $\frac{a-b}{a+b} \approx 1\%$ [117]. Further, there is a magnetic phase transition that occurs at the roughly the same temperature in 122 systems, or at significantly lower temperatures in 1111 systems³. The material changes from paramagnetic to a state that is ordered anti-ferromagnetically along the a -axis and ferromagnetically along the b -axis, with every other spin being the same, i.e. period $2a_{\text{FeFe}}$, a_{FeFe} being the shortest iron-iron distance. This particular order is sometimes (sloppily) called ‘spin-density-wave phase’ or ‘antiferromagnetic phase’, we will use the latter nomenclature. Fig. 7.5 is a plot of the strength of the staggered magnetic moment as a function of temperature in LaFeAsO ,

³Recent work suggests that this difference is very dependent on sample quality [95].

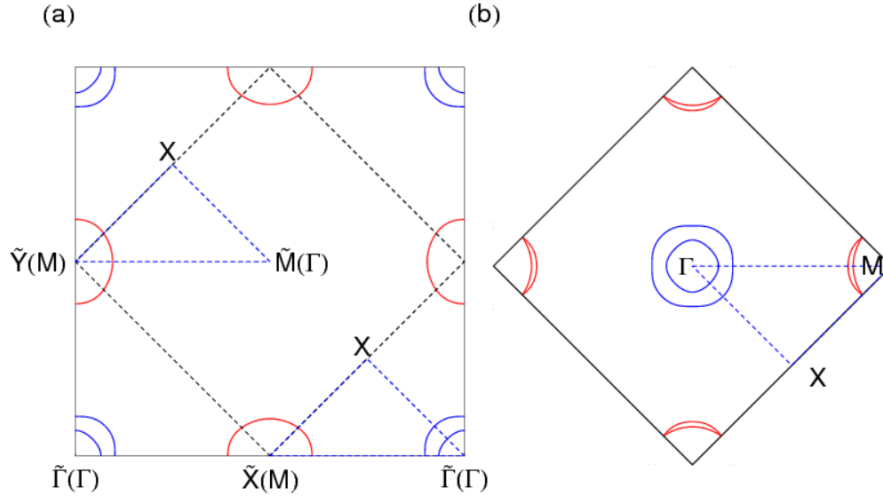


Figure 7.4: The bandstructure of CaFe_2As_2 . (a), Effective Brillouin zone for Fe-Fe tight-binding model. The dashed line indicates the Brillouin zone of the crystallographic unit cell (Fig. 7.3). (b), Back-folding of the bands lead to two hole pockets around Γ and two electron pockets around M . *Figure reproduced from Ref. [107].*

the inset is a schematic of the ordering of the spins. The phase transition reflects itself also in nuclear magnetic resonance, Mössbauer, and resistivity measurements. Upon doping, the temperature of the phase transitions is lowered until it goes towards zero ($\sim 4\%$ to 8% in BaFe_2As_2). After some threshold doping, the sample becomes superconducting; the transition temperature marks usually roughly the shape of a dome in the phase diagram. In 122 samples, the structural and magnetic transition lines hit the superconductivity dome, and there exists coexistence of superconductivity and antiferromagnetic ordering [118]. In 1111 samples, the magnetic phase transition temperature goes to zero at lower doping where no superconductivity takes place while the structural phase transition hits the superconductivity dome. Fig. 7.6 shows representative phase diagrams.

7.4 Similarities with the cuprates

The phase diagrams of the ferropnictides have clear similarities with the ones of the cuprates (and with some organic superconductors, for that matter [119]): An antiferromagnetic parent state that becomes superconducting upon carrier doping (Fig. 7.6), and an anti-ferromagnetic (or Mott insulator) phase transition line that is suppressed to zero with doping. Both are layered

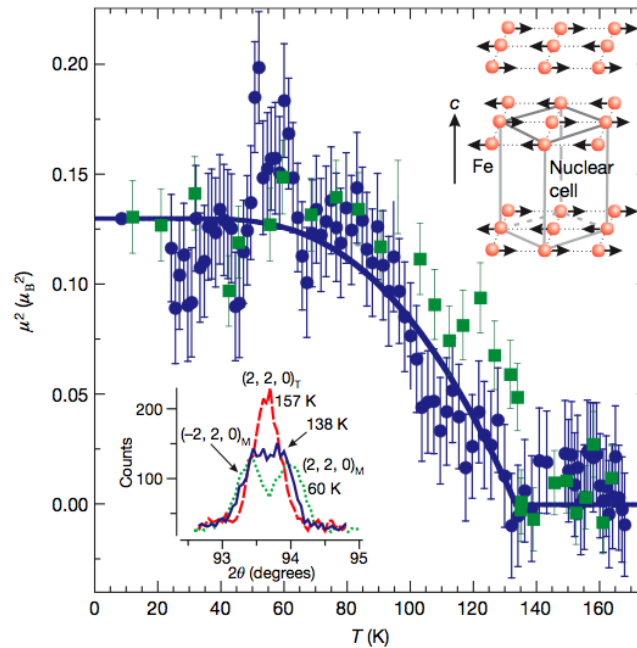


Figure 7.5: Temperature dependence of the square of the magnetic moment in $F_x\text{La}_{1-x}\text{OFeAs}$, measured by neutron scattering. The inset shows schematically how the spins are arranged in the antiferromagnetic phase. *Figure reproduced from Ref. [115].* For details, see reference.

compounds, both have to a large extent d -electron carriers. Differences include the bandstructure that is more complicated in the ferropnictides than in the cuprates, and the insulating parent state of the cuprate parent state compared to the metallic parent state in the ferropnictides. A more detailed comparison can be found in Ref. [120].

7.5 STM experiments on the ferropnictides

The first single crystals of 122 ferropnictides were grown in mid-2008, and immediately, ARPES and SI-STM experiments were performed. Unfortunately, the latter proved to be very challenging. The cleaved surfaces showed mostly disordered structures without atomic resolution, sometimes patches of atoms appeared but mostly with much scattered debris on them, rendering most classic SI-STM experiments impossible. Fig. 7.7K shows a typical topographic image of BaFe_2As_2 : no atomically flat surface is visible. Even

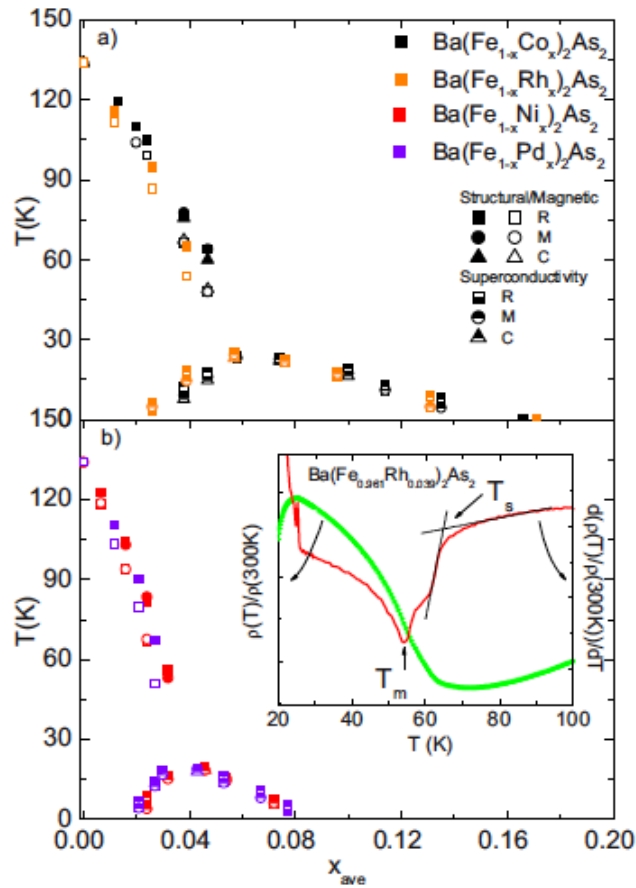


Figure 7.6: Phase diagram of various $\text{Ba}(R_x\text{Fe}_{1-x})_2\text{As}_2$ compounds with transition temperatures for antiferromagnetic, structural, and superconducting phase transition (see labels). The generic shape includes lines of structural and magnetic phase transitions that are, upon doping, suppressed towards zero temperature, and a dome of superconductivity. *Figure reproduced from Ref. [116]. For details, see reference.*

though it can be expected that cleaving is more violent in the ferropnictides than in the cuprates - due to the lack charge neutral cleaving planes and mirror planes in between layers of atoms - it is unclear why one observes these disordered surfaces. Could it be that parts of the spacer layer, such as Ba and Ca in 122 systems, stays scattered on the surface? This question is under debate (c.f. chapter 8).

We take a practical approach to this challenge and display an overview of cleaved surfaces from the literature and from our lab in Fig. 7.7. Only two materials seem to give the atomically flat, debris-free surfaces suitable for SI-

STM experiments: CaFe_2As_2 , and members of the 11 family. We concentrate on CaFe_2As_2 .

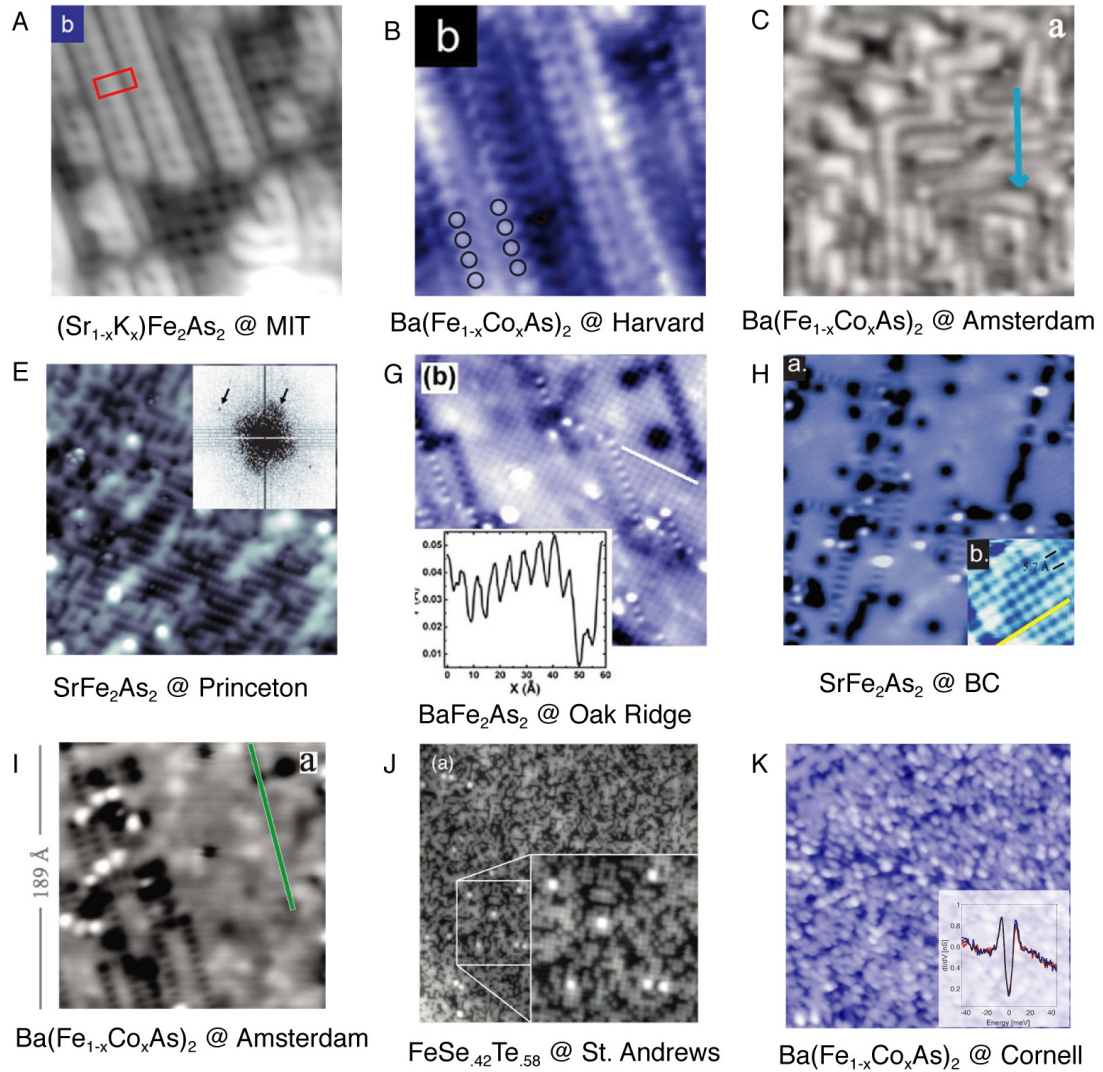


Figure 7.7: Various STM images of different ferropnictide surfaces. Most surfaces show either disordered structures or much debris on the surface (A-H,K). The $\text{FeSe}_x\text{Te}_{1-x}$ (J) and the $\text{Ca}(\text{Fe}_{1-x}\text{Co}_x\text{As})_2$ (Fig. 8.2) compounds show surfaces well suited for SI-STM. *Images reproduced from Refs. [121, 122, 123, 124, 125, 126, 123, 19], respectively.* For details, see references.

Chapter 8

SI-STM of the nematic electronic state in $\text{Ca}(\text{Fe}_{0.97}\text{Co}_{0.03}\text{As})_2$

In Fig. 8.2, one can see that cleaving $\text{Ca}(\text{Fe}_{1-x}\text{Co}_x\text{As})_2$ crystals reveals atomically flat surfaces suitable for SI-STM, thus we now concentrate our experiments on this material.

$\text{Ca}(\text{Fe}_{1-x}\text{Co}_x\text{As})_2$ is representative of the 122 family of structurally similar compounds. LDA calculations as well as ARPES measurements show Fermi surfaces in fair agreement with other 122-compounds [127, 128, 108, 109, 110, 111, 112, 113] – the details of back-folding and hybridizations are, as often in the ferropnictides, complicated and not well understood. Transport and X-ray measurements confirmed the typical 122 phase diagram qualitatively similar to BaFe_2As_2 and SrFe_2As_2 , with simultaneous magnetic and structural transitions at ~ 170 K [99, 117, 129] (Fig. 8.1). Surprisingly however, neutron scattering showed a clear difference between the coupling constants J_{1a} , J_{1b} in CaFe_2As_2 , much larger than what is expected from the miniscule lattice asymmetry [130, 131].

In this chapter, we discuss $\text{Ca}(\text{Fe}_{1-x}\text{Co}_x\text{As})_2$, with $x = 3 \pm 0.5\%$.¹ This is well on the underdoped side and, as will be shown later, in the orthorhombic regime. Fig. 8.2 shows a topograph of $\text{Ca}(\text{Fe}_{0.97}\text{Co}_{0.03}\text{As})_2$. Immediately visible is the mostly debris free, atomically flat surface with a 1×2 surface reconstruction (blue and red arrows in inset), also observed in LEED experiments [126, 132]. This surface reconstruction is prevalent on 122 surfaces [121, 122, 133, 123, 124, 125, 126]. For reasons not yet clear, it is very hard to image single atoms on the $\text{Ca}(\text{Fe}_{1-x}\text{Co}_x\text{As})_2$ surface, and for that matter, on most 122 surfaces. Only very low junction resistance topographs show atomic resolution, and even there, not single atoms but rather dimers

¹The doping is rather inhomogeneous, we will discuss this on page 8.

are visible (Fig. 8.2, inset). Perhaps for this reason, it is not absolutely clear what the cleaving surface is and how the atoms on the top-layer arrange themselves. Given that the covalent bonds between iron and arsenic are very strong, the two possibilities are FeAs or Ca terminated surfaces (c.f. Fig. 7.3). Based on various arguments, most of the literature seems to favor the FeAs terminated picture; discussed is also the possibility that about half the Ca atoms stay on the surface and are involved in the formation of the 2×1 superstructure [123, 132, 125, 126, 134, 122]. Some STM images indicate a possible dimerization of the surface [126].

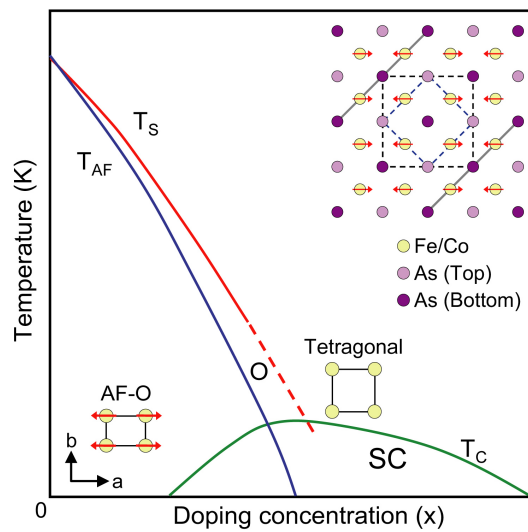


Figure 8.1: Schematic phase diagram of $R(\text{Fe}_{1-x}\text{Co}_x)_2\text{As}_2$ (here $R = \text{Ca}, \text{Sr}, \text{or Ba}$) as function of doping concentration x [99, 100, 117, 129]. Red, blue, and green curves show the transition temperature for structure (T_S), antiferromagnetism (T_{AF}), and superconductivity (T_C), respectively. The red arrows indicate the spin orientation for each Fe atom in the antiferromagnetic-orthorhombic phase. *Upper right*, FeAs layer showing the unit cell in tetragonal (blue dashed lines) and orthorhombic (black dashed lines) phases. The orientation and periodicity of the surface reconstruction in the topographic images in Fig. 8.2 is indicated by gray lines.

We now want to turn our attention towards the underlying atomic structure. At low doping, $\text{Ca}(\text{Fe}_{1-x}\text{Co}_x\text{As})_2$ is an orthorhombic material, and as such it has, albeit a and b are less than 1% different, a 180° -symmetric (C_2) crystal structure [117]. It is thus important to know if the sample studied is in the orthorhombic or tetragonal phase. Although the qualitative phase diagram is known to be similar to those reported for BaFe_2As_2 , the heterogeneity of doping so far prevents the measurement of the exact doping at

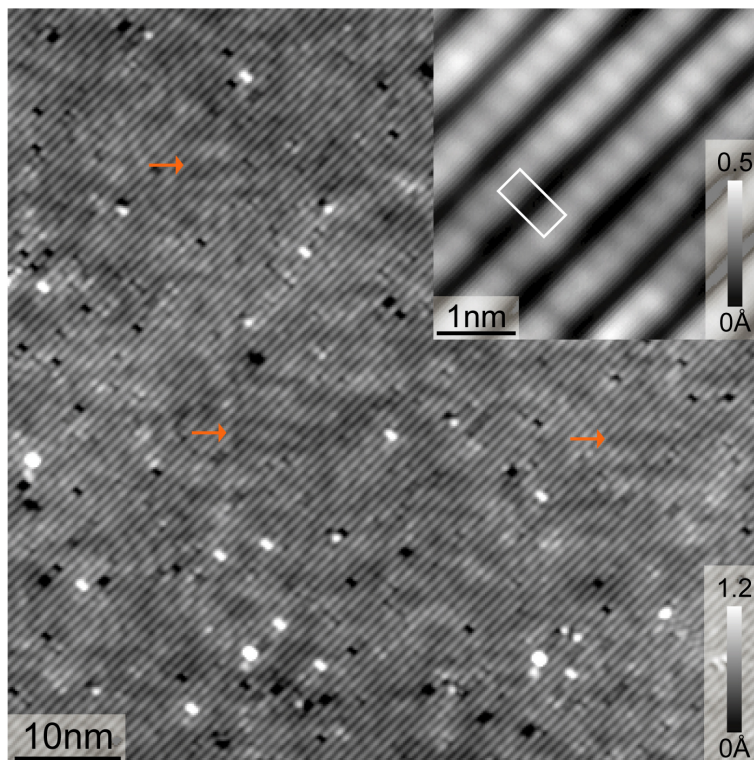


Figure 8.2: Constant-current topographic image of $\text{Ca}(\text{Fe}_{1-x}\text{Co}_x\text{As})_2$ taken at $V_B = -50$ mV and $I_0 = 10$ pA on a 71×71 nm² FOV. Inset: a high resolution topograph in a smaller FOV (4.2nm-square) taken at $V_B = -5$ mV and $I_0 = 100$ pA. The white box marks the 1×2 surface reconstruction. The orange arrows indicate the first indications of unidirectional electronic nano-pattern.

which the low temperature structural phase transition occurs.

A standard method to measure doping concentration is wavelength dispersive X-ray spectroscopy. This technique uses the fact that, when irradiated with X-ray light, different atoms emit electrons at different, atom-specific energies, allowing us to measure their relative molar concentrations (for a review, c.f. Ref. [135]). We performed X-ray spectroscopy experiments on our samples, and obtained very inhomogeneous dopings. On the sample studies in this thesis, we measured with a spot size of $200 \mu\text{m}$, and obtained 3.63%, 3.49%, 2.74%, 2.66%, 2.67%, 2.98%, 2.90%, 2.47% and 3.03% doping at different random locations, i.e. $3 \pm 0.4\%$ on average. On different samples of the same batch, we obtained $4.6 \pm 1\%$. Obviously, this cannot answer the question about the exact location in the phase diagram, but tells us that we measure samples well on the underdoped, orthorhombic and antiferromagnetic side.

8.1 Static nematic pattern in $\text{Ca}(\text{Fe}_{0.97}\text{Co}_{0.03}\text{As})_2$

Detailed examination of topographic images of $\text{Ca}(\text{Fe}_{1-x}\text{Co}_x\text{As})_2$ surface reveals a surprising fact: it appears to show faint unidirectional structures (Fig. 8.2, orange arrows). When two identical atomically registered topographs, taken at $V_B = \pm 50$ meV, are subtracted to cancel the signal of the surface reconstruction and topographic disorder, unidirectional nano-pattern are seen. Since topographs represent a logarithmic measure of the integrated density of states [22], this means there exists some form of non-dispersive electronic unidirectionality. To get a clearer picture of any such electronic nano-pattern, we image the energy-resolved $LDOS(\mathbf{r}, E_B)$ in the same FOV. Unidirectional electronic nano-pattern with different magnitude are detected in all low energy $g(\mathbf{r}, E)$ images in a $\sim \pm 100$ meV range. These nano-pattern are non-dispersive in the sense that they change very little over the energy range in which they are visible (c.f. section 8.2).

The C_2 unidirectionality exhibits itself very clearly in the autocorrelation $AC(g(\mathbf{r}, E))$: Apart from the central peak, there are two clear peaks along the same direction as the unidirectional electronic structure is observed (Fig. 8.3E,F). This not only shows a clear unidirectionality, but also a characteristic distance of $\sim 8a_{\text{FeFe}}$ at which a *self-similarity* is present. This self-similarity is short-ranged, there are no peaks in the Fourier transform indicative of long-range order. In this thesis, we will refer to the conductance pattern causing this unidirectionality as ‘static nematic pattern’ (SNP).

Note that the directionality of the SNP is independent of the surface reconstruction that is aligned at a relative angle of $\pm 45^\circ$. Fig. 8.4A shows a topographic image of the $\text{Ca}(\text{Fe}_{0.97}\text{Co}_{0.03}\text{As})_2$ surface with surface reconstructions in two different directions. Clearly, the unidirectional nano-pattern (Fig. 8.4B) is not influenced by the boundary of the surface reconstruction. This shows that the SNP is indeed a bulk property unaffected by the reconstruction at the surface.

8.1.1 Domain boundaries

In the orthorhombic phase, there is a structural directionality in $\text{Ca}(\text{Fe}_{1-x}\text{Co}_x\text{As})_2$, and since our crystal is not de-twinned, different orthorhombic domains exist. Consequently, it might be expected that there are domains of the electronic directionality too. We searched for such domain boundaries, i.e. areas where the directionality of the electronic structure rotates by 90° , and indeed, we have found such areas where there are SNP domain boundary. Fig. 8.5 is a $g(\mathbf{r}, E = -37$ meV) conductance image on an area where the directionality of the unidirectional nano-pattern rotates by 90° . The boundary is straight

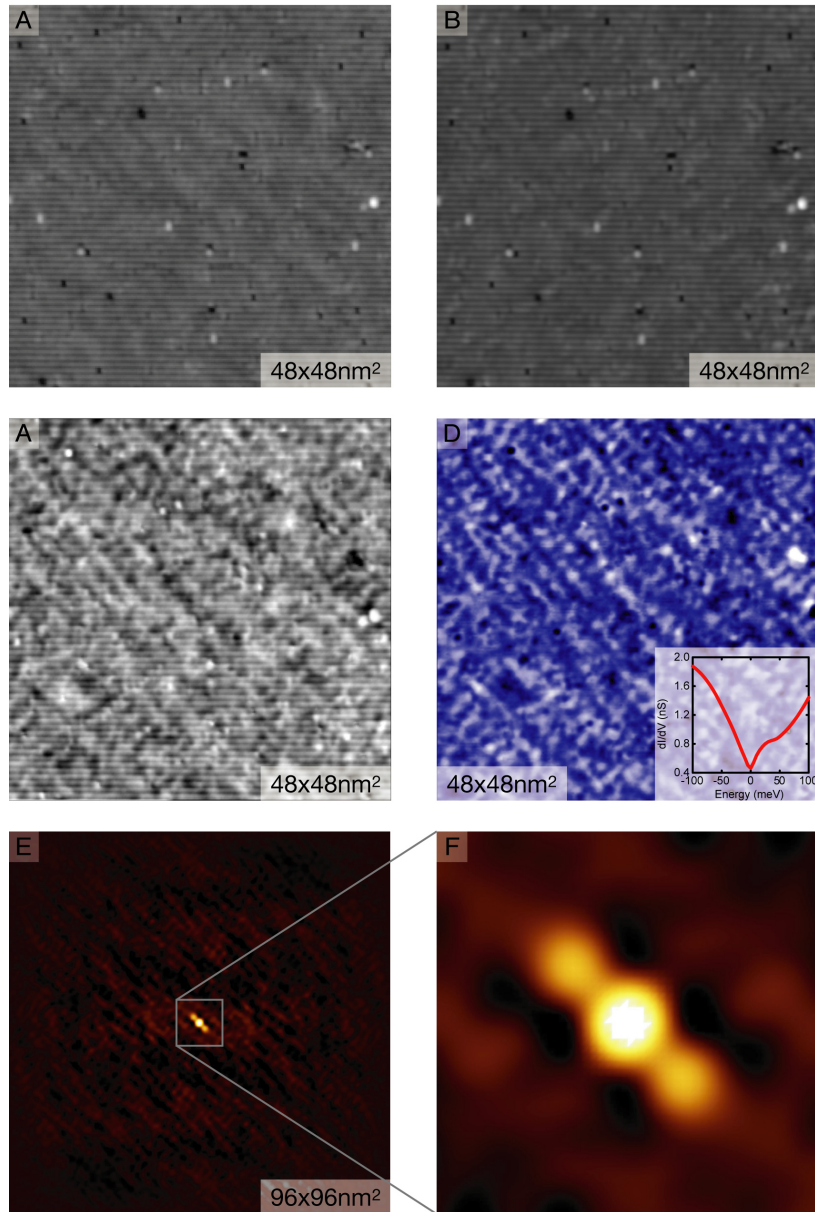


Figure 8.3: Unidirectionality in $\text{Ca}(\text{Fe}_{0.97}\text{Co}_{0.03}\text{As})_2$. (A,B) Topographic images taken at $V_B = +50, -50$ meV, respectively. (C), The subtraction removes topographic features and reveals electronic unidirectionality. (D), The same pattern can be seen in $g(\mathbf{r}, E = -37\text{meV})$ (for clarity we Fourier-filtered the 2×1 surface superstructure out, as we did in all following $g(\mathbf{r}, E)$ images). (E,F), The autocorrelation of $g(\mathbf{r}, E = -37\text{meV})$ shows that the unidirectionality stems from a $\sim 8 a_{\text{FeFe}}$ self-similarity.

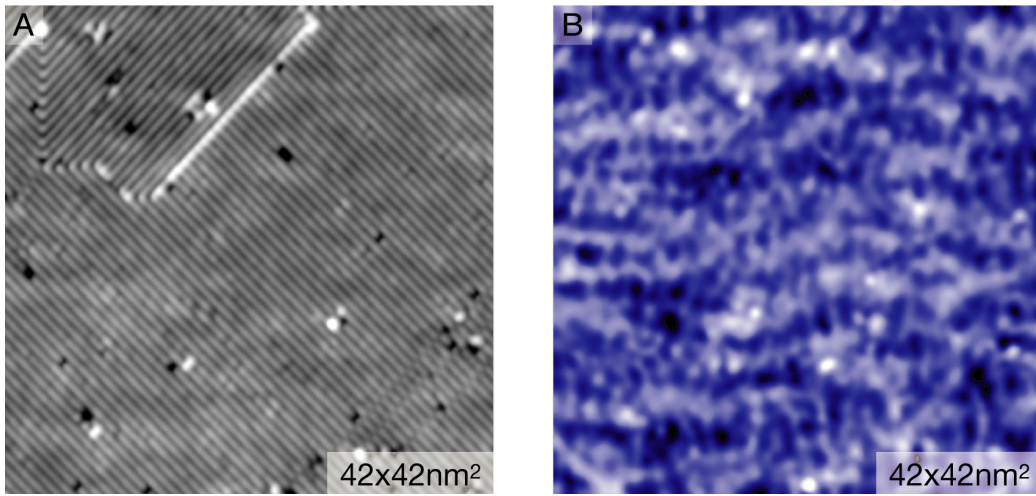


Figure 8.4: (A), Topographic image that spans a FOV with two different directions of surface reconstructions. (B), The conductance image $g(\mathbf{r}, E=-37\text{meV})$. The SNP is not influenced by the surface reconstruction.

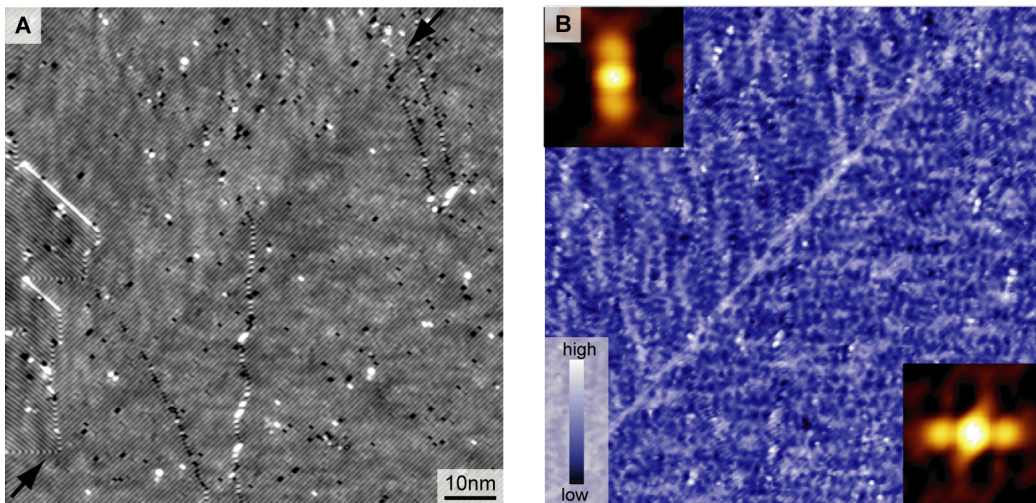


Figure 8.5: (A), Topographic image of a FOV spanning two different domains (the boundary marked by black arrows). (B), The conductance image $g(\mathbf{r}, E=-37\text{meV})$. Clearly the the directionality of the electronic structure rotates by 90° . The insets show the autocorrelations from the respective domains.

and aligned along the As-As direction, it is only weakly visible in the topographic image (Fig. 8.5A, arrows). We cannot yet conclusively determine if

a simultaneous twin boundary of the orthorhombic lattice induces the SNP to change directionality.

This observation of the SNP domain boundary is also very important for the following reason: Unidirectional signals in SI-STM are often a consequence of horizontally elongated or double tips, since the measured signal is always a function – approximately a convolution – of the tip and the sample. It is therefore important to exclude such an effect, and this is done here by showing different directionalities measured by the same tip.

8.1.2 Changes in the nematic pattern with varying energy

The $\text{Ca}(\text{Fe}_{0.97}\text{Co}_{0.03}\text{As})_2$ surface is very sensitive to high ($|V_B| \gtrsim 100$ mV) bias voltages. Consequently, most experiments were done at ± 50 to 70 mV. Since the SNP gives a strong signal in most of this range, the set-point effect (c.f. chapter 2) plays an important role.

Let us illustrate this with an example: Let us assumed that the SNP contrast is entirely ‘present’ at negative binding energies, and that the local density-of-states at positive binding energies is constant. Then, according to Eq. 2.5, the SNP contrast would be entirely normalized out at all negative conductance layers. However, at positive energies the SNP would appear.

This makes it very challenging to obtain information about particle-hole symmetry, a characteristic that is expected for e.g. polarons.

One way to track this problem is to look for the SNP signal in the autocorrelation of the topographs. Since topographic images represent a logarithmic measure of the integrated local density-of-states up to the bias voltage, this is unaffected by the set-point effect. However, topographic features shadow the SNP contrast. Only in the autocorrelation the nematic pattern is clearly visible. Based on this analysis (not shown), we can say that the SNP signal is mostly present at binding energies between -50 and 0 meV. On the positive side, the SNP is present too, but weaker. Lastly, from cross-correlation analysis, we can say that the contrast of the SNP inverts somewhere between 0 and 10 meV.

In summary, our analysis points towards a particle-hole antisymmetric SNP contrast that is much stronger on the negative side. We plan to do further work on this subject.

8.2 Dimer-shaped nematogens

We have seen that the electronic structure in $\text{Ca}(\text{Fe}_{0.97}\text{Co}_{0.03}\text{As})_2$ is highly unidirectional, with a self-similarity on a characteristic length-scale of $\sim 8a_{\text{FeFe}}$. This is consistent with neutron scattering experiments that measure a degree of magnetic anisotropy that cannot be explained with the miniscule lattice anisotropy [130, 131].

From these facts, some questions naturally arise: What is microscopic *source* of this unidirectionality? What possible electronic structures can lead to such an autocorrelation pattern? Are there any *nematogens*, i.e. can we deepen the comparison with liquid crystals, where the nematogens are anisotropic molecules? And finally, are there any *stripes*, as proposed by countless theoretical models?

We will try to answer some of these questions in the following section.

First, we reexamine the autocorrelation images (Fig. 8.3E,F). The triple peak indicates unidirectionality. Further, the absence of peaks in the Fourier transform indicates that there is no long-range order. The unidirectionality can therefore be categorized as *nematic*, and not as e.g. smectic or periodic ('stripy'). Almost as striking as the C_2 -triple peak is the *absence* of any other strong structure in the autocorrelation. This indicates that there is, other than the mentioned unidirectional self-similarity, no other electronic short-range correlation visible in the data. The only persistent length is $\sim 8a_{\text{FeFe}}$. This sets strong constraints on the nematogens leading to our pattern.

For example, if the nematogens were to be long objects, such as the proposed and measured [136, 137, 11] stripes in $\text{YBa}_2\text{Cu}_3\text{O}_{6+x}$, one would obviously see a very different autocorrelation. Even in the case that there exist different stripes which are only $8a_{\text{FeFe}}$ long, even in the case that they are curved, the autocorrelation would show an elongated single object, not a triple-peak, as illustrated in Fig. 8.6. Or, let us assume that the nematogens are some complicated object. This too would be reflected in the shape of the autocorrelation (Fig. 8.6, Chapter 1).

Let us now investigate what kind of conductance pattern could lead to the observed autocorrelation. The simplest solution is a random field of nematogens consisting of dimers of Gaussians, $\mathcal{N}(\mathbf{r}) = \mathcal{G}_\sigma(\mathbf{r} - \mathbf{d}/2) + \mathcal{G}_\sigma(\mathbf{r} + \mathbf{d}/2)$, with displacement $|\mathbf{d}| \approx 8a_{\text{FeFe}}$. Fig. 8.7 is a schematic illustration of such a dimer compared with the atomic lattice. Obviously, if these dimers are randomly scattered, there would be no signature in the autocorrelation except for the side-peaks, in agreement with the SI-STM data. Note that this is not only the simplest, but – if one assumes that all nematogens are equal and oriented – also the only possible set of nematogens resulting in such an autocorrelation pattern. Consequently, we want to investigate this

case in more detail.

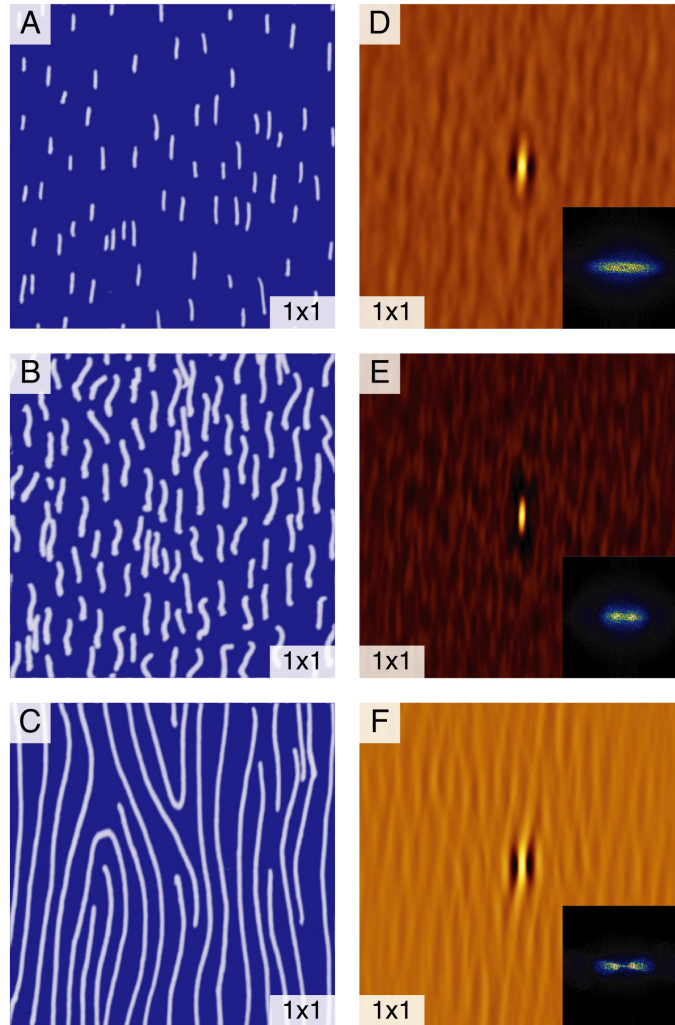


Figure 8.6: Schematic illustration on how different nematic pattern influence the auto-correlation. (A-C), 'Real space' pattern, either with elongated objects or nematicogens. Their shape is clearly reflected in the autocorrelation pattern (D-F). None of the shown pattern show clear unidirectional double peaks as observed on $\text{Ca}(\text{Fe}_{0.97}\text{Co}_{0.03}\text{As})_2$. The insets show the respective Fourier transforms with polynomial peaks indicating correlation.

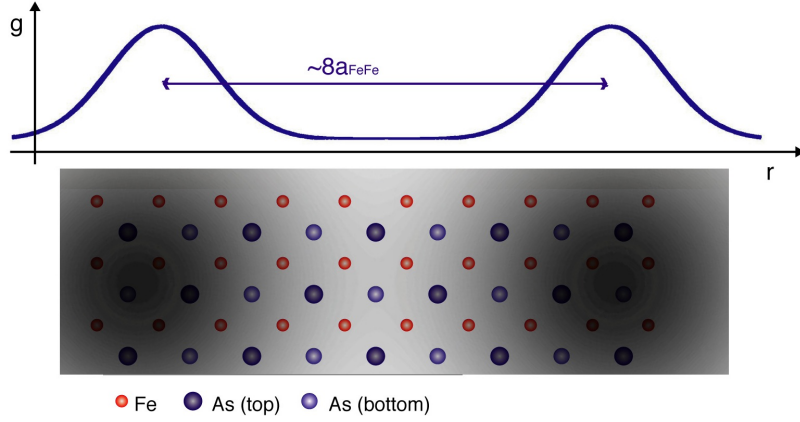


Figure 8.7: Schematic illustration of the proposed dimer-shaped nematogens $\mathcal{N}(\mathbf{r}) = \mathcal{G}_\sigma(\mathbf{r} - \mathbf{d}/2) + \mathcal{G}_\sigma(\mathbf{r} + \mathbf{d}/2)$. Top, a cut through one dimer. Bottom, the atomic lattice for comparison, with one dimer overlaid in grayscale. Note that the spacing of $\sim 8a_{\text{FeFe}}$ is large compared with the lattice spacings.

8.2.1 Simulations

Even though our hypothesis of dimer-shaped nematogens produces the right autocorrelation, at first sight, the $g(\mathbf{r}, E)$ images seem not indicative of such nematogens; by eye, no dimers are distinguishable. Could it be that many overlapping dimers make it impossible for the eye to pinpoint and identify single ones? To test this, we performed simulations. Fig. 8.8A-D show a $48 \times 48 \text{ nm}^2$ FOV with $N = 1, 12, 220, 2000$ nematogens as proposed, respectively. They obviously yield the correct autocorrelation (insets) by design. While one can distinguish single dimers at $N=1, 12$, it becomes harder at $N \approx 200$, and almost impossible at $N \approx 2000$. We emphasize that the dimers are randomly scattered; the apparent ‘stripe’ like features (orange arrow) are nothing but random accumulations of nematogens misleading the eye of the observer.

Clearly, the simulated images are qualitatively similar to our $g(\mathbf{r}, E=-37\text{meV})$ data, as long as $\frac{N}{\text{Area}} \gtrsim 0.2 \text{ nm}^{-2}$ (Fig. 8.9A,B show a comparison of the same FOV). The same holds for the autocorrelation (Fig. 8.9E,F) and for the Fourier transform (Fig. 8.9C,D). While this is trivial for the former (by design) it might not be obvious for the latter. We thus want to elaborate the Fourier transform one can expect from our proposed nematogene-generated $g(\mathbf{r}, E)$ above.

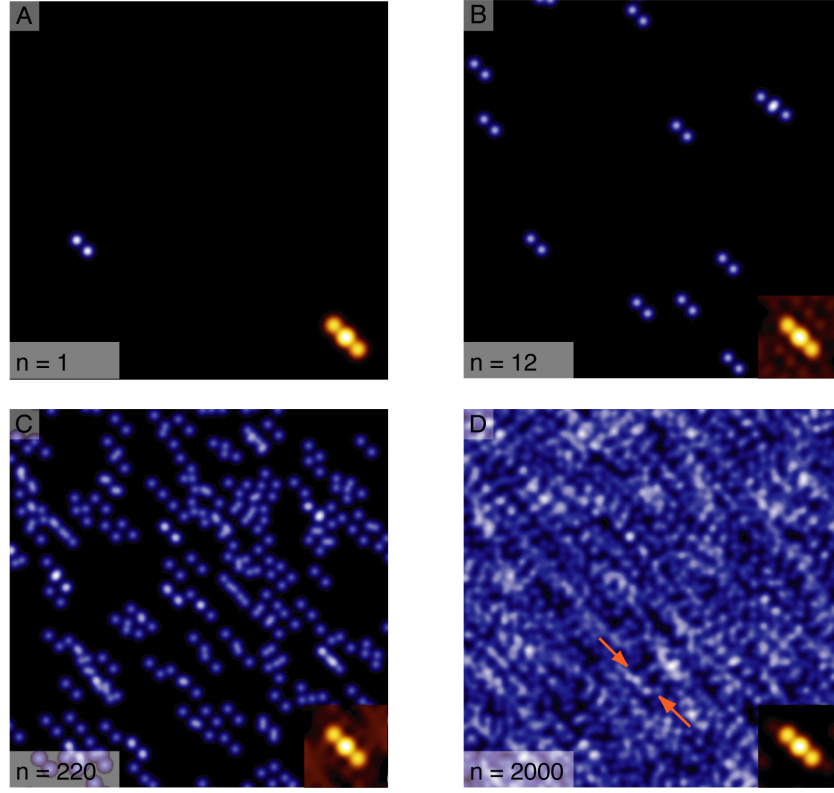


Figure 8.8: Simulations of randomly scattered dimers ($\mathcal{N} = \mathcal{G}_\sigma(\mathbf{r}-\mathbf{d}/2) + \mathcal{G}_\sigma(\mathbf{r}+\mathbf{d}/2)$, $|\mathbf{d}| \approx 8 a_{\text{FeFe}}$) on a $40 \times 40 \text{ nm}^2$ FOV, with N the number of dimers, $N=1, 12, 220, 2000$, respectively. The insets show the respective autocorrelations. Note that already at $N = 220$ it is not possible to distinguish every single dimer, at $N = 2000$ one can hardly distinguish any dimers.

8.2.2 Fourier transform of dimer-shaped nematogens

According to our hypothesis, the conductance consists of the sum of randomly scattered, dimer-shaped nematogens,

$$g(\mathbf{r}) = \sum_{\mathbf{R}_j \in \mathcal{R}} \mathcal{N}(\mathbf{r} - \mathbf{R}_j),$$

where \mathcal{R} is a set of random locations and $\mathcal{N}(\mathbf{r})$ is one nematogene consisting of a dimer of conductance maxima in the shape of two Gaussians peaks,

$$\mathcal{N}(\mathbf{r}) = \mathcal{G}_\sigma(\mathbf{r}) + \mathcal{G}_\sigma(\mathbf{r} + \mathbf{d}),$$

$$\mathcal{G}_\sigma(\mathbf{r}) = \left\{ a \cdot e^{-\frac{|\mathbf{r}|^2}{\sigma^2}} \right\} \text{ mS},$$

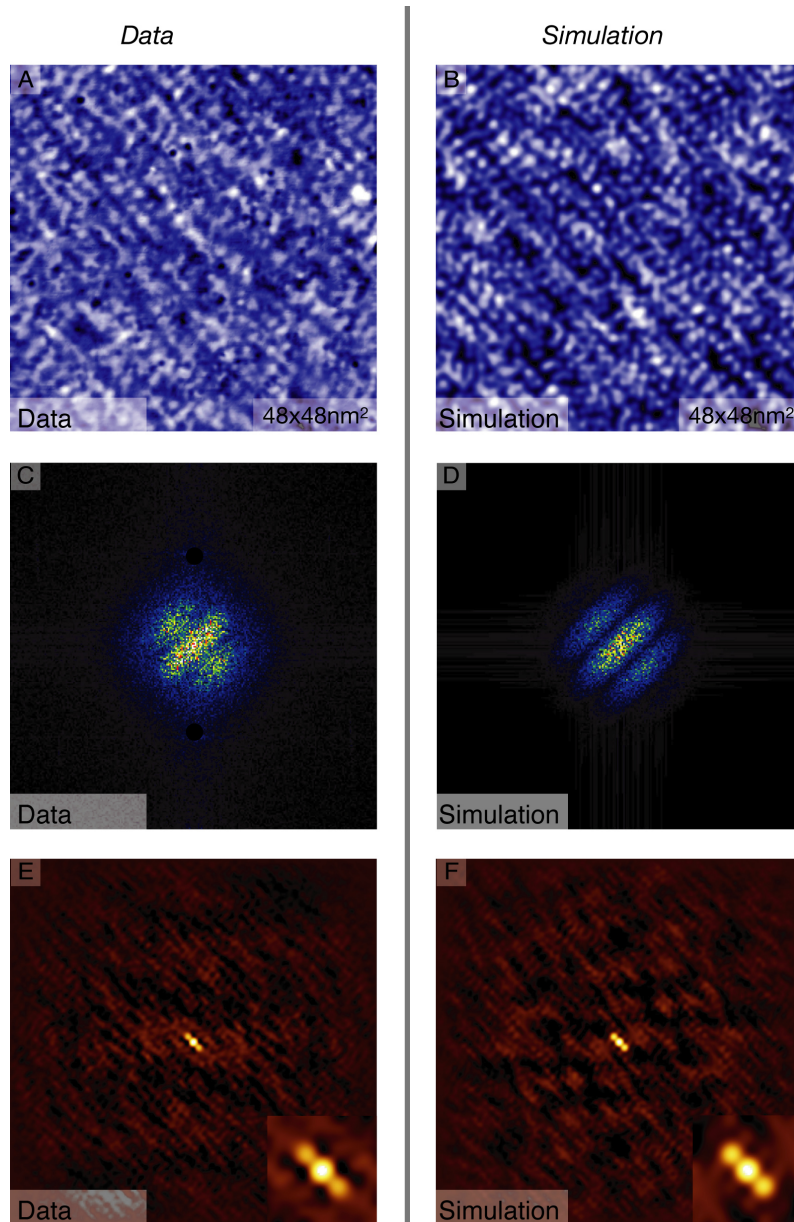


Figure 8.9: Comparison between the simulations shown in Fig. 8.8 and $g(\mathbf{r}, E=-37\text{meV})$ data from a FOV with the same size ($40\times 40\text{nm}^2$). The conductance (A,B), Fourier transform (C,D), and autocorrelation (E,F) look qualitatively similar. Again, the surface reconstruction in $g(\mathbf{r}, E=-37\text{meV})$ image (A) is removed by Fourier filtering, also visible in (C).

and $|\mathbf{d}|$ is the distance between the Gaussians within a dimer. Then we can rewrite $g(\mathbf{r})$ as a sum of two shifted function,

$$g(\mathbf{r}) = f(\mathbf{r} + \mathbf{d}) + f(\mathbf{r}),$$

with $f(\mathbf{r})$ the field of randomly scattered single Gaussians,

$$f(\mathbf{r}) = \sum_{\mathbf{R}_j \in \mathcal{R}} \mathcal{G}_\sigma(\mathbf{r} - \mathbf{R}_j).$$

The Fourier transform of such a function can be simplified as

$$\begin{aligned} \mathcal{F}\{g(\mathbf{r})\} &= \mathcal{F}\{f(\mathbf{r} + \mathbf{d})\} + \mathcal{F}\{f(\mathbf{r})\} \\ &= \int d\mathbf{r} e^{i\mathbf{r}\cdot\mathbf{q}} f(\mathbf{r}) + \int d\mathbf{r} e^{i\mathbf{r}\cdot\mathbf{q}} f(\mathbf{r} + \mathbf{d}) \\ &= \int d\mathbf{r} e^{i\mathbf{r}\cdot\mathbf{q}} f(\mathbf{r}) + \int d\mathbf{r} e^{i(\mathbf{r}+\mathbf{d})\cdot\mathbf{q}} f(\mathbf{r}) \\ &= (1 + e^{i\mathbf{d}\cdot\mathbf{q}}) \int d\mathbf{r} e^{i\mathbf{r}\cdot\mathbf{q}} f(\mathbf{r}) \\ &= (1 + e^{i\mathbf{d}\cdot\mathbf{q}}) \mathcal{F}\{f(\mathbf{r})\}. \end{aligned}$$

The last term can be explicitly calculated since

$$\begin{aligned} \mathcal{F}\{f(\mathbf{r})\} &= \mathcal{F}\left\{ \sum_{\mathbf{R}_j \in \mathcal{R}} \mathcal{G}_\sigma(\mathbf{r} - \mathbf{R}_j) \right\} \\ &= \int d\mathbf{r} \left\{ \sum_{\mathbf{R}_j \in \mathcal{R}} e^{i\mathbf{r}\cdot\mathbf{q}} \mathcal{G}_\sigma(\mathbf{r} - \mathbf{R}_j) \right\} \\ &= \sum_{\mathbf{R}_j \in \mathcal{R}} \left\{ \int d\mathbf{r} e^{-i\mathbf{R}_j\cdot\mathbf{q}} e^{i\mathbf{r}\cdot\mathbf{q}} \mathcal{G}_\sigma(\mathbf{r}) \right\} \\ &\approx \mathcal{G}_{1/\sigma}(\mathbf{q}). \end{aligned}$$

In the last step, we assumed the limit of many nematogens and a large FOV. The last term is real, and thus we measure

$$\begin{aligned} |\mathcal{F}\{g(\mathbf{r})\}| &= |e^{i\mathbf{d}\cdot\mathbf{q}} + 1| \cdot \mathcal{G}_{1/\sigma}(\mathbf{q}) \\ &= \sqrt{1 + e^{i\mathbf{d}\cdot\mathbf{q}} + e^{-i\mathbf{d}\cdot\mathbf{q}} + 1} \cdot \mathcal{G}_{1/\sigma}(\mathbf{q}) \\ &= \sqrt{2 + 2 \cos(\mathbf{d}\cdot\mathbf{q})} \cdot \mathcal{G}_{1/\sigma}(\mathbf{q}) \\ &= \sqrt{4 \cos^2(\mathbf{d}\cdot\mathbf{q}/2)} \cdot \mathcal{G}_{1/\sigma}(\mathbf{q}) \\ &= 2 |\cos(\mathbf{d}\cdot\mathbf{q}/2)| \cdot \mathcal{G}_{1/\sigma}(\mathbf{q}). \end{aligned}$$

This is a Gaussian peak modulated by $|\cos|$ with frequency $|\mathbf{d}|/2$. This not only explains the particular shape of the Fourier transform of the SNP, but also gives a way to extract the intra-dimer-distance from the data. One has to keep in mind that the \mathbf{q} -space resolution in our experiment is limited, influencing especially the sharp features from the $|\cos|$ term. This can be overcome by introducing a \mathbf{q} -resolution constant Λ_q . The final result is then obtained by convoluting $|\mathcal{F}\{g(\mathbf{r})\}|$ as calculated with an instrumental response function that limits the resolution, $\mathcal{G}_{\Lambda_q}(\mathbf{q})$, leading to

$$|\mathcal{F}\{g(\mathbf{r})\}| = \left(|\cos(\mathbf{d}\cdot\mathbf{q}/2)| \cdot \mathcal{G}_{1/\sigma}(\mathbf{q}) \right) * \mathcal{G}_{\Lambda_q}(\mathbf{q}),$$

where $*$ denotes the convolution.

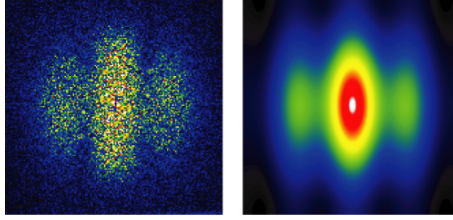


Figure 8.10: Two-dimensional fit (*right*) of the Fourier transform of $g(\mathbf{q}, E=-37\text{meV})$ (*left*) using $|\mathcal{F}\{g(\mathbf{r})\}| = (|\cos(\mathbf{d}\cdot\mathbf{q}/2)| \cdot \mathcal{G}_{1/\sigma}(\mathbf{q})) * \mathcal{G}_{\Lambda_q}(\mathbf{q})$, yielding $(\sigma, \Lambda_q, |\mathbf{d}|) = (1/6.1 \text{ \AA}^{-1}, 1/16 \text{ \AA}^{-1}, 21.8 \text{ \AA})$. More details are given in the text and in Fig. 8.12.

Using above formula, we performed two-dimensional fitting on the Fourier transform of the SNP, with parameters σ , Λ_q , \mathbf{d} , as well as a constant factor and constant background. Fig. 8.10 shows an example, the obtained fitting parameters are $(\sigma, \Lambda_q, |\mathbf{d}|) = (1/6.1 \text{ \AA}^{-1}, 1/16 \text{ \AA}^{-1}, 21.8 \text{ \AA})$. We did this for all $g(\mathbf{r}, E)$ layers showing the SNP.

A more direct way to obtain the intra-dimer-distance is to fit the auto-correlation of the SNP with three Gaussians. This directly yields the characteristic distance of self-similarity. The fit in Fig. 8.11 gives the parameters $(\sigma, |\mathbf{d}|) = (6.7 \text{ \AA}, 19.1 \text{ \AA})$, Fig. 8.12A shows fits for different $g(\mathbf{r}, E)$ energy layers. Fig. 8.12C compares the results for the autocorrelation and Fourier transform fits. The intra-dimer-distances agree well. The distance is weakly varying between 7 and 9 a_{FeFe} as a function of energy.

8.2.3 Impurity imaging

The conductance $g(\mathbf{r}, E)$ images at energies of 100 meV to 200 meV show local maxima (Fig. 8.13), similar to the ones observed at oxygen dopant location

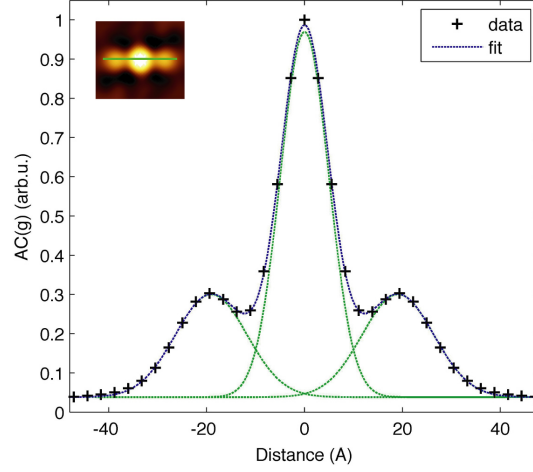


Figure 8.11: Fit of a cut trough the autocorrelation that shows the central peak as well as the two side-peaks. The shape can be fitted to three Gaussians; the distance between them gives the intra-dimer-distance, c.f. Fig. 8.12.

in $\text{Bi}_2\text{Sr}_2\text{CaCu}_2\text{O}_{8+\delta}$ [33]. We identify these maxima to be some sort of impurity. Averaging all spectra at such peak locations leads to a peak in the $LDOS(\mathbf{r} = \mathbf{r}_{imp}, E)$, indicating some form of impurity state. Intriguingly, this peak is at the same energy as the impurity peak predicted by LDA calculations for Co doping in BaFe_2As_2 [128]. To test if these peaks stem from cobalt dopants, we checked for their signature in pure CaFe_2As_2 , and in fact, it was absent. We thus identify the conductance peak at ~ 120 meV with cobalt.

The total number of impurity atoms in the $64 \times 64 \text{ nm}^2$ FOV shown in Fig. 8.13A is ~ 260 , much less than the ~ 1600 expected from 3% Co doping. The inhomogeneous doping of the sample cannot explain this, the wavelength dispersion spectroscopy measurements consistently yielded higher values than all the doping counts, and this explanation is thus statistically highly unlikely. The reason for the discrepancy in doping values is so far unknown, one can speculate about the Co dopants being in different electronic states with only one state detectable by our method.

Next, we would like to elaborate a possible connection between the nematogens and the impurity locations. The standard procedure is to cross-correlate the image of the impurity locations, $Co(\mathbf{r})$, with the relevant $g(\mathbf{r}, E)$ image [33]. However, this is not a suitable method in this case, since even if every Co location would pin down a nematogene, the cross-correlation would

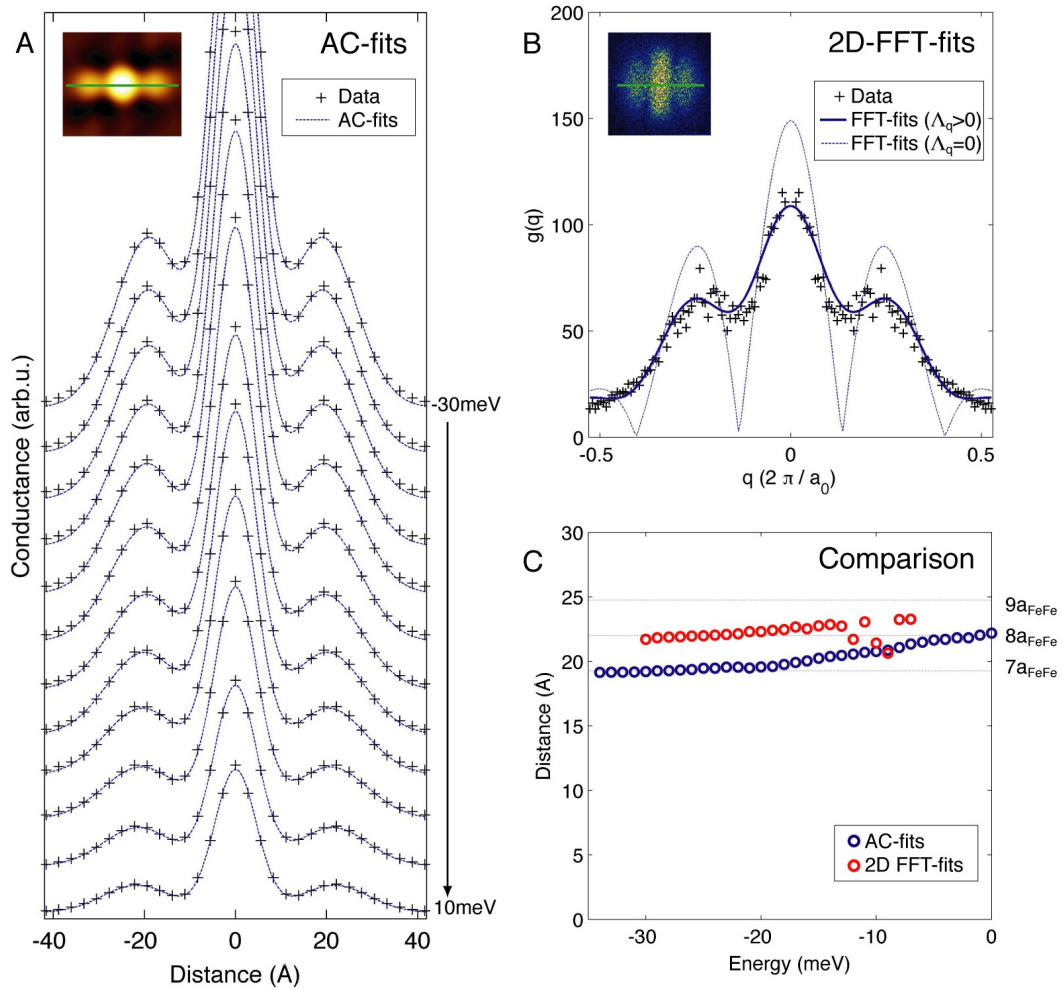


Figure 8.12: Extracting the intra-dimer-distance. (A), Cuts through the autocorrelation at various binding energies. The inset shows the location of the cuts in the autocorrelation. The three peaks fit well to a triplet of Gaussians, yielding the intra-dimer-distance. Alternatively, one can 2d-fit the Fourier transform $\mathcal{F}\{g(E)\}$ using a Gaussian modulated by $|\cos|$ (c.f. text). Fig. 8.10 shows such a two-dimensional fit; (B) shows a cut along the axis of the dimers. The inset shows the location of the cuts in the Fourier transform. (C), The two methods agree well and show that the intra-dimer-distance $|d|$ is fairly constant with changing binding energy.

not yield a high value, since there are much more dimers than dopants. We take another route: Cropping the local environment around each impurity (Fig. 8.14A) and summing up all these local patches, one can average out background noise and overlapping signatures. The resulting image is shown

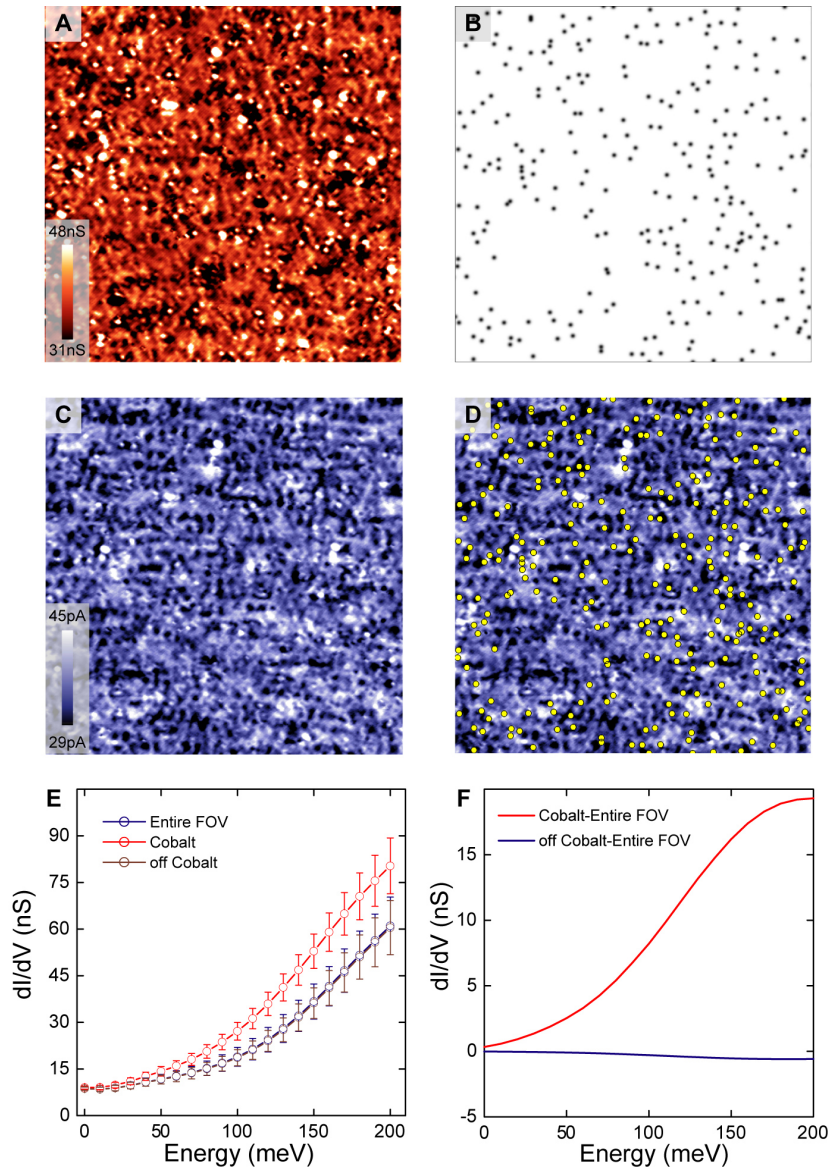


Figure 8.13: (A), The conductance peaks at the impurity locations \mathbf{r}_i at $E_B = 120$ meV. (B), schematic representations of the impurity locations extracted from (A). (C), SNP at $g(\mathbf{r}, E = -37$ meV) and (D), the same with impurity locations marked as yellow spots. The impurity state shows up as a peak in the conductance around 150 meV (F) or as a higher slope in the current (E). In (F), we subtracted the average conductance spectrum for clarity.

in Fig. 8.14B. Clearly there is C_2 symmetry present, and two peaks with the expected $\sim \delta a_{\text{FeFe}}$ separation. The image is, however, not as clear as one

would expect. We therefore think that there is some degree of pinning, but are unsure about the extent of it.

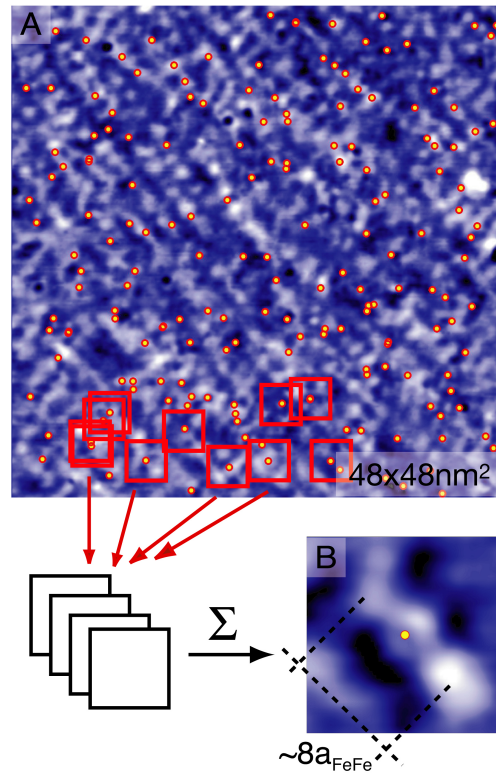


Figure 8.14: Averaging over impurity locations. (A), $g(\mathbf{r}, E=-37\text{meV})$ with the impurity locations from Fig. 8.13 overlaid. Taking the the local environment around each dopants and summing up all these local patches, one can average out background noise and overlapping signatures. The dopants are marked by yellow dots in (A), and some of the local patches that are cropped are marked by red boxes. (B), The resulting ‘impurity-averaged’ image shows a weak circle around the impurity and a dimer of peaks like the one proposed as nematogens.

8.3 C₂-quasiparticle interference

One of the great advantages of SI-STM is the possibility to simultaneously image the localized states (\mathbf{r} -space) and itinerant (\mathbf{k} -space) quasiparticles. In this section we discuss the dynamic electronic states detected in $\text{Ca}(\text{Fe}_{1-x}\text{Co}_x\text{As})_2$ by QPI and their relation to the nematogens and to other probes.

As explained in chapter 2, a QPI signal is best viewed in the Fourier transform of the conductance $g(\mathbf{q}, E)$. In the case of $\text{Ca}(\text{Fe}_{0.97}\text{Co}_{0.03}\text{As})_2$, the Fourier transform includes not only the QPI signal, but also a non-dispersive signal from the SNP, which is strong enough to shadow the QPI. Since the spectroscopy experiments discussed in this section are set-up at positive bias, the SNP signal is suppressed on positive layers, but not on negative (c.f. chapter 2). To avoid SNP signatures oppressing the QPI signal, we subtract the former from the latter, i.e.

$$\begin{aligned} g_{\text{QPI}}(\mathbf{r}, E) &= g_{\text{raw}}(\mathbf{r}, E) - g_{\text{SNP}}(\mathbf{r}, E) \\ &= g_{\text{raw}}(\mathbf{r}, E) - 0.6g_{\text{raw}}(\mathbf{r}, E = -37\text{meV}). \end{aligned}$$

The factor of 0.6 is chosen to maximize the QPI signal. (This is done to increase the visibility of the peaks, their dispersion is independent of this.)

Fig. 8.15 shows a sequence of conductance images prepared like this at different energies. Dispersing pattern are visible with increasing wavelength for increasing energies. The Fourier transforms, $g(\mathbf{q}, E)$, show 6 peaks at the corresponding \mathbf{q} -vectors that disperse with energy.

Before further analysis, we perform three steps to enhance the visibility of the raw QPI data (Fig. 8.15) and to obtain the images shown in Fig. 8.16A-J. First, we symmetrize the data along the symmetry axes of the orthorhombic lattice, i.e. the a - and b - axes. Second, we deal with the center peak around $\mathbf{q}=(0,0)$. This peak stems from long range spatial variations of the surface and from randomly scattered defects; it is not related to quasiparticle scattering. We thus suppress the intensity of very small \mathbf{q} -vectors around the center, explicitly $QPI = QPI_{\text{raw}} \cdot (1 - 0.97\mathcal{G}_\sigma(\mathbf{q}))$, with the width of the Gaussian \mathcal{G}_σ chosen to only suppress the intensity of \mathbf{q} -vectors smaller than the dispersing peaks discussed in this section. Last, we low-pass-filter the $g(\mathbf{q}, E)$ images to reduce the high frequency noise.

Fig. 8.16A-J show the resulting images processed that way. The wavelength of the QPI peaks is long compared to $2\pi/a_0$ (Fig. 8.16K), and increases with increasing energy. We extract the 6 peak positions in $g(\mathbf{q}, E)$ from Fig. 8.16A-J and plot them versus E_B in Fig. 8.16L. The two center peaks show hole-like dispersion towards the center, and their trajectory $\mathbf{q}(E)$ is mimicked by two pairs of side-peaks. Intriguingly, they are $2\pi/(8a_{\text{FeFe}})$ apart from the center peak; we will discuss this later.

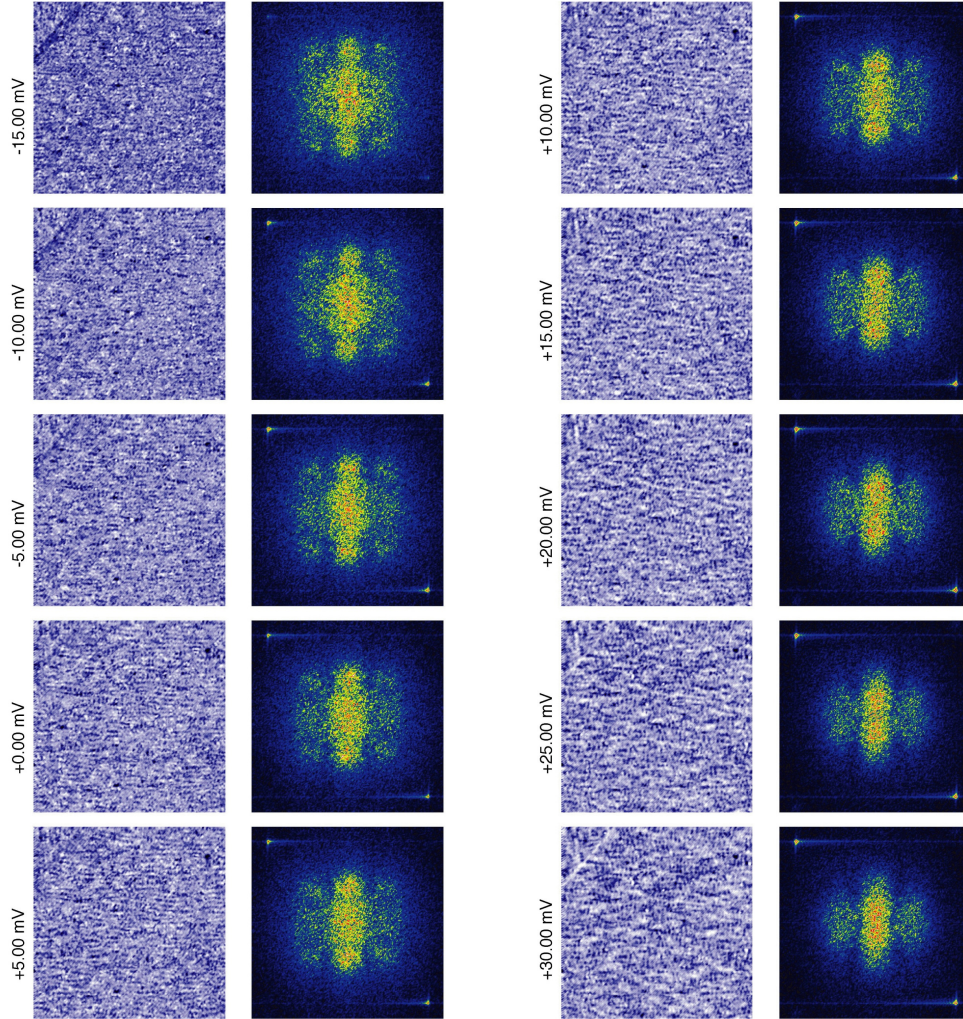


Figure 8.15: *Left columns*, A sequence of $g_{\text{QPI}}(E) = g_{\text{raw}}(E) - 0.6g_{\text{raw}}(E = -37\text{meV})$ images from $E = -30$ meV to 10 meV on a 94×94 nm² FOV. The patterns in each image disperse vertically and to longer wavelength with increasing energy. *Right columns*, The Fourier transforms of the images reveal the C_2 -symmetric structure of the QPI patterns. Six dispersing peaks are clearly visible. The two center peaks disperse in a hole-like fashion and along one axis only. Pairs of side peaks mimic their dispersion at $q_{\pm} \approx 2\pi/(8a_{\text{FeFe}})$. The peaks in two diagonal corners of each image stem from the \mathbf{q} -space locations of the 1×2 reconstruction.

In Fig. 8.17, we compare the $\mathbf{k}(E) = \mathbf{q}(E)/2$ trajectories with the dispersion of the α_2 band measured by ARPES by Kondo *et al.* [127]. For this, we shift the QPI data points by 12.5 meV to account for the possible shift in

E_{Fermi} induced by Co-doping (the ARPES data stem from pure CaFe_2As_2). The QPI and ARPES data agree for the Fermi vector and Fermi velocity.

One obvious question is why we see a set of 6 peaks with a C_2 -dispersion, and not a C_4 symmetric image as measured by ARPES. Here, one has to note that the spot-size for ARPES is much larger than typical orthorhombic domain sizes in $\text{Ca}(\text{Fe}_{1-x}\text{Co}_x\text{As})_2$, so all experiments reported in the literature average over several domains. Furthermore, possible C_2 signatures from ARPES have to be taken with caution, since these experiments often show a directionality for geometric reasons, because the scattering plane (defined by incoming beam and photoelectron) breaks rotational symmetry. Often, C_4 is further broken by the polarization of the incoming photons. Thus, if one wants to study nematicity with ARPES on non-detwinned crystals, one has to design the experiment very carefully [13, 138].²

Even if the apparent disagreement with ARPES is perhaps not so surprising, one has to wonder why we measure such particular dispersion. One could perhaps speculate that the 6 peaks stem from enhanced density of states at certain \mathbf{k} -points due to back-folding of the bands according to the new $\sim 8a_{\text{FeFe}}$ ‘quasi-periodicity’. This leads to the right location for the peaks and would further explain the unidirectional dispersion.

Let us alternatively assume that the QPI actually stem from a C_4 band that is unaffected by the nematic pattern, but is scattered by the discussed dimers. What signal would one expect? Capriotti *et al.* calculated the expected difference in the density-of-states δN for a two-dimensional metal:

$$\delta N(\mathbf{r}, \omega) = -\frac{1}{\pi} \text{Im} \int d\mathbf{r}' G_0(\mathbf{r} - \mathbf{r}', \omega) V(\mathbf{r}) G_0(\mathbf{r} - \mathbf{r}', \omega).$$

$G_0(\mathbf{r})$ is the Green’s function of the unperturbed system, and $V(\mathbf{r})$ is the scattering potential. Assuming a weak potential, this leads to the following QPI pattern:

$$|\delta N(\mathbf{r}, \omega)|^2 \propto \left| \frac{1}{\pi} \text{Im} \int d\mathbf{r}' e^{i\mathbf{q}\cdot\mathbf{r}} G_0(\mathbf{r}, \omega) V(\mathbf{r}) G_0(-\mathbf{r}, \omega) \right|^2 |V(\mathbf{q})|^2.$$

The first term describes the bare quasiparticle interference and the last term is the structure factor of the scattering potential. In most cases, the spatial dimension of the scattering potential is small compared to the wavelength, and the scattering potential is nearly constant, in case of a perfect point scatterer it is even exactly a constant. In our case, we assume the scatterer to be a dimer, with spacial dimensions larger than the QPI wavelength,

²Recently, ARPES work on de-twinned crystals confirmed strong electronic unidirectionality and measured the shape of the C_2 symmetric Fermi pockets.

and consequently, we have to take the structure factor into account. The calculation is similar to section 8.2.2; the basic shape is a Gaussian with $|\cos(\mathbf{d}\cdot\mathbf{q}/2)|$ modulation. Thus the C_4 signal from a $C_4\text{-}\alpha_2$ band will be multiplied by a C_2 structure factor proportional to $|\cos(\mathbf{d}\cdot\mathbf{q}/2)|$. This is consistent with our data.

An important test of the proposed picture is to check the change of QPI directionality over the domain boundary observed in the SNP. This is shown in Fig. 8.18 where QPI pattern at $E = -10$ meV of the respective domains are plotted, and indeed, the directionality rotates by 90° .

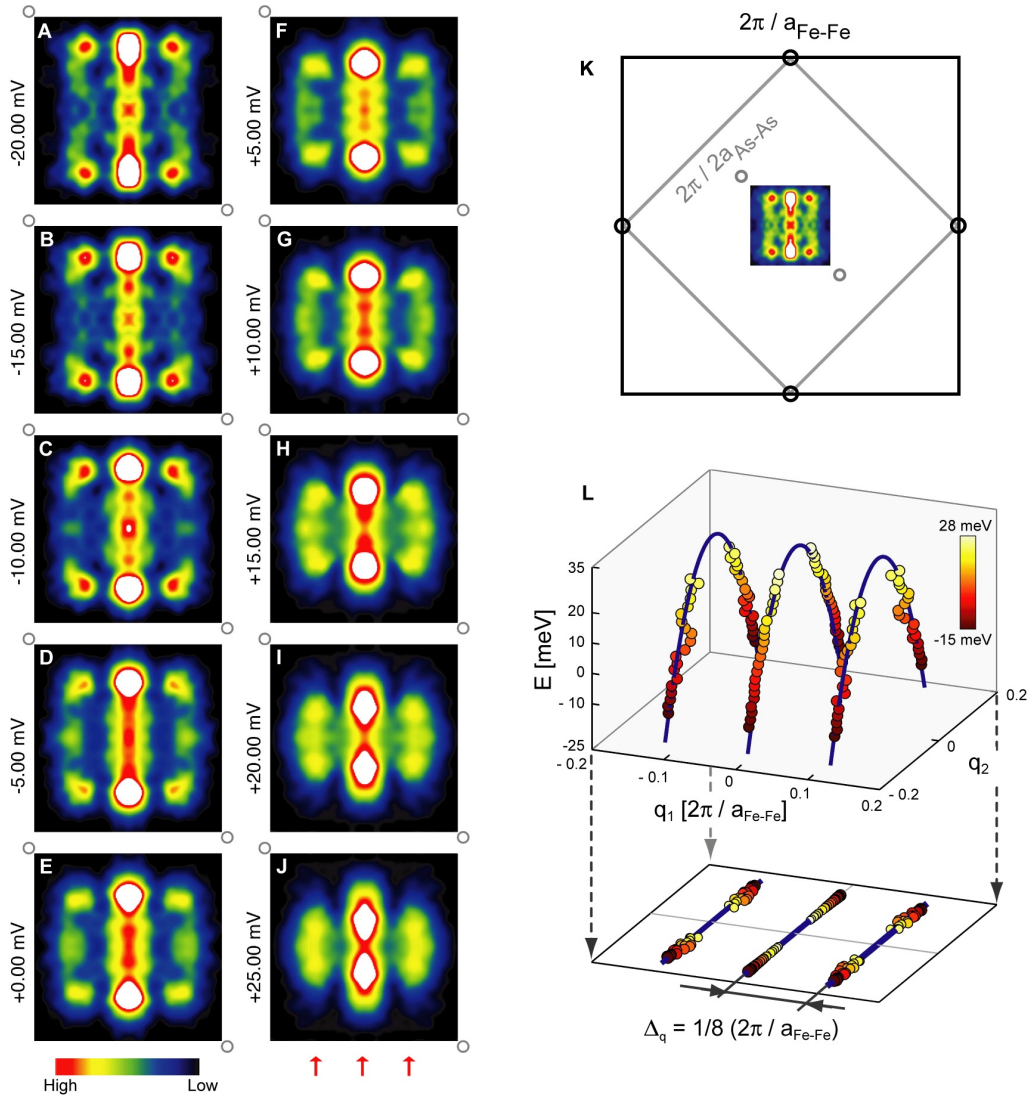


Figure 8.16: (A to J), The enhanced Fourier transform images $g(\mathbf{q}, E)$ from a $94 \times 94 \text{ nm}^2$ FOV conductance images reveal the highly C_2 -symmetric structure of the QPI patterns. Six dispersing peaks are clearly visible. The two center peaks disperse in a hole-like fashion along one axis only. Pairs of side peaks mimic their dispersion at $q_{\pm} \approx 2\pi/(8a_{\text{Fe-Fe}})$. The open circles at two corners of each image represent the \mathbf{q} -space locations of the 2×1 reconstruction. Red arrows indicate the three parallel dispersion trajectories. (K), Overview of the different directions and length scales in \mathbf{q} -space. The dispersing QPI vectors are short compared with the $2\pi/a_{\text{Fe-Fe}}$ box that spans all scattering vectors in the first Fe-Fe Brillouin zone (the large black box). The small gray box indicates the first As-As reciprocal unit cell. (L) The hole-like dispersion of QPI, plotted in (q_a, q_b, E) space. Circles mark the positions of the six dispersion peaks extracted from each $g(\mathbf{q}, E)$ image; the blue lines are the parabolic fit for QPI. Projections to the (q_a, q_b) plane emphasize how unidirectional the dispersions are.

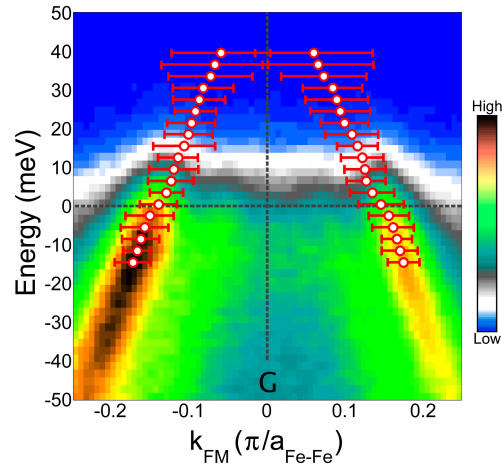


Figure 8.17: The comparison between QPI (red circles filled in white) and angle resolved photoemission spectroscopy (ARPES) data (background) of α_2 band (adopted from Ref. [127] by the courtesy of Adam Kaminski). Here, the ARPES data is measured on pure CaFe_2As_2 at $T=40$ K with photon energy=105 eV and our QPI data is measured on underdoped $\text{Ca}(\text{Fe}_{0.97}\text{Co}_{0.03}\text{As})_2$ at $T=4.3$ K with energy range between +27 meV and -27 meV. Possibly due to the difference in doping level, the chemical potential of the QPI data is shifted by +12.5 meV to fit the α_2 band observed by ARPES.

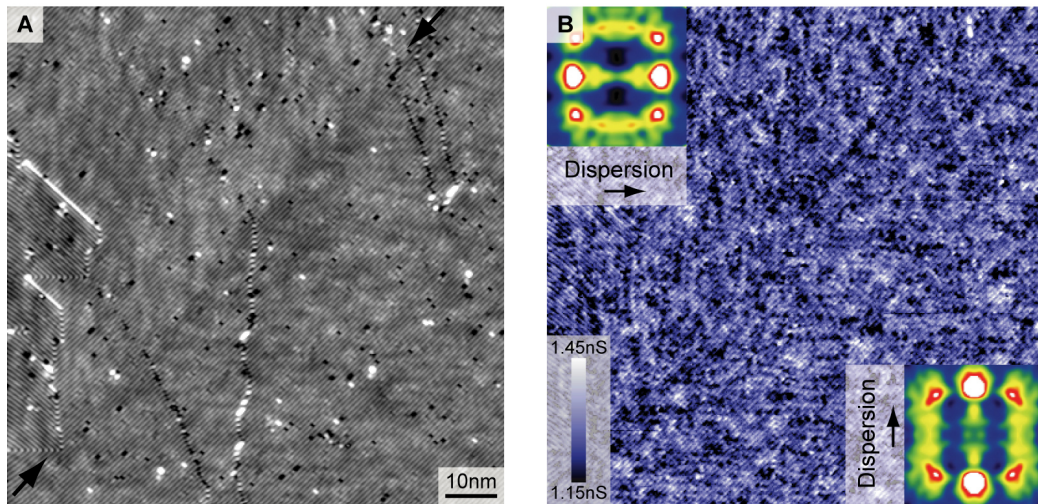


Figure 8.18: (A), Topographic image of a FOV spanning two different domains (the boundaries marked by black arrows). (B), The conductance layer $g(\mathbf{r}, E = -10\text{meV})$, and the Fourier transform of the respective domains (inset). The directionalities of the QPI dispersion rotate by 90° .

8.4 Concluding remarks

Glassy character of the nematic electronic state

After having proposed dimer-shaped nematogens as a source of the SNP, we would like to briefly discuss the consequences this has to the analogy to liquid crystals that is sometimes suggested in this thesis. That there is directional order without translations symmetry is clear. However, the term ‘liquid’ has to be used with more care. The nematogens we observe are, on the time scales of SI-STM, static in time. In case of a liquid crystal, this would be like a ‘photograph’ of the liquid of anisotropic molecules. Our case is thus more glass-like than liquid-like. Of course the static pattern could arise from scattering of itinerant quasiparticles, it might come from ‘nano-domains’ of itinerant quasiparticles, and so on. As of now, however, our data point towards a glassy state.

Intriguingly, recent neutron scattering groups reported a spin glass regime in a small region of the underdoped state of $\text{Fe}_{1+y}\text{Se}_x\text{Te}_{1-x}$. We hope further investigations will show possible connections to the nematogens in $\text{Ca}(\text{Fe}_{0.97}\text{Co}_{0.03}\text{As})_2$.

Physical origin of the nematogens / future work

Future work will likely concentrate on the physical origin of the nematogens. We would like to briefly speculate about some possibilities here:

- Ideas of **preformed singlets** that condense into the superconducting state are widespread. If these are pinned down, one might be able to see them in a conductance map. Their shape would depend much on the pairing symmetry.
- We mentioned the possible pinning of dimer-shaped nematogens by the Co-signatures, and the discrepancy of observed impurity states and the expected number of Co-atoms (section 8.2.3). Looking at the spatially extended impurity states that Zn atoms have in $\text{Bi}_2\text{Sr}_2\text{CaCu}_2\text{O}_{8+\delta}$ [139], one can speculate that the nematogens actually are such **impurity states of the Co-atoms**, and that we only image some of them at the discussed 120 meV feature. However, it is unlikely that such an impurity state has a shape that is non-dispersive.
- A dimer-shaped charge distribution might also stem from **polarons or bi-polarons**. In that case, we would expect a particle-hole anti-symmetric contrast, since the probability of injecting a charge is negative to the probability of extracting one.

Of course, a combination of above explanation is also possible. We hope that future experiments will bring some light into this. Better crystals of all ferropnictide families and the possibility to de-twinn orthorhombic crystals, which opens the field to many new techniques, will likely bring more access to the physics of underdoped ferropnictides.

Recent experimental evidence for C_2 -symmetric electronic structure

At the time of finishing this thesis, different experiments on de-twinned $\text{Ca}(\text{Fe}_{1-x}\text{Co}_x\text{As})_2$ crystals have been performed, many concentrating on the C_2 symmetry of the electronic structure. Most of them have not been published at the time of writing. Still, we want to try to give a brief overview for the sake of completeness:

- ARPES measurements indicate a strongly C_2 symmetric bandstructure and lead to the conclusion that we have strong correlation. It is the shape of the Fermi pockets that exhibit C_2 symmetry, not the photocurrent intensity (which is mainly governed by matrix elements). Experiments have been performed e.g. in the groups of Z.X. Shen and D. S. Dessau.
- Transport measurement showed strong resistivity anisotropy. Intriguingly this it is strongest at around 3% doping. The ratio between ϱ_b and ϱ_a is up to two [140].
- Neutron scattering experiments reported a anisotropy of the electronic structure before [130]. Now several groups report a ‘glassy’ state at the corresponding doping in the 11 family [141].

Bibliography

- [1] E. N. Zalta. ‘Emergent properties’. *The Stanford Encyclopedia of Philosophy* - <http://plato.stanford.edu/> (2003).
- [2] J. Kim. ‘Making sense of emergence’. *Philosophical Studies*, **9**, 3 (1999).
- [3] Radio Lab WNYC. ‘Emergence’. <http://www.wnyc.org/shows/radio-lab/episodes/2005/02/18> (2005).
- [4] P. W. Anderson. ‘More is different’. *Science*, **177**, 393 (1972).
- [5] N.W. Ashcroft and N.D. Mermin. *Solid State Physics*. Saunders College (Philadelphia) (1976).
- [6] S.D. Kevan and R.H. Gaylord. ‘High-resolution photoemission study to the electronic structure of the noble-metal (111) surfaces’. *Phys. Rev. B*, **36**, 5809 (1987).
- [7] F. Baumberger, T. Greber, and J. Osterwalder. ‘Fermi surfaces of the two-dimensional surface states on vicinal Cu(111)’. *Phys. Rev. B*, **64**, 195411 (2001).
- [8] F. Baumberger, T. Greber, B. Delley, and J. Osterwalder. ‘Tailoring confining barriers for surface states by step decoration: CO/vicinal Cu(111)’. *Phys. Rev. Lett.*, **88**, 237601 (2002).
- [9] DisplaySearchTM, NPD Group. ‘Projected sales of LCD displays’. www.displaysearch.com (2010).
- [10] S. A. Kivelson, E. Fradkin, and V. J. Emery. ‘Electronic liquid-crystal phases of a doped Mott insulator’. *Nature*, **393**, 550 (1998).
- [11] V. Hinkov, S. Pailhes, P. Bourges, Y. Sidis, A. Ivanov, A. Kulakov, C. T. Lin, D. P. Chen, C. Bernhard, and B. Keimer. ‘Two-dimensional geometry of spin excitations in the high-transition-temperature superconductor $\text{YBa}_2\text{Cu}_3\text{O}_{6+x}$ ’. *Nature*, **430**, 650 (2004).

- [12] Y. Kohsaka, C. Taylor, K. Fujita, A. Schmidt, C. Lupien, T. Hanaguri, M. Azuma, M. Takano, H. Eisaki, H. Takagi, S. Uchida, and J. C. Davis. ‘An intrinsic bond-centered electronic glass with unidirectional domains in underdoped cuprates’. *Science*, **315**, 1380 (2007).
- [13] S. Hüfner. *Photoelectron Spectroscopy, 3th edition*. Springer, Berlin (2003).
- [14] A. Damascelli, Z. Hussain, and Z.-X. Shen. ‘Angle-resolved photoemission studies of the cuprate superconductors’. *Rev. Mod. Phys.*, **75**, 473 (2003).
- [15] A. Tamai. *Molecular Arrangement and Electronic Properties of Low-Dimensional C₆₀ Systems*. Ph.D. thesis, Universität Zürich (2006).
- [16] M. Hengsberger, D. Purdie, P. Segovia, M. Garnier, and Y. Baer. ‘Photoemission study of a strongly coupled electron-phonon system’. *Phys. Rev. Lett.*, **83**, 592 (1999).
- [17] M. Hengsberger, R. Frésard, D. Purdie, P. Segovia, and Y. Baer. ‘Electron-phonon coupling in photoemission spectra’. *Phys. Rev. B*, **60**, 10796 (1999).
- [18] A. Lanzara, P. V. Bogdanov, X. J. Zhou, S. A. Kellar, D. L. Feng, E. D. Lu, T. Yoshida, H. Eisaki, A. Fujimori, K. Kishio, J. Shimoyama, T. Noda, S. Uchida, Z. Hussain, and Z. Shen. ‘Evidence for ubiquitous strong electron-phonon coupling in high-temperature superconductors’. *Nature*, **412**, 510 (2001).
- [19] A. Tamai, A. Y. Ganin, E. Rozbicki, J. Bacsá, W. Meevasana, P. D. C. King, M. Caffio, R. Schaub, S. Margadonna, K. Prassides, M. J. Rosseinsky, and F. Baumberger. ‘Strong electron correlations in the normal state of the iron-based FeSe_{0.42}Te_{0.58} superconductor observed by angle-resolved photoemission spectroscopy’. *Phys. Rev. Lett.*, **104**, 097002 (2010).
- [20] J. E. Hoffman. *A Search for Alternative Electronic Order in the High Temperature Superconductor Bi₂Sr₂CaCu₂O_{8+δ} by Scanning Tunneling Microscopy*. Ph.D. thesis, Cornell University (2003).
- [21] I. Giaever and H. Zeller. ‘Energy gap in superconductors measured by electron tunneling’. *Phys. Rev. Lett.*, **5**, 147 (1960).

- [22] Julian Chen. *Introduction to Scanning Tunneling Microscopy*. Oxford University Press. (1993).
- [23] M.F. Crommie, C.P. Lutz, and D.M. Eigler. ‘Imaging standing waves in a two-dimensional electron gas’. *Nature*, **363**, 524 (1993).
- [24] L. Petersen, P. Hofmann, and E. Plummer. ‘Fourier transform–STM: determining the surface Fermi contour’. *J. Electron Spectr.*, **109**, 97 (2000).
- [25] S. H. Pan, E. W. Hudson, J. Ma, and J. C. Davis. ‘Imaging and identification of atomic planes of cleaved $\text{Bi}_2\text{Sr}_2\text{CaCu}_2\text{O}_{8+\delta}$ by high resolution scanning tunneling microscopy’. *Appl. Phys. Lett.*, **73**, 58 (1998).
- [26] S. H. Pan, E. W. Hudson, and J. C. Davis. ‘Vacuum tunneling of superconducting quasiparticles from atomically sharp scanning tunneling microscope tips’. *Appl. Phys. Lett.*, **73**, 2992 (1998).
- [27] J. Lee, M. P. Allan, M. A. Wang, J. Farrell, S. A. Grigera, F. Baumberger, J. C. Davis, and A. P. Mackenzie. ‘Heavy d -electron quasiparticle interference and real-space electronic structure of $\text{Sr}_3\text{Ru}_2\text{O}_7$ ’. *Nat. Phys.*, **5**, 800. 10.1038/nphys1397 (2009).
- [28] A. Schmidt, M. Hamidian, P. Wahl, F. Meier, A. Balatsky, J. Garrett, T. Williams, G. Luke, and J. Davis. ‘Imaging the fano lattice to ‘hidden order’ transition in URu_2Si_2 ’. *submitted* (2010).
- [29] A. R. Schmidt. *Quasiparticle Interference and the impact of strong correlations on high temperature superconductivity*. Ph.D. thesis, Cornell University (2009).
- [30] K. McElroy, J. Lee, J. Slezak, D. Lee, H. Eisaki, S. Uchida, and J. C. Davis. ‘Atomic-scale sources and mechanism of nanoscale electronic disorder in $\text{Bi}_2\text{Sr}_2\text{CaCu}_2\text{O}_{8+\delta}$ ’. *Science*, **309**, 1048 (2005).
- [31] K. M. Lang, V. Madhavan, J. E. Hoffman, E. W. Hudson, H. Eisaki, S. Uchida, and J. C. Davis. ‘Imaging the granular structure of high- T_c superconductivity in underdoped $\text{Bi}_2\text{Sr}_2\text{CaCu}_2\text{O}_{8+\delta}$ ’. *Nature*, **415**, 412 (2002).
- [32] C. Taylor. *Coexistence of Bogoliubov Quasiparticles and Electronic Cluster Domains*. Ph.D. thesis, Cornell University (2008).

- [33] K. McElroy, R. Simmonds, J. E. Hoffman, D.-H. Lee, J. Orenstein, H. Eisaki, S. Uchida, and J. C. Davis. ‘Relating atomic-scale electronic phenomena to wave-like quasiparticle states in superconducting $\text{Bi}_2\text{Sr}_2\text{CaCu}_2\text{O}_{8+\delta}$ ’. *Nature* (2003).
- [34] J. E. Hoffman, K. McElroy, D. H. Lee, K. Lang, H. Eisaki, S. Uchida, and J. C. Davis. ‘Imaging quasiparticle interference in $\text{Bi}_2\text{Sr}_2\text{CaCu}_2\text{O}_{8+\delta}$ ’. *Science*, **297**, 1148 (2002).
- [35] S. H. Pan, E. W. Hudson, and J. C. Davis. ‘He-3 refrigerator based very low temperature scanning tunneling microscope’. *Rev. Sci. Instrum.*, **70**, 1459 (1999).
- [36] J. F. Mercure. *The de Haas-van Alphen effect near a quantum critical end point in $\text{Sr}_3\text{Ru}_2\text{O}_7$* . Ph.D. thesis, University of St. Andrews (2008).
- [37] Y. Maeno, K. Yoshida, H. Hashimoto, S. Nishizaki, S. Ikeda, M. Nohara, T. Fujita, A. Mackenzie, N. Hussey, J. Bednorz, and F. Lichtenberg. ‘Two-dimensional Fermi liquid behavior of the superconductor Sr_2RuO_4 ’. *J. Phys. Soc. Japan*, **66**, 1405 (1997).
- [38] A.P. Mackenzie and Y. Maeno. ‘The superconductivity of Sr_2RuO_4 and the physics of spin-triplet pairing’. *Rev. Mod. Phys.*, **75**, 657 (2003).
- [39] P. B. Allen, H. Berger, O. Chauvet, L. Forro, T. Jarlborg, A. Junod, B. Revaz, and G. Santi. ‘Transport properties, thermodynamic properties, and electronic structure of SrRuO_3 ’. *Phys. Rev. B*, **53**, 4393 (1996).
- [40] Q. Huang, J. W. Lynn, R. W. Erwin, J. Jarupatrakorn, and R. J. Cava. ‘Oxygen displacements and search for magnetic order in $\text{Sr}_3\text{Ru}_2\text{O}_7$ ’. *Phys. Rev. B*, **58**, 8515 (1998).
- [41] R. Kiyonagi, K. Tsuda, N. Aso, H. Kimura, Y. Noda, Y. Yoshida, S.-I. Ikeda, and Y. Uwatoko. ‘Investigation of the structure of single crystal $\text{Sr}_3\text{Ru}_2\text{O}_7$ by neutron and convergent beam electron diffractions’. *J. Phys. Soc. Japan*, **73**, 639 (2004).
- [42] R. Matzdorf, Z. Fang, Ismail, J. Zhang, T. Kimura, Y. Tokura, K. Terakura, and E. Plummer. ‘Ferromagnetism stabilized by lattice distortion at the surface of the p-wave superconductor Sr_2RuO_4 ’. *Science*, **289**, 746 (2000).

- [43] R. Matzdorf, Ismail, T. Kimura, Y. Tokura, and E. Plummer. ‘Surface structural analysis of the layered perovskite Sr_2RuO_4 by LEED I(V)’. *Phys. Rev. B*, **65**, 085404 (2002).
- [44] G. Cao, S. McCall, and J. E. Crow. ‘Observation of itinerant ferromagnetism in layered $\text{Sr}_3\text{Ru}_2\text{O}_7$ single crystals’. *Phys. Rev. B*, **55**, R672 (1997).
- [45] S. Ikeda and Y. Maeno. ‘Magnetic properties of bilayered $\text{Sr}_3\text{Ru}_2\text{O}_7$ ’. *Physica B*, **259-261**, 947 (1999).
- [46] R. S. Perry, L. M. Galvin, S. A. Grigera, L. Capogna, A. J. Schofield, A. P. Mackenzie, M. Chiao, S. R. Julian, S. I. Ikeda, S. Nakatsuji, Y. Maeno, and C. Pfleiderer. ‘Metamagnetism and critical fluctuations in high quality single crystals of the bilayer ruthenate $\text{Sr}_3\text{Ru}_2\text{O}_7$ ’. *Phys. Rev. Lett.*, **86**, 2661 (2001).
- [47] R. S. Perry, K. Kitagawa, S. A. Grigera, R. A. Borzi, A. P. Mackenzie, K. Ishida, and Y. Maeno. ‘Multiple first-order metamagnetic transitions and quantum oscillations in ultrapure $\text{Sr}_3\text{Ru}_2\text{O}_7$ ’. *Phys. Rev. Lett.*, **92**, 166602 (2004).
- [48] K. Iwaya, S. Satow, T. Hanaguri, N. Shannon, Y. Yoshida, S. I. Ikeda, J. P. He, Y. Kaneko, Y. Tokura, T. Yamada, and H. Takagi. ‘Local tunneling spectroscopy across a metamagnetic critical point in the bilayer ruthenate $\text{Sr}_3\text{Ru}_2\text{O}_7$ ’. *Phys. Rev. Lett.*, **99**, 057208 (2007).
- [49] J. Farrell. *The influence of cation doping on the electronic Properties of $\text{Sr}_3\text{Ru}_2\text{O}_7$* . Ph.D. thesis, University of St. Andrews (2009).
- [50] L. Fitting Kourkoutis. ‘Electron microscopy on $\text{Sr}_3\text{Ru}_2\text{O}_7$ ’. *Private communication* (2009).
- [51] S. Grigera, A. MacKenzie, A. Schofield, S. Julian, and G. Lonzarich. ‘A metamagnetic quantum critical endpoint in $\text{Sr}_3\text{Ru}_2\text{O}_7$ ’. *Int. J. Mod. Phys. B*, **16**, 3258 (2002).
- [52] S. A. Grigera, R. S. Perry, A. J. Schofield, M. Chiao, S. R. Julian, G. G. Lonzarich, S. I. Ikeda, Y. Maeno, A. J. Millis, and A. P. Mackenzie. ‘Magnetic field-tuned quantum criticality in the metallic ruthenate $\text{Sr}_3\text{Ru}_2\text{O}_7$ ’. *Science*, **294**, 329 (2001).
- [53] S. A. Grigera, P. Gegenwart, R. A. Borzi, F. Weickert, A. J. Schofield, R. S. Perry, T. Tayama, T. Sakakibara, Y. Maeno, A. G. Green, and

- A. P. Mackenzie. ‘Disorder-sensitive phase formation linked to metamagnetic quantum criticality’. *Science*, **306**, 1154 (2004).
- [54] R. A. Borzi, S. A. Grigera, J. Farrell, R. S. Perry, S. J. S. Lister, S. L. Lee, D. A. Tennant, Y. Maeno, and A. P. Mackenzie. ‘Formation of a nematic fluid at high fields in $\text{Sr}_3\text{Ru}_2\text{O}_7$ ’. *Science*, **315**, 214 (2007).
- [55] A. W. Rost, R. S. Perry, J. F. Mercure, A. P. Mackenzie, and S. A. Grigera. ‘Entropy landscape of phase formation associated with quantum criticality in $\text{Sr}_3\text{Ru}_2\text{O}_7$ ’. *Science*, **325**, 1360 (2009).
- [56] S.-I. Ikeda, Y. Maeno, S. Nakatsuji, M. Kosaka, and Y. Uwatoko. ‘Ground state in $\text{Sr}_3\text{Ru}_2\text{O}_7$: Fermi liquid close to a ferromagnetic instability’. *Phys. Rev. B*, **62**, R6089 (2000).
- [57] S. Sachdev. *Quantum phase transitions*. Cambridge University Press, Cambridge (1999).
- [58] B. Binz and M. Sgrist. ‘Metamagnetism of itinerant electrons in multi-layer ruthenates’. *Europhys. Lett.*, **65**, 816 (2004).
- [59] H.-Y. Kee and Y. B. Kim. ‘Itinerant metamagnetism induced by electronic nematic order’. *Phys. Rev. B*, **71**, 184402 (2005).
- [60] C. Puetter, H. Doh, and H.-Y. Kee. ‘Metanematic transitions in a bilayer system: Application to the bilayer ruthenate’. *Phys. Rev. B*, **76**, 235112 (2007).
- [61] H. Yamase and A. A. Katanin. ‘Van Hove singularity and spontaneous Fermi surface symmetry breaking in $\text{Sr}_3\text{Ru}_2\text{O}_7$ ’. *J. Phys. Soc. Japan*, **76**, 5 (2007).
- [62] S. Raghu, A. Paramakanti, E. A. Kim, R. A. Borzi, S. A. Grigera, A. P. Mackenzie, and S. A. Kivelson. ‘Microscopic theory of the nematic phase in $\text{Sr}_3\text{Ru}_2\text{O}_7$ ’. *Phys. Rev. B*, **79**, 214402 (2009).
- [63] W.-C. Lee and C. Wu. ‘Nematic electron states enhanced by orbital band hybridization’. *arXiv:0902.1337v2* (2009).
- [64] M.H. Fischer and M. Sgrist. ‘Effect of a staggered spin-orbit coupling on the occurrence of a nematic phase in $\text{Sr}_3\text{Ru}_2\text{O}_7$ ’. *arXiv:0909.5392v1* (2009).

- [65] A. Tamai, M. P. Allan, J. F. Mercure, W. Meevasana, R. Dunkel, D. H. Lu, R. S. Perry, A. P. Mackenzie, D. J. Singh, Z. X. Shen, and F. Baumberger. ‘Fermi surface and van Hove singularities in the itinerant metamagnet $\text{Sr}_3\text{Ru}_2\text{O}_7$ ’. *Phys. Rev. Lett.*, **101**, 026407 (2008).
- [66] C.M. Puetter and J. G. Rau, H.-Y. Kee. ‘Effect of a staggered spin-orbit coupling on the occurrence of a nematic phase in $\text{Sr}_3\text{Ru}_2\text{O}_7$ ’. *arXiv:0909.4545v2* (2009).
- [67] A. Damascelli, D. H. Lu, K. M. Shen, N. P. Armitage, F. Ronning, D. L. Feng, C. Kim, Z.-X. Shen, T. Kimura, Y. Tokura, Z. Q. Mao, and Y. Maeno. ‘Fermi surface, surface states, and surface reconstruction in Sr_2RuO_4 ’. *Phys. Rev. Lett.*, **85**, 5194 (2000).
- [68] R.A. Borzi, S.A. Grigera, R.S. Perry, N. Kikugawa, K. Kitagawa, Y. Maeno, and A.P. Mackenzie. ‘de Haas–van Alphen effect across the metamagnetic transition in $\text{Sr}_3\text{Ru}_2\text{O}_7$ ’. *Phys. Rev. Lett.*, **92**, 216403 (2004).
- [69] J.-F. Mercure, S. K. Goh, E. C. T. O’Farrell, R. S. Perry, M. L. Sutherland, A. W. Rost, S. A. Grigera, R. A. Borzi, P. Gegenwart, and A. P. Mackenzie. ‘Quantum oscillations in the anomalous phase in $\text{Sr}_3\text{Ru}_2\text{O}_7$ ’. *Phys. Rev. Lett.*, **103**, 176401 (2009).
- [70] J. F. Mercure, A. W. Rost, E. C. T. O’Farrell, S. K. Goh, R. S. Perry, M. L. Sutherland, S. A. Grigera, R. A. Borzi, P. Gegenwart, A. S. Gibbs, and A. P. Mackenzie. ‘Quantum oscillations near a quantum critical end point in $\text{Sr}_3\text{Ru}_2\text{O}_7$ ’. *arXiv:0909.1215* (2009).
- [71] W. Meevasana, F. Baumberger, K. Tanaka, F. Schmitt, W. R. Dunkel, D. H. Lu, S.-K. Mo, H. Eisaki, and Z.-X. Shen. ‘Extracting the spectral function of the cuprates by a full two-dimensional analysis: Angle-resolved photoemission spectra of $\text{Bi}_2\text{Sr}_2\text{CuO}_6$ ’. *Phys. Rev. B*, **77**, 104506 (2008).
- [72] N.J.C. Ingle *et al.* ‘Quantitative analysis of Sr_2RuO_4 angle-resolved photoemission spectra: Many-body interactions in a model Fermi liquid’. *Phys. Rev. B*, **72**, 205114 (2005).
- [73] K. M. Shen, N. Kikugawa, C. Bergemann, L. Balicas, F. Baumberger, W. Meevasana, N. J. C. Ingle, Y. Maeno, Z. X. Shen, and A. P. Mackenzie. ‘Evolution of the Fermi surface and quasiparticle renormalization through a van Hove singularity in $\text{Sr}_{2-y}\text{La}_y\text{RuO}_4$ ’. *Phys. Rev. Lett.*, **99**, 187001 (2007).

- [74] E. Rozbicki. ‘LDA+SO’. *Private communication* (2010).
- [75] W.-C. Lee and C. Wu. ‘Spectroscopic imaging scanning tunneling microscopy as a probe of orbital structures and ordering’. *Phys. Rev. Lett.*, **103**, 176101 (2009).
- [76] R.A. Borzi *et al.* ‘de Haas–van Alphen effect across the metamagnetic transition in $\text{Sr}_3\text{Ru}_2\text{O}_7$ ’. *Phys. Rev. Lett.*, **92**, 216403 (2004).
- [77] S. Engelsberg and J.R. Schrieffer. ‘Coupled electron-phonon system’. *Phys. Rev.*, **131**, 993 (1963).
- [78] S. LaShell, E. Jensen, and T. Balasubramanian. ‘Observation of non-quasiparticle structure in the photoemission spectra from the $\text{be}(0001)$ surface and determination of the electron self-energy’. *Phys. Rev. B*, **61**, 2371 (2000).
- [79] X. J. Zhou, J. Shi, T. Yoshida, T. Cuk, W. L. Yang, V. Brouet, J. Nakamura, N. Mannella, S. Komiyama, Y. Ando, F. Zhou, W. X. Ti, J. W. Xiong, Z. X. Zhao, T. Sasagawa, T. Kakeshita, H. Eisaki, S. Uchida, A. Fujimori, Z. Zhang, E. W. Plummer, R. B. Laughlin, Z. Hussain, and Z.-X. Shen. ‘Multiple bosonic mode coupling in the electron self-energy of $(\text{La}_{2-x}\text{Sr}_x)\text{CuO}_4$ ’. *Phys. Rev. Lett.*, **95**, 117001 (2005).
- [80] T. Greber, T.J. Kreuz, and J. Osterwalder. ‘Photoemission above the Fermi level: the top of the minority d band in nickel’. *Phys. Rev. Lett.*, **79**, 4465 (1997).
- [81] L. Capogna, E. M. Forgan, S. M. Hayden, A. Wildes, J. A. Duffy, A. P. Mackenzie, R. S. Perry, S. Ikeda, Y. Maeno, and S. P. Brown. ‘Observation of two-dimensional spin fluctuations in the bilayer ruthenate $\text{Sr}_3\text{Ru}_2\text{O}_7$ by inelastic neutron scattering’. *Phys. Rev. B*, **67**, 012504 (2003).
- [82] M. B. Stone, M. D. Lumsden, R. Jin, B. C. Sales, D. Mandrus, S. E. Nagler, and Y. Qiu. ‘Temperature-dependent bilayer ferromagnetism in $\text{Sr}_3\text{Ru}_2\text{O}_7$ ’. *Phys. Rev. B*, **73**, 174426 (2006).
- [83] S. Ramos, E. M. Forgan, C. Bowell, S. M. Hayden, A. J. Schofield, A. Wildes, E. A. Yelland, S. P. Brown, M. Laver, R. S. Perry, and Y. Maeno. ‘Spin dynamics in $\text{Sr}_3\text{Ru}_2\text{O}_7$ near the metamagnetic transition by inelastic neutron scattering’. *Physica B*, **403**, 1270 (2008).

- [84] J. Farrell, R. S. Perry, A. Rost, J. F. Mercure, N. Kikugawa, S. A. Grigera, and A. P. Mackenzie. ‘Effect of electron doping the metamagnet $\text{Sr}_{3-y}\text{La}_y\text{Ru}_2\text{O}_7$ ’. *Phys. Rev. B*, **78**, 180409 (2008).
- [85] S. A. Carter, B. Batlogg, R. J. Cava, J. J. Krajewski, W. F. Peck, and L. W. Rupp. ‘Mechanism for the metal-insulator transition in $\text{Sr}_2\text{Ir}_{1-x}\text{Ru}_x\text{O}_4$ ’. *Phys. Rev. B*, **51**, 17184 (1995).
- [86] S. Elgazzar, J. Ruzs, M. Amft, P. M. Oppeneer, and J. A. Mydosh. ‘Hidden order in URu_2Si_2 originates from Fermi surface gapping induced by dynamic symmetry breaking’. *Nat. Mat.*, **8**, 337 (2009).
- [87] B. I. Barker, S. K. Dutta, C. Lupien, P. L. McEuen, N. Kikugawa, Y. Maeno, and J. C. Davis. ‘STM studies of individual Ti impurity atoms in Sr_2RuO_4 ’. *Physica B*, **329-333**, 1334 (2003).
- [88] K. McElroy, G.-H. Gweon, S. Y. Zhou, J. Graf, S. Uchida, H. Eisaki, H. Takagi, T. Sasagawa, D.-H. Lee, and A. Lanzara. ‘Elastic scattering susceptibility of the high temperature superconductor $\text{Bi}_2\text{Sr}_2\text{CaCu}_2\text{O}_{8+\delta}$: A comparison between real and momentum space photoemission spectroscopies’. *Phys. Rev. Lett.*, **96**, 067005 (2006).
- [89] R. S. Markiewicz. ‘Bridging k and q space in the cuprates: Comparing angle-resolved photoemission and STM results’. *Phys. Rev. B*, **69**, 214517 (2004).
- [90] Y. Kamihara, T. Watanabe, M. Hirano, and H. Hosono. ‘Iron-based layered superconductor $\text{LaO}_{1-x}\text{F}_x\text{FeAs}$ ($x = 0.05 - 0.12$) with $T_c=26$ K’. *J. Am. Chem. Soc.*, **130**, 3296 (2008).
- [91] K. Ishida, Y. Nakai, and H. Hosono. ‘To what extent iron-pnictide new superconductors have been clarified: A progress report’. *J. Phys. Soc. Japan*, **78**, 062001 (2009).
- [92] M. Norman. ‘High-temperature superconductivity in the iron pnictides’. *Physics* (2008).
- [93] J. Bednorz and K. Müller. ‘Possible high T_c superconductivity in the BaLaCuO system’. *Z. Phys. B* (1986).
- [94] D. Larbalestier, A. Gurevich, D. M. Feldmann, and A. Polyanskii. ‘High- T_c superconducting materials for electric power applications’. *Nature*, **414**, 368 (2001).

- [95] A. Jesche, C. Krellner, M. de Souza, M. Lang, and C. Geibel. ‘Structural and magnetic transition in CeFeAsO: separated or connected?’ *arXiv:1001.4349* (2010).
- [96] H. Kito, H. Eisaki, and A. Iyo. ‘Superconductivity at 54 K in F-free NdFeAsO_{1-y}’. *J. Phys. Soc. Japan*, **77**, 063707 (2008).
- [97] M. Rotter, M. Tegel, and D. Johrendt. ‘Superconductivity at 38 K in the iron arsenide (Ba_{1-x}K_x)Fe₂As₂’. *Phys. Rev. Lett.*, **101**, 107006 (2008).
- [98] K. Sasmal, B. Lv, B. Lorenz, A. M. Guloy, F. Chen, Y.-Y. Xue, and C.-W. Chu. ‘Superconducting fe-based compounds (A_(1-x)Sr_x)Fe₂As₂ with A=K and cs with transition temperatures up to 37 K’. *Phys. Rev. Lett.*, **101**, 107007 (2008).
- [99] N. Ni, S. Nandi, A. Kreyssig, A. I. Goldman, E. D. Mun, S. L. Bud’ko, and P. C. Canfield. ‘First-order structural phase transition in CaFe₂As₂’. *Phys. Rev. B*, **78**, 014523 (2008).
- [100] H. Hosono. ‘Two classes of superconductors discovered in our material research: Iron-based high temperature superconductor and electride superconductor’. *Physica C*, **469**, 314. Elsevier B.V. (2009).
- [101] X. C. Wang, Q. Q. Liu, Y. X. Lv, W. B. Gao, L. X. Yang, R. C. Yu, F. Y. Li, and C. Q. Jin. ‘The superconductivity at 18 K in LiFeAs system’. *Solid State Commun.*, **148**, 538 (2008).
- [102] T. L. Xia, J. B. He, D. M. Wang, and G. F. Chen. ‘Superconductivity at 33 K in "111" single crystals at ambient pressure’. *arXiv:1001.3311* (2010).
- [103] Y. Mizuguchi, F. Tomioka, S. Tsuda, T. Yamaguchi, and Y. Takano. ‘Superconductivity at 27 K in tetragonal FeSe under high pressure’. *Appl. Phys. Lett.*, **93**, 152505 (2008).
- [104] X. Zhu, F. Han, G. Mu, B. Zeng, P. Cheng, B. Shen, and H.-H. Wen. ‘Sr₃Sc₂Fe₂As₂O₅ as a possible parent compound for FeAs-based superconductors’. *Phys. Rev. B*, **79**, 024516 (2009).
- [105] H. Ogino, Y. Katsura, S. Horii, K. Kishio, and J. ichi Shimoyama. ‘New iron-based arsenide oxides (Fe₂As₂)(Sr₄M₂O₆) (M=Sc, Cr)’. *Supercond. Sci. Technol.*, **22**, 085001 (2009).

- [106] H. P. Nguyen, I. Yeam, A. Angot, and G. B. Martin. ‘AvrPto’. *New Phytol.* (2010).
- [107] S. Graser, T. Maier, P. Hirschfeld, and D. Scalapino. ‘Near-degeneracy of several pairing channels in multiorbital models for the Fe pnictides’. *N. J. Phys.* (2009).
- [108] M. Yi, D. H. Lu, J. G. Analytis, J.-H. Chu, S.-K. Mo, R.-H. He, M. Hashimoto, R. G. Moore, I. I. Mazin, D. J. Singh, Z. Hussain, I. R. Fisher, and Z.-X. Shen. ‘Unconventional electronic reconstruction in undoped (Ba,Sr)Fe₂As₂ across the spin density wave transition’. *Phys. Rev. B*, **80**, 174510 (2009).
- [109] M. Yi, D. H. Lu, J. G. Analytis, J. H. Chu, S. K. Mo, R. H. He, R. G. Moore, X. J. Zhou, G. F. Chen, J. L. Luo, N. L. Wang, Z. Hussain, D. J. Singh, I. R. Fisher, and Z. X. Shen. ‘Electronic structure of the BaFe₂As₂ family of iron-pnictide superconductors’. *Phys. Rev. B*, **80**, 024515 (2009).
- [110] C. Liu, T. Kondo, N. Ni, A. D. Palczewski, A. Bostwick, G. D. Samolyuk, R. Khasanov, M. Shi, E. Rotenberg, S. L. Bud’ko, P. C. Canfield, and A. Kaminski. ‘Three- to two-dimensional transition of the electronic structure in CaFe₂As₂: A parent compound for an iron arsenic high-temperature superconductor’. *Phys. Rev. Lett.*, **102**, 167004 (2009).
- [111] D. Evtushinsky, D. Inosov, V. Zabolotnyy, M. Viazovska, R. Khasanov, A. Amato, H. Klauss, H. Luetkens, C. Niedermayer, G. Sun, V. Hinkov, C. Lin, A. Varykhalov, A. Koitzsch, M. Knupfer, B. Buechner, A. Kordyuk, and S. Borisenko. ‘Momentum-resolved superconducting gap in the bulk of Ba_{1-x}K_xFe₂As₂ from combined ARPES and μ -SR measurements’. *New J. Phys.*, **11**, 550069 (2009).
- [112] H. Liu, W. Zhang, L. Zhao, X. Jia, J. Meng, G. Liu, X. Dong, G. F. Chen, J. L. Luo, N. L. Wang, W. Lu, G. Wang, Y. Zhou, Y. Zhu, X. Wang, Z. Xu, C. Chen, and X. J. Zhou. ‘Fermi surface and band renormalization of Sr_{1-x}K_xFe₂As₂ from angle-resolved photoemission spectroscopy’. *Phys. Rev. B*, **78**, 184514 (2008).
- [113] P. Richard, T. Sato, K. Nakayama, S. Souma, T. Takahashi, Y.-M. Xu, G. F. Chen, J. L. Luo, N. L. Wang, and H. Ding. ‘Angle-resolved photoemission spectroscopy of the Fe-based Ba_{0.6}K_{0.4}Fe₂As₂ high temperature superconductor: Evidence for an orbital selective electron-mode coupling’. *Phys. Rev. Lett.*, **102**, 047003 (2009).

- [114] S. de Jong, E. van Heumen, S. Thirupathaiah, R. Huisman, F. Masee, J. B. Goedkoop, R. Ovsyannikov, J. Fink, H. A. Dorr, A. Gloskovskii, H. S. Jeevan, P. Gegenwart, A. Erb, L. Patthey, M. Shi, R. Follath, A. Varykhalov, and M. S. Golden. ‘Droplet-like Fermi surfaces in the anti-ferromagnetic phase of EuFe_2As_2 , an Fe-pnictide superconductor parent compound’. *EPL (Europhysics Letters)*, **89**, 27007 (2010).
- [115] C. de La Cruz, Q. Huang, J. W. Lynn, J. Li, W. R. , II, J. L. Zarestky, H. A. Mook, G. F. Chen, J. L. Luo, N. L. Wang, and P. Dai. ‘Magnetic order close to superconductivity in the iron-based layered $\text{LaO}_{1-x}\text{F}_x\text{FeAs}$ systems’. *Nature*, **453**, 899 (2008).
- [116] N. Ni, A. Thaler, A. Kracher, J. Q. Yan, S. L. Bud’ko, and P. C. Canfield. ‘Phase diagrams of $\text{Ba}(\text{Fe}_{1-x}\text{M}_x)_2\text{As}_2$ single crystals ($M = \text{Rh}$ and Pd)’. *Phys. Rev. B*, **80**, 024511 (2009).
- [117] A. I. Goldman, A. Kreyssig, K. Prokess, D. K. Pratt, D. N. Argyriou, J. W. Lynn, S. Nandi, S. A. J. Kimber, Y. Chen, Y. B. Lee, G. Samolyuk, J. B. Leao, S. J. Poulton, S. L. Bud’ko, N. Ni, P. C. Canfield, B. N. Harmon, and R. J. McQueeney. ‘Lattice collapse and quenching of magnetism in CaFe_2As_2 under pressure: A single-crystal neutron and X-ray diffraction investigation’. *Phys. Rev. B*, **79**, 024513 (2009).
- [118] D. K. Pratt, W. Tian, A. Kreyssig, J. L. Zarestky, S. Nandi, N. Ni, S. L. Bud’ko, P. C. Canfield, A. I. Goldman, and R. J. McQueeney. ‘Coexistence of competing antiferromagnetic and superconducting phases in the underdoped $\text{Ba}(\text{Fe}_{0.953}\text{Co}_{0.047})_2\text{As}_2$ compound using X-ray and neutron scattering techniques’. *Phys. Rev. Lett.*, **103**, 087001 (2009).
- [119] R. H. McKenzie. ‘Similarities between organic and cuprate superconductors’. *Science*, **278**, 820 (1997).
- [120] Z. Tesanovic. ‘Are iron pnictides new cuprates?’ *Physics*, **2**, 60 (2009).
- [121] M. C. Boyer, K. Chatterjee, W. D. Wise, G. F. Chen, J. L. Luo, N. L. Wang, and E. W. Hudson. ‘Scanning tunneling microscopy of the 32 K superconductor $(\text{Sr}_{1-x}\text{K}_x)\text{Fe}_2\text{As}_2$ ’. *arXiv:0806.4400* (2008).
- [122] Y. Yin, M. Zech, T. L. Williams, X. F. Wang, G. Wu, X. H. Chen, and J. E. Hoffman. ‘Scanning tunneling spectroscopy and vortex imaging in the iron pnictide superconductor $\text{BaFe}_{1.8}\text{Co}_{0.2}\text{As}_2$ ’. *Phys. Rev. Lett.*, **102**, 097002 (2009).

- [123] F. Masee, Y. Huang, R. Huisman, S. de Jong, J. B. Goedkoop, and M. S. Golden. ‘Nanoscale superconducting-gap variations and lack of phase separation in optimally doped $\text{BaFe}_{1.86}\text{Co}_{0.14}\text{As}_2$ ’. *Phys. Rev. B*, **79**, 220517 (2009).
- [124] D. Hsieh, Y. Xia, L. Wray, D. Qian, K. Gomes, A. Yazdani, G. F. Chen, J. L. Luo, N. L. Wang, and M. Z. Hasan. ‘Experimental determination of the microscopic origin of magnetism in parent iron pnictides’. *arXiv:0812.2289* (2008).
- [125] V. B. Nascimento, A. Li, D. R. Jayasundara, Y. Xuan, J. O’Neal, S. Pan, T. Y. Chien, B. Hu, X. B. He, G. Li, A. S. Sefat, M. A. McGuire, B. C. Sales, D. Mandrus, M. H. Pan, J. Zhang, R. Jin, and E. W. Plummer. ‘Surface geometric and electronic structures of $\text{BaFe}_2\text{As}_2(001)$ ’. *Phys. Rev. Lett.*, **103**, 076104 (2009).
- [126] F. C. Niestemski, V. B. Nascimento, B. Hu, W. Plummer, J. Gillett, S. Sebastian, Z. Wang, and V. Madhavan. ‘Unveiling the atomic and electronic structure at the surface of the parent pnictide SrFe_2As_2 ’. *arXiv:0906.2761* (2009).
- [127] T. Kondo, R. M. Fernandes, R. Khasanov, C. Liu, A. D. Palczewski, N. Ni, M. Shi, A. Bostwick, E. Rotenberg, J. Schmalian, S. L. Bud’ko, P. C. Canfield, and A. Kaminski. ‘Unusual Fermi surface nesting in parent compounds of iron arsenic high temperature superconductors revealed by angle resolved photoemission spectroscopy’. *arXiv:0905.0271* (2009).
- [128] A. Kemper, C. Cao, P. Hirschfeld, and H. Cheng. ‘Effects of cobalt doping and three-dimensionality in BaFe_2As_2 ’. *Phys. Rev. B*, **80**, 104511 (2009).
- [129] S.-H. Baek, N. J. Curro, T. Klimczuk, E. D. Bauer, F. Ronning, and J. D. Thompson. ‘First-order magnetic transition in single-crystalline CaFe_2As_2 detected by ^{75}As nuclear magnetic resonance’. *Phys. Rev. B*, **79**, 052504 (2009).
- [130] J. Zhao, D. T. Adroja, D.-X. Yao, R. Bewley, S. Li, X. F. Wang, G. Wu, X. H. Chen, J. Hu, and P. Dai. ‘Spin waves and magnetic exchange interactions in CaFe_2As_2 ’. *Nat. Phys.*, **5**, 555 (2009).
- [131] S. O. Diallo, V. P. Antropov, T. G. Perring, C. Broholm, J. J. Pulkottil, N. Ni, S. L. Bud’ko, P. C. Canfield, A. Kreyssig, A. I. Goldman,

- and R. J. McQueeney. ‘Itinerant magnetic excitations in antiferromagnetic CaFe_2As_2 ’. *Phys. Rev. Lett.*, **102**, 187206 (2009).
- [132] F. Masee, S. de Jong, Y. Huang, J. Kaas, E. van Heumen, J. B. Goedkoop, and M. S. Golden. ‘Cleavage surfaces of the $\text{BaFe}_{2-x}\text{Co}_x\text{As}_2$ and $\text{Fe}_y\text{Se}_{1-x}\text{Te}_x$ superconductors: A combined STM plus LEED study’. *Phys. Rev. B*, **80**, 140507 (2009).
- [133] Y. Yin, M. Zech, T. Williams, and J. Hoffman. ‘Scanning tunneling microscopy and spectroscopy on iron-pnictides’. *Physica C*, **469**, 535 . Superconductivity in Iron-Pnictides (2009).
- [134] M. Gao, F. Ma, Z.-Y. LU, and T. Xiang. ‘Atomic and electronic structures of ternary iron arsenides $\text{AFe}_2\text{As}_2(001)$ surfaces ($A=\text{Ba}$, Sr , or Ca)’. *arXiv:0909.5136* (2009).
- [135] J. Goldstein. *Scanning electron microscopy and X-ray microanalysis*. Academic/Plenum Publishers (2003).
- [136] J. Zaanen and O. Gunnarsson. ‘Charged magnetic domain lines and the magnetism of high- t_c oxides’. *Phys. Rev. B*, **40**, 7391 (1989).
- [137] V. Emery and S. Kivelson. ‘Frustrated electronic phase separation and high-temperature superconductors’. *Physica C*, **209**, 597 (1993).
- [138] T. Shimojima, K. Ishizaka, Y. Ishida, N. Katayama, K. Ohgushi, T. Kiss, M. Okawa, T. Togashi, X. Y. Wang, C. T. Chen, S. Watanabe, R. Kadota, T. Oguchi, A. Chainani, and S. Shin. ‘Orbital-dependent modifications of electronic structure across magneto-structural transition in BaFe_2As_2 ’. *Phys. Rev. Lett.*, **104**, 057002 (2009).
- [139] S. H. Pan, E. W. Hudson, K. M. Lang, H. Eisaki, S. Uchida, and J. C. Davis. ‘Imaging the effects of individual zinc impurity atoms on superconductivity in $\text{Bi}_2\text{Sr}_2\text{CaCu}_2\text{O}_{8+\delta}$ ’. *Nature*, **403**, 746 (2000).
- [140] J.-H. Chu, J. G. Analytis, K. D. Greve, P. L. McMahon, Z. Islam, Y. Yamamoto, and I. R. Fisher. ‘Evidence for an electron nematic phase transition in underdoped iron pnictide superconductors’. *arXiv:1002.3364v2* (2010).
- [141] N. Katayama, S. Ji, D. Louca, S.-H. Lee, M. Fujita, T. J. Sato, J. S. Wen, Z. J. Xu, G. D. Gu, G. Xu, Z. W. Lin, M. Enoki, S. Chang, K. Yamada, and J. M. Tranquada. ‘Investigation of the spin-glass regime between the antiferromagnetic and superconducting phases in $\text{Fe}_{1+y}\text{Se}_x\text{Te}_{1-x}$ ’. *arXiv:1003.4525v1* (2010).